

Institut für Theoretische Physik
Fakultät Mathematik und Naturwissenschaften
Technische Universität Dresden

Dynamics of Cilia and Flagella

Dissertation

Zur Erlangung des akademischen Grades

Doctor rerum naturalium
(Dr. rer. nat.)

vorgelegt von

Andreas Hilfinger

Geboren am 13. Juni 1977 in Schwenningen a.N.

Max-Planck-Institut für
Physik komplexer Systeme



Dresden, 2005

To my teachers and parents

Abstract

What are cilia and flagella Cilia and flagella are hair-like appendages of eukaryotic cells. They are actively bending structures that exhibit regular beat patterns and thereby play an important role in many different circumstances where motion on a cellular level is required. Most dramatic is the effect of nodal cilia whose vortical motion leads to a fluid flow that is directly responsible for establishing the left-right axis during embryological development in many vertebrate species, but examples range from the propulsion of single cells, such as the swimming of sperm, to the transport of mucus along epithelial cells, e.g. in the ciliated trachea.

Our objective Cilia and flagella contain an evolutionary highly conserved structure called the axoneme, whose characteristic architecture is based on a cylindrical arrangement of elastic filaments (microtubules). In the presence of a chemical fuel (ATP), molecular motors (dynein) exert shear forces between neighbouring microtubules, leading to a bending of the axoneme through structural constraints. We address the following two questions: How can these organelles generate regular oscillatory beat patterns in the absence of a biochemical signal regulating the activity of the force generating elements? And how can the beat patterns be so different for apparently very similar structures?

Our results We present a theoretical description of the axonemal structure as an actively bending elastic cylinder, and show that in such a system bending waves emerge from a non-oscillatory state via a dynamic instability. The corresponding beat patterns are solutions to a set of coupled partial differential equations presented herein.

Our approach enables us to discuss analytically, three dimensional beat patterns that resemble qualitatively the motion of nodal cilia that play an important role in establishing the left-right asymmetry during embryological development in vertebrates.

Focusing on beats confined to a surface we put forward a hypothesis concerning axonemal beat pattern control, in which we explicitly discuss the previously neglected mechanical properties of the basal connection. In collaboration with I. Riedel and J. Howard we estimate quantitatively the mechanical properties of the basal connection of bull sperm flagella by comparing theoretical beat patterns to experimental data from beating bull sperm.

Acknowledgements

First and foremost I thank Prof. Frank Jülicher for his supervision during these exciting three years. Throughout this thesis definite traces, not only of his style but hopefully also his scientific rigour can be found. It is with great appreciation that I acknowledge the time and energy he invested in “teaching me science”. I hope these efforts were not entirely futile.

Not formally appointed as such, Prof. Jonathon Howard acted as co-supervisor of this thesis by having an indirect, yet enormous influence through his PhD student Ingmar Riedel, who I am fortunate enough to call my collaborator and friend.

Ingmar and I spent hours, days and weeks arguing and fighting about every aspect of this project. If anyone had witnessed these encounters they would have to be excused for assuming that we were trying to mock our supervisors’ style of scientific discussion, with Ingmar as a constant source of innovative speculations about the nature of flagellar beat and my constant efforts to ground those speculations in rigorous definitions and precise statements. These encounters taught me what science is all about – the intense interaction of curious minds. What more could I have hoped for?

I would have never succeeded without the help of my fellow students at the Max-Planck-Institute for the Physics of Complex Systems. I constantly annoyed them with countless questions regarding important and not so important aspects of my research. I thank Björn Nadrowski, Nils Becker, Alexander Zumdieck, Gernot Klein, Tobias Bollenbach, Peter Borowski, Nilüfer Baba, and Elisabeth Fischer for their help and encouragement.

Dr Karsten Kruse’s role as a mentor of graduate students in the biological physics department cannot be exaggerated. He is a leading example of how to combine research of highest standard with a kind-hearted and friendly attitude.

On the administrative side of things Nadine Baldes – with her way of solving even the most difficult (and usually urgent) problems while keeping everyone’s spirits high – is the glue holding a whole department together. We are all greatly indebted to her for her extraordinary efforts.

I also gratefully acknowledge Prof. Raymond Goldstein, Prof. Charles Brokaw, Prof. Donner Babcock, Prof. Peter Satir, Prof. Hans Machemer, Prof. Jean-François Joanny, Boris Guirao and Dr Amit Chattopadhyay for helpful discussions.

Both institutes at which I had the pleasure to work, are blessed with extraordinarily helpful librarians. I thank Mrs Heidi Näther and Mrs Silke Thüm for their invaluable assistance.

I thank Sebastian Debnar-Daumler, Susanne Abraham and Laura Buffa for their friendship and tremendous support especially during the later stages of this project. On top of being the most incredible and inspiring friends one can imagine, I am very grateful to Emma Pooley and Ben Hope for proofreading this thesis.

On a much longer time-scale I wholeheartedly thank my parents for their love and support over the years. They are the ones that made it possible for me to pursue the dream of becoming a scientist – a certainly not very pragmatic (read sensible) career choice.

Contents

1	Introduction	1
1.1	What cilia and flagella are and why they are important	1
1.2	The key elements of cilia and flagella	3
1.2.1	Microtubules	3
1.2.2	Molecular motors	3
1.2.3	The axoneme	5
1.2.4	The basal body	6
1.3	What we know about axonemal beat patterns	6
1.3.1	Differences in structure and observed beat patterns	6
1.3.2	The influence of Ca^{2+}	9
1.3.3	The role of the central pair	10
1.3.4	Effects of external oscillations and motor mutations	11
1.4	Existing theoretical approaches	11
1.5	Our approach	12
2	The physics of the axoneme – an actively bending tube	13
2.1	Geometry	13
2.2	Energetics	14
2.2.1	Relating geometry to motor activity	16
2.2.2	Virtual displacements	18
2.3	Overdamped dynamics	20
2.3.1	Incompressibility constraint	21
2.3.2	Dynamic equations	21
2.3.3	Boundary conditions	21

3	Planar motion	23
3.1	Dynamic equations	25
3.2	Non-linear solutions – an analytical expansion	28
3.3	Numerical solutions	30
3.3.1	Mathematical structure and implementation	30
3.3.2	Finite amplitude non-linear waves	31
4	Flagellar beats observed in vivo	33
4.1	Comparing linearly unstable modes to experimental beat patterns	33
4.2	Beat pattern control via the basal apparatus	36
5	Three dimensional beat patterns	41
5.1	Equilibrium configuration and linearly unstable modes	41
5.2	Beating patterns for symmetric bending rigidities	44
6	Conclusions and discussion	49
6.1	Summary of our results	50
6.2	Outlook on future work	51
6.2.1	Generic properties vs microscopic details of physical systems	51
6.2.2	Discussing asymmetry - on which side lies your heart?	51
A	Local sliding expression	53
B	Variational discussion	57
C	Integrating variational terms by parts	61
D	Three dimensional non-linear equations and boundary terms	63
E	Non-linear perturbation calculation	69
F	Complete experimental dataset with theoretical fits	77
G	Unstable modes for microscopic motor models	81
H	Boundary condition defining matrices	83
	Bibliography	85

Introduction

1.1. What cilia and flagella are and why they are important

In a way we all owe our existence to the beating of cilia and flagella, since not only the swimming of sperm but also the transport of the fertilised egg to the uterus is a result of the activity of these organelles. But let us proceed systematically and introduce the subject of this thesis step by step. Cilia and flagella are actively bending hair-like appendages that act as sensing and motility generating organelles of eukaryotic cells. Their evolutionary highly conserved¹ working mechanism as well as their widespread occurrence in a great variety of systems demonstrate the power and importance of physical interactions as a means of achieving biological function.

A prominent example of the many different circumstances where the ability of cilia and flagella to generate regular beat patterns plays a vital role to create motion on a cellular level is the **propulsion of single cells** such as the swimming of protozoa and spermatozoa. Also the **transport of fluid** along a stationary layer of cells as for example in the trachea and oviduct is achieved through the beating of cilia covering epithelial cells. Another most striking display of the importance of ciliary beats is the recently discovered vortical motion of nodal cilia that leads to an external fluid flow during embryological development [2]. This flow has been shown to be responsible for the **establishment of the left-right axis** across many vertebrate species [3], a spectacular finding that has answered the long standing medical puzzle of why approximately half of the people whose cilia are immotile due to a genetic defect (primary ciliary dyskinesia²) exhibit an inversion of the usual left-right asymmetry of their internal organs (situs inversus) [4].

¹Their form is structurally so similar in all eukaryotes that their evolutionary origin is believed to date back as far as the last common eukaryotic ancestor that lived around 1-2 billion years ago [1].

²Previously known as “immotile-cilia syndrome”

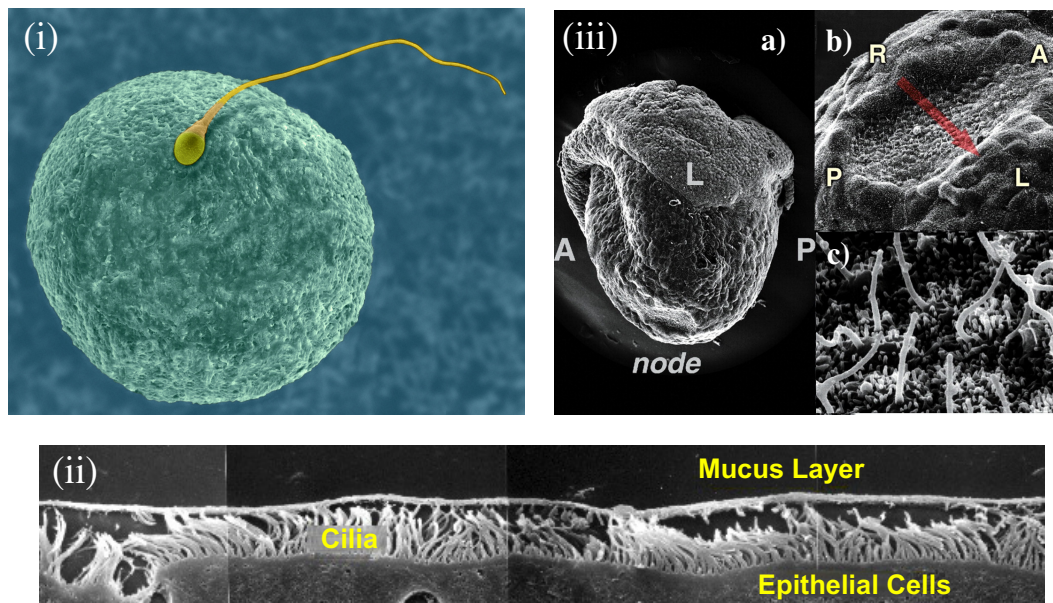


Figure 1.1: Cilia and flagella at work in different circumstances. i) Spermatozoa are propelled forward by the whip-like beat patterns of a single flagellum. Typical beat frequencies are in the range of tens of Hertz leading to swimming speeds of the order of tens of $\mu\text{m/s}$. The sperm flagellum is typically around $30\text{-}60\ \mu\text{m}$ long, although extreme exceptions exist. In the picture you can see two false coloured scanning electron micrographs merged, showing a human spermatozoon and egg illustrating the moment of fertilisation. Reproduced with kind permission from Dennis Kunkel Microscopy, Inc. with whom the copyright remains [5]. ii) In the respiratory tract the concerted action of beating cilia transports mucus up the trachea (wind pipe) which works as an important cleaning and defence mechanism [6], sometimes instructively called “mucociliary escalator”. Edited from [7]. iii) Scanning electron micrographs showing an eight day old mouse embryo (a) and in detail the ventral node cells (b) with their monocilia (c). These short ($2\text{-}3\ \mu\text{m}$) cilia rotate in clockwise direction with a frequency of around 10Hz and lead to an external fluid flow, as indicated by the red arrow in (b) which establishes the embryo’s left-right axis. Edited from [8] with the anterior-posterior and left-right axes indicated by A,P,L,R.

1.2. The key elements of cilia and flagella

Cilia and flagella are two different names that are often used interchangeably for the same structure of eukaryotic cells. As suggested by the meaning of the words (*lat.* cilia “eyelashes”, flagellum “whip”) the term cilia tends to be used when the cellular appendages are short and abound on a single cell, whereas the term flagellum is used for longer filaments, of which only one or two are usually found per cell. Their inner structure is characterised by a cylindrical core called the axoneme, which is a cylindrical arrangement of elastic filaments (microtubules) and force generating molecular motors (dynein) as explained in the following. Unfortunately the term flagellum is also used for the hair-like appendages of bacteria, which are fundamentally different. Prokaryotic flagella of e.g. *E. coli* are described in detail in [9]. Their dynamical properties have for example been studied in [10,11], and will be discussed in this work only as far as the equations describing such dynamics can be regarded as the passive limit of the equations derived in this thesis describing the axonemal structure. In the remainder of this work we will use the term flagellum to mean eukaryotic flagellum only.

1.2.1. Microtubules

Microtubules are small tubes with a diameter of 25nm [12], built from smaller building blocks of tubulin. They are a key component of the cytoskeleton where, because of their long persistence length of several μm due to the high bending rigidity of around $30 \times 10^{-24} \text{Nm}^2$ [13], they play an important role where mechanical stability is required in cells. Examples are the dendritic structures in axons, mitotic spindles during cell division and of course the axoneme. By convention their structural polarity defines a plus and minus end³. On top of their structural function microtubules also form the backbone of the cell’s internal transport machinery by acting as tracks along which molecular motors move, as discussed in the next section. Microtubules can be highly dynamic [12], but in the case of cilia and flagella, the microtubules that form the axoneme are stable and have a constant length.

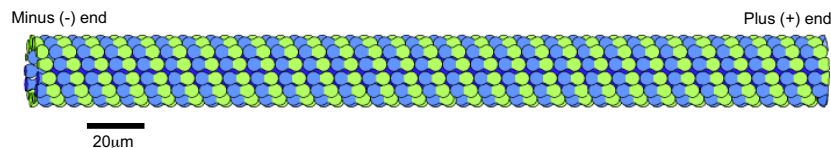


Figure 1.2: Schematic diagram of a microtubule filament – a cylindrical arrangement of polar tubulin monomers, made up of β -tubulin (blue) and α -tubulin (green). Edited from [14].

1.2.2. Molecular motors

What have come to be known as molecular motors are remarkable proteins, that convert chemical energy to mechanical work by coupling ATP binding and ATP hydrolysis to conformational changes [15,16]. The recent headline *20 billion motors for 1 cent* [17] illustrates nicely the scale (and the “nano-hype”). They come in a great variety of families that

³Note that this terminology has nothing to do with electrical charges.

bind to different filaments, moving in different (but specified) directions with different speeds and processivity [13]. However, their working mechanism can be understood in a general framework that describes the attachment and detachment of the motor as well as the hydrolysis of ATP and the consequential conformational change as a continuous cycle as illustrated schematically in Fig. 1.3.

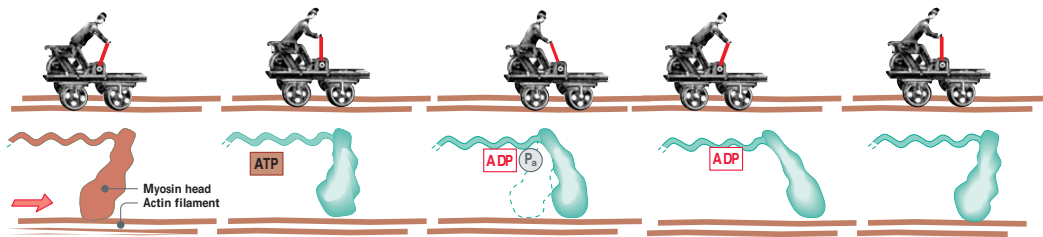


Figure 1.3: Schematic illustration of a processive molecular motor (in this case myosin) moving along a polar filament (in this case actin) as observed experimentally in [18,19]. Taken from [17].

We focus on the motor protein dynein, which is a minus end directed microtubule associated motor and the force generating element in cilia and flagella [20]. It is a large molecule with a 10nm long stem and one to three heads of a relative molecular weight of around 500kDa, each containing an ATP hydrolysing and microtubule binding site. The power stroke of a single headed dynein has recently been shown to be around 15nm and could be visualised directly using electron microscopy and image processing as illustrated in Fig. 1.4.

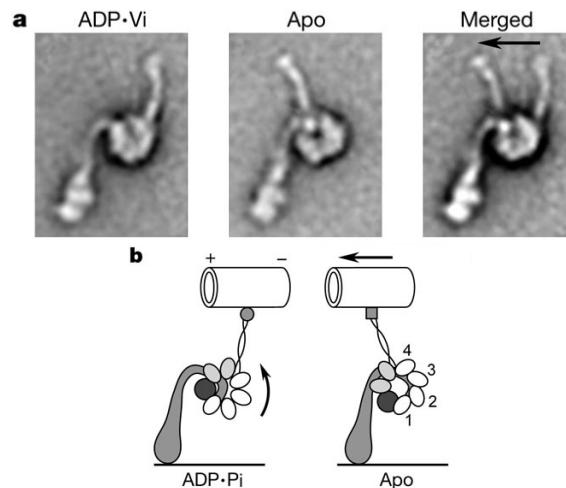


Figure 1.4: Electron micrographs (a) depicting the structure and speculative power stroke of a single headed dynein molecule, as schematically illustrated in (b). Apo refers to the nucleotide free dynein structure and corresponds to the post-power stroke conformation, whereas ADP-Vi refers to the ADP with vanadate construct that is thought to mimic the pre-power stroke conformation corresponding to the ADP-Pi state. The arrow indicates 15nm. Source [21].

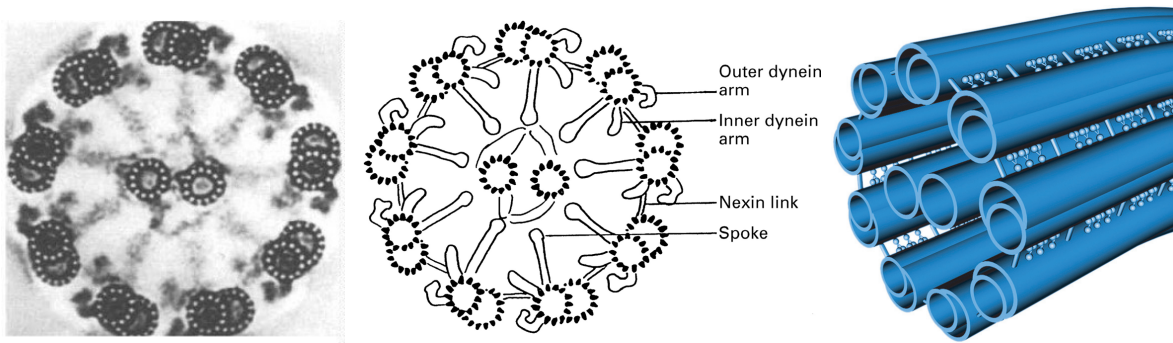


Figure 1.5: A computer enhanced electron micrograph of a cross section through the 9+2 axoneme [22] and a corresponding schematic illustration when viewed from the basal end [23], leading to a three dimensional impression of the axonemal structure as depicted above [24].

1.2.3. The axoneme

The axoneme consists of nine cylindrically arranged microtubule doublets, that are connected by the molecular motor protein dynein as illustrated in Fig. 1.5. Their structure is chiral (i.e. it has a handedness) such that when viewed from the distal end, the motors are rigidly attached with their stems to one microtubule doublet reaching with their motile heads for the neighbouring doublet in counterclockwise direction [25]. In the described architecture this ATP driven motion of outer and inner dynein arms will lead to a relative sliding between microtubule doublets, as illustrated in Fig. 1.6. The whole structure is held together by stable but flexible nexin links connecting the microtubules.

The axoneme comes in two versions, with and without a central pair which connects to the peripheral microtubules by radial spokes. The two configurations are referred to as 9+2 and 9+0 axoneme respectively, and typically differ in their beat patterns as elaborated below in section 1.3.

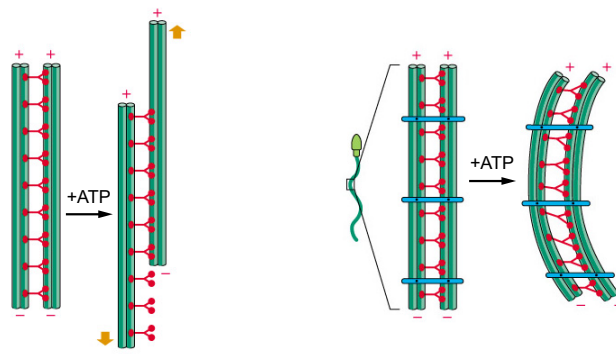


Figure 1.6: Schematic illustration of dynein induced microtubule sliding with and without geometric constraints. The case of freely sliding microtubules is realised in axonemes whose nexin links are broken, which disintegrate upon activation of dynein [26]. Taken from [12].

1.2.4. The basal body

The basal body anchors the minus ends of the microtubules and connects the axoneme to the rest of the cell⁴. It is similar in structure to the axoneme, but consists of nine microtubule triplets without a central pair ranging around 400nm [27] into the cell. The basal body is identical in structure to centrioles, two of which arranged in a perpendicular fashion constitute a centrosome, which plays an important role in organising cell division. Hence its protein interactions have been at the centre of research, whereas the mechanical properties of the anchoring of the axoneme to the cell have so far not been resolved in detail. However, recent observations suggest that the connection is sufficiently flexible to allow for relative sliding between microtubules even at the base of the axoneme [28]. Defects of the basal body have been implicated as a likely cause of Bardet-Biedl syndrome, a rare inherited condition with severe effects such as mental retardation, obesity, degeneration of the retinas of the eyes and kidney abnormalities, all associated with dysfunctional cilia [29].

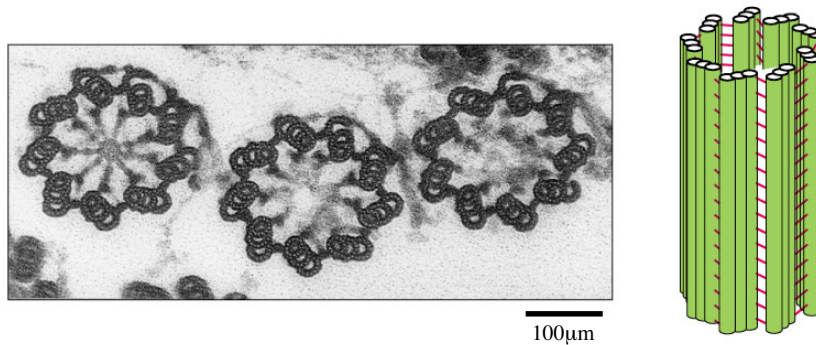


Figure 1.7: Electron micrograph of a cross-section through a collection of basal bodies, and a schematic illustration. Taken from [12].

1.3. What we know about axonemal beat patterns

1.3.1. Differences in structure and observed beat patterns

9+2 flagella

As a single whip-like appendage, 9+2 flagella drive many different species of spermatozoa by means of generating a planar travelling wave. They also occur in pairs such as in the biflagellate alga *Chlamydomonas reinhardtii*⁵, where their motion is also planar, but more breaststroke like. In the recently published Ph.D. thesis of our collaborator I. Riedel [30] the planar beat pattern of 9+2 bull sperm flagella has been analysed quantitatively using Fourier modes, which form a reliable cornerstone to test theoretical hypotheses. These flagellar

⁴In mammalian sperm flagella the axoneme is anchored by so called “outer dense fibres”, which attach the microtubule doublets to the “connecting piece”, that plays the role of the basal body.

⁵The workhorse of genetic research on flagella. Many motility affecting mutations are known, with phenotypes that lead to important conclusions as discussed in the remainder of this section.

beat patterns are usually travelling waves confined to a plane (with a small out of plane contribution). These waves normally travel from base to tip, although there are exceptions such as the flagella of the kinetoplastid *Crithidia oncopelti* exhibit waves in the opposite direction⁶ [31]. It has also been observed that at unphysiologically high viscosities of the surrounding medium (1.5-4Pas), the usual planar beat of sea urchin (*Echinus esculentus*) spermatozoa can change into a fully three-dimensional helical beat pattern [32]. Typical beat frequencies of 9+2 flagella are a few tens of Hertz with flagellar lengths ranging from 10-100 μm [33], although extreme exceptions exist⁷.

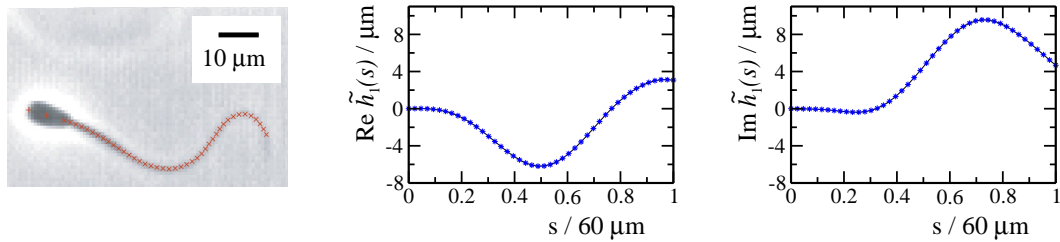


Figure 1.8: Snapshot of a bull sperm beating in a plane, with an automatically tracked 9+2 flagellum. Real and imaginary part of the first Fourier mode describing the time dependent amplitude $h(s, t)$ of a bull sperm attached to the cover slip beating with $\omega/2\pi \approx 20\text{Hz}$, as analysed in [30]. $h(s, t) \approx \tilde{h}^{(0)}(s) + \frac{1}{2}\tilde{h}^{(1)}(s)e^{i\omega t} + \text{c.c.}$, where s is the arclength along the flagellum.

9+0 flagella

The spermatozoa of a small number of species such as eel (*Anguilla anguilla*) and the Asian horseshoe crab (*Tachypleus tridentatus* and *Tachypleus gigas*) have spermatozoa whose axonemes lack a central pair [35,36]. These 9+0 flagella beat in a helical fashion, where the handedness of the helix differs between the two species. Eel spermatozoa also lack the outer dynein arms and exhibit an unusually high frequency of up to 110Hz⁸.

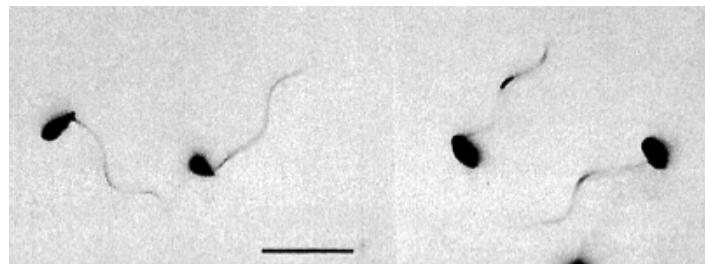


Figure 1.9: Inverted darkfield micrograph of swimming eel sperm showing the helicoidal beat pattern of 9+0 flagella. The bar indicates 20 μm . Edited from [37]

It is interesting to note that there exist even more extreme architectures of axonemes

⁶Which means that in contrast to the majority of protozoa *Crithidia* swims flagellum first.

⁷For example the spermatozoa of *Drosophila melanogaster* have an incredibly long flagellum with an average length of 2mm [34].

⁸Which does not seem to be an effect of the specific 9+0 architecture, since spermatozoa from the general group of teleosts (such as trout) whose flagella do not lack the central pair, beat with similarly high frequencies.

without a central pair. The parasitic protozoon *Lecudina tuzetea* and the male gametes of the gregarian sporozoan *Diplauxis hatti* have flagella with a 6+0 and 3+0 axoneme, respectively that exhibit helical motion [38–40]. Mutants of *Chlamydomonas* that lack the central pair and radial spokes are generally immotile [41]. However motility can be restored by suppressor mutations without restoring the structural defect [42,43] or under conditions with unphysiological salt and ATP concentrations [44–46].

9+2 cilia

These “conventional” cilia commonly cover epithelial cells of higher animals, but are also found in large numbers on uni-cellular organisms such as the protozoon *Paramecium*. There are usually many of these cilia per cell (10-200). Their complex three dimensional beating pattern, consisting of a power and recovery stroke, is usually co-ordinated such that an effective global motion is achieved as illustrated in Fig. 1.10.

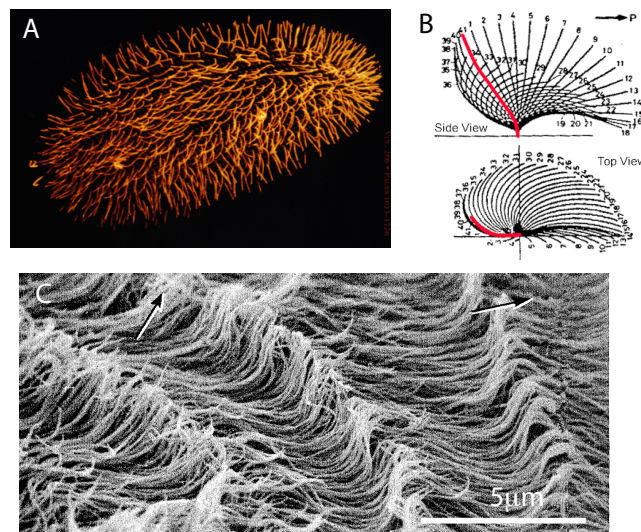


Figure 1.10: (A) Scanning electron micrograph of a *Paramecium* with kind permission from Dr Anne Fleury-Aubusson [47]. (B) Schematic diagram illustrating the 9+2 ciliary beat pattern, consisting of power stroke and recovery stroke. Edited from [48]. (C) Metachronal waves as seen on the ciliated surface of the protozoon *Opalina ranarum* nicely illustrating the global motion that is produced by the coordinated beating of 9+2 cilia. Edited from [49].

9+0 cilia

These cilia, long thought to be immotile, occur typically one per cell (therefore often called monocilia or primary cilia) and are an almost ubiquitous feature of many cells of higher organisms [50]. Already twenty years ago it was reported that a small number of solitary cilia of the rabbit oviductal epithelium move in a rotational way, counterclockwise⁹

⁹All circling directions described in this thesis will be described when viewed from above. This is different from the conventional view from the basal end traditionally used in the cilia and flagella literature, but is the natural view when observing the motion of motile cilia under the microscope. In this thesis we stick to this convention (describing the axonemal structure and its motion when viewed from the distal end) to uniquely identify the sense of rotation, a problem that has caused considerable confusion in the existing literature [51].

– in the one illustrated case [52]. Since the recent discovery of rotating cilia in the ventral node of mouse embryos [2] motile monocilia have also been discovered in the node equivalent of rabbit and medaka fish [3], all of which circle in a clockwise direction. In the case of the mouse node, the cilia are posteriorly tilted [53,54] such that their clockwise rotation results in an external leftward fluid flow. This has been shown to be directly responsible for determining the left-right axis of the developing embryo [55], as indicated in Fig. 1.11¹⁰. It is interesting to note that the 9+0 monocilia in the spinal cord of zebrafish were shown to rotate in counterclockwise direction [56], similar to a small number of nodal cilia in a mutant (*inv*) mouse embryo [3], which shows that the direction of rotation is not a direct result of the chirality of the axonemal structure, which is the same for all cilia. Typically these beating monocilia are around 2 – 3 μ m long and rotate with a frequency of approximately 10Hz.

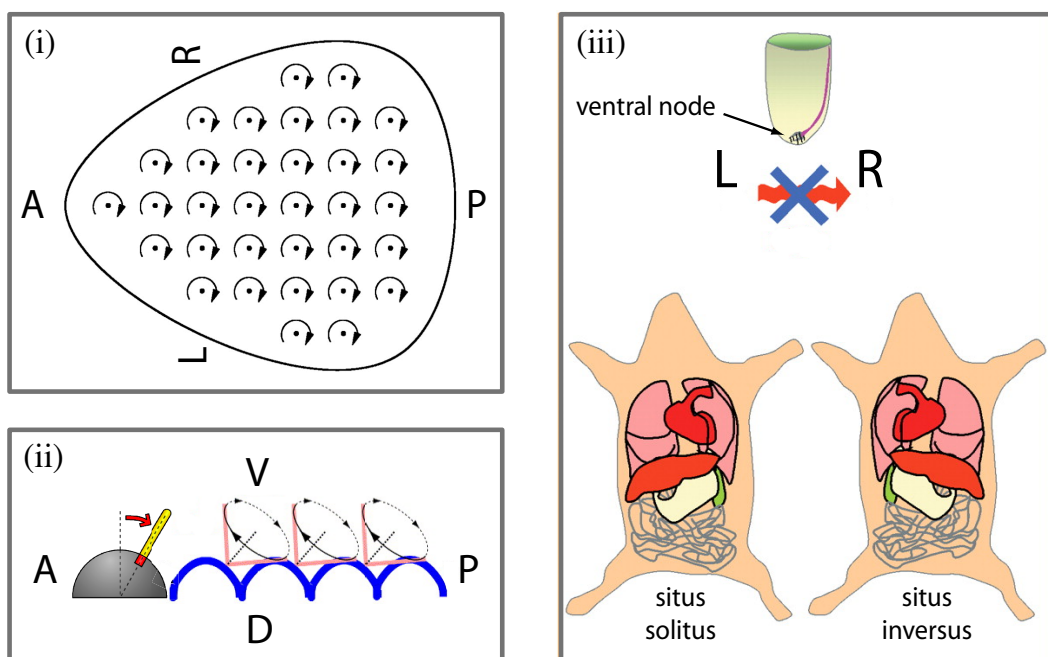


Figure 1.11: Nodal flow and situs inversion. i) Ventral node as viewed from above, indicating an array of clockwise rotating monocilia. ii) Illustration of the posteriorly tilted orientation of the nodal cilia, that leads to a leftward fluid flow. iii) Normal and inverse development of the left-right axis, randomised due to the lack of a leftward fluid flow in the node. Anterior-posterior, ventral-dorsal and left-right axes are indicated by A,P,V,D,L,R. Edited from [3,53,54,57].

1.3.2. The influence of Ca^{2+}

The concentration of Ca^{2+} has a significant effect on ciliary and flagellar beat patterns. Effects can be as extreme as wave reversal such as in *Crithidia* [58] where the normal direction of tip to base travelling waves¹¹ has been shown to be reversed in reactivated axonemes above

¹⁰Whether this fluid flow establishes a morphogene gradient that leads to an asymmetric gene expression pattern or whether the directed fluid flow as such is detected with cilia that act as mechanosensors, is the subject of ongoing debate.

¹¹Recall that the usual direction of flagellar beats of *Crithidia* is the opposite of typical flagellar waves, leading to *Crithidia* swimming flagellum first.

a critical Ca^{2+} concentration of approximately 10^{-4}M [59]. Interestingly, the degree of asymmetry of flagellar wave patterns of sea urchin spermatozoa (and therefore the radius of their circular swimming paths) can be controlled by changing the concentration of Ca^{2+} in a range from 10^{-7} to 10^{-5}M [60]¹². Flagella of *Chlamydomonas* exhibit a similar effect, albeit with a response of opposite nature. Whereas sea urchin spermatozoa wave patterns become more asymmetrical as the concentration of Ca^{2+} is increased, *Chlamydomonas* beat patterns become more symmetrical [61].

Note, that all of the above experiments involve demembrated and reactivated flagella¹³ in order to examine the effect of ion concentrations on axonemal beat patterns. A recent study using caged cyclic GMP molecules to open Ca^{2+} channels using modern fluorescence imaging techniques to detect directly the level of intracellular Ca^{2+} suggests that it is a rapid influx of Ca^{2+} rather than the absolute level of Ca^{2+} that induces a response in the beat pattern [62].

1.3.3. The role of the central pair

The observed motility of 9+0 cilia and flagella as described above, as well as rescued motility of previously thought immotile mutant 9+0 flagella, directly contradict the incorrect view that the central pair is essential for axonemal motility as such. The beat patterns of cilia and flagella naturally lacking the central pair have been described as helical or vortical, suggesting that the central pair is somehow necessary to achieve a planar axonemal beat. However, intriguingly the flagellar beat of central pair lacking *Chlamydomonas* mutants is only slightly more three-dimensional than that of the 9+2 wildtype [63].

The hypothesis that the plane of beat might be determined by the orientation of the central pair has been shown to be wrong, since for example the central pair twists in the near planar beats of *Chlamydomonas* flagella [64]. This does not imply that it acts as a “distributor” to regulate the activity of dyneins as suggested in [64–66], since the central pair rotation has subsequently been shown to be a passive response to the bend propagation along the axoneme [67]. For several other organisms the central pair maintains a fixed orientation relative to the plane of axonemal beating [68], which leaves the mechanism of how the central pair is involved in achieving a planar beat as an open question. Regarding how this cylindrical structure comes to exhibit planar beat patterns, it is an important finding that two of the microtubule doubles are thought to be permanently linked in many cases [69,70].

Many studies show that Ca^{2+} has an effect on the axonemal beat patterns that is mediated via the central pair and the radial spokes apparatus [66,68,71,72]. However, the view that the central pair and the radial spokes apparatus are essential for waveform conversions due to Ca^{2+} [73], has been contradicted by the findings that reactivated flagella from *Chlamydomonas* mutants lacking the central pair exhibit a pronounced Ca^{2+} dependent effect [63], leaving us to conclude that the role of the central pair remains elusive despite many efforts to understand the reason for its preserved existence.

¹²Sea urchin spermatozoa become quiescent above a critical Ca^{2+} concentration of around 10^{-4}M .

¹³I.e. the cell membrane is dissolved using a detergent such as Triton with the spermatozoa in “reactivation solution” that contains appropriate amounts of salt ions such as Ca^{2+} , K^+ , Mg^{2+} as well as ATP.

1.3.4. Effects of external oscillations and motor mutations

To further complicate matters, it has been shown that inner and outer dynein arm mutants of *Chlamydomonas* exhibit different phenotypes. Comparing the beat patterns of flagella lacking outer dynein arms with those of wildtype flagella, it was demonstrated that outer dynein arm deficient mutants beat with a normal waveform at reduced frequency. This is in contrast to beat patterns of flagella lacking a subset of inner dynein arms, where the frequency is normal but the beat pattern is significantly reduced in amplitude compared with the wild-type [74]. This is interpreted as a different biological function of inner and outer dynein arms in generating axonemal beat patterns, although from a physical point of view their function is identical – generating shear forces. The different effect of interfering with inner and outer dynein arms might be due to the different force generating properties of these motor families, as suggested by several experiments involving inner and outer dynein arm *Chlamydomonas* mutants, that compared swimming velocities at different viscosities [75] or sliding disintegration velocities [76]. Their results indicate that the different dynein sub-families have distinct force-velocity relations and so given that at least eleven different axonemal dynein heavy chains (i.e. the motor heads) have been identified – all with presumably different mechanochemical properties – the question of how the axoneme can work as an efficient machine while being equipped with motors working at intrinsically different speeds, has been asked [77]. It is interesting to note that individual dynein molecules have been observed to exhibit oscillations when working against an elastic element [78]. The diversity of axonemal dynein motors and their properties is reviewed in [79].

Another interesting experimental result is that the frequency as well as the plane of beat of sperm flagella can be influenced by mechanical stimulation. Spermatozoa whose head were held by suction of a micropipette, adapted their beat frequency to the frequency of the laterally vibrating pipette over a range of 20-70 Hz [80]. In a similar set up, where the plane of vibrations was rotated, the plane of beat followed the plane defined by the external vibrations. Remarkably, this resulted in a “wound up” flagellum that spontaneously unwound back to its original orientation once the external vibrations were stopped [81]. In subsequent studies it was shown that these rotations of the beat plane do not correspond to a rotation of the axonemal structure as such [82], and intriguingly that spontaneous unwinding only occurs after prior clockwise winding (as seen from the distal end of the flagellum) [83].

1.4. Existing theoretical approaches

The first theoretical study discussing the swimming of micro-organisms deduced that the Reynolds number of such motion is very small, meaning that – in contrast to macroscopic swimming – inertial forces are negligible in magnitude to viscous forces [84]. A point that has been taken up in Purcell’s entertaining and popular article [85] in which it was stressed that *Life at Low Reynolds-Number* differs fundamentally from our experiences. If a swimming sperm stops beating it “coasts” less than 10^{-10} m and comes to a halt within 10^{-6} s. Matching the elastic and viscous forces of a bending rod in two dimensions, equations describing the motion of an actively bending structure at low Reynolds number, were first derived in [86]. Discussing solutions to these equations¹⁴ for different boundary conditions

¹⁴Which are linear equations, valid in the limit of small amplitudes.

and comparing them with experimental observations, the existence of active force generators along the flagellum was established. After the discovery of the axonemal structure with its characteristic microtubule sliding [87], those active elements were identified experimentally as molecular dynein motors [20] that exert shear forces between neighbouring microtubules [88]. But to this day the mechanism behind the periodic force generation leading to travelling waves remains elusive. Hence in many of the subsequent modelling approaches the activity of the internal motors was – somewhat arbitrarily – put in by hand in order to mimic ciliary and flagellar beats [89–91].

Two hypotheses have been put forward proposing that the activity of motors is directly regulated by the geometry of the axoneme. The “geometric clutch hypothesis” was first reported in [92] and developed further in [93]. It proposes that in a bending axoneme transverse forces develop that pull neighbouring microtubule doublets apart and that this increase in inter-doublet spacing leads to a decrease in the probability of dynein engagement. The “curvature control hypothesis” proposes that the activity of motors is regulated directly by the degree of axonemal bending [94]. Although neither mechanism is supported by any direct experimental evidence on a microscopic level, they have been shown to produce travelling waves in computer models and have been discussed extensively in [94–100].

A third hypothesis is based on the observation that a system of many molecular motors acting against an elastic element can oscillate spontaneously as supported by theoretical [101] as well as experimental analyses [102,103]. The resulting axonemal dynamics, due to the collective properties of the molecular motors present in the axoneme, have been discussed for the two-dimensional case in a computer model [104] and analytically [105,106]. These studies concluded that travelling waves would naturally occur in such a system.

1.5. Our approach

In this thesis we look at the physical properties of an axoneme in the complete absence of biochemical regulation. Similar to [86] we deduce axonemal dynamics from matching viscous and elastic forces, but in contrast to [86] present a full three-dimensional description of the axonemal structure. Taking the ability of a collection of molecular motors to exhibit spontaneous oscillations [101] into account we discuss the equations of motion describing the axoneme. The limiting cases of this system reproduce previously reported equations describing the dynamics of a two-dimensional actively bending filament [105,106] as well as the dynamics of a passive three-dimensional filament [107]. Discussing the two-dimensional limit, we examine the non-linear effects on axonemal dynamics and extend existing theoretical approaches by allowing for basal sliding of microtubules, as experimentally observed in [28].

As a concluding remark of this introduction we would like to point out that the extensive use of active formulations such as “we present” or “we conclude” is not due a misguided perception of the author’s importance but rather an effort to improve the readability of this thesis.

The physics of the axoneme – an actively bending tube

In this chapter we present a theoretical description of the forces describing the dynamics of the basic axonemal structure. We represent the axoneme as a cylinder with an active surface that is capable of generating shear stresses, which constitutes a continuum approximation of the discrete microscopic structure, such that the active elements are represented as local shear force densities.

2.1. Geometry

We start by denoting the path of the central line of the axonemal structure¹ as $\mathbf{r}(s)$. Defining $\mathbf{r}(s) : \mathbb{R} \rightarrow \mathbb{R}^3$ such that it is a curve parametrised by its arclength, we construct a right handed orthonormal set of vectors $\mathbf{e}_1(s), \mathbf{e}_2(s), \mathbf{e}_3(s)$ such that the vector $\mathbf{e}_3(s) \equiv \dot{\mathbf{r}}(s)$ points along the central pair in the direction from base to tip and $\mathbf{e}_2(s)$ lies in the plane defined by the central pair as detailed in Fig. 2.1. This constitutes a “material frame” in which the rates of change of the vectors $\mathbf{e}_1(s), \mathbf{e}_2(s), \mathbf{e}_3(s)$ along s correspond to the twisting and bending of the axoneme.

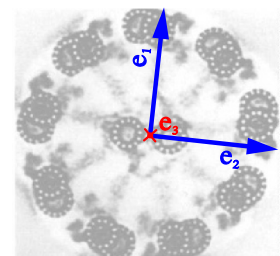


Figure 2.1: Definition of material frame

Making use of this material frame we denote the cylindrical surface of the axoneme (of radius a) by $\mathbf{R}(s, \phi)$, which can be expressed as follows

$$\mathbf{R}(s, \phi) = \mathbf{r}(s) + a\mathbf{e}_1(s) \cos \phi + a\mathbf{e}_2(s) \sin \phi \quad (2.1)$$

where the curves $\mathbf{R}(s, \phi_n)$ for $\phi_n = \frac{2\pi}{9}n, n = 0, \dots, 8$ can be thought of as the paths of the nine peripheral microtubule doublets as indicated in Fig. 2.3. A twist of the axonemal structure, as for example seen in the configuration depicted in Fig. 2.4, is then described by a rotation of $\mathbf{e}_1(s), \mathbf{e}_2(s)$ around $\mathbf{e}_3(s)$ along the curve $\mathbf{r}(s)$.

¹Which can be thought of as the trace of the central pair

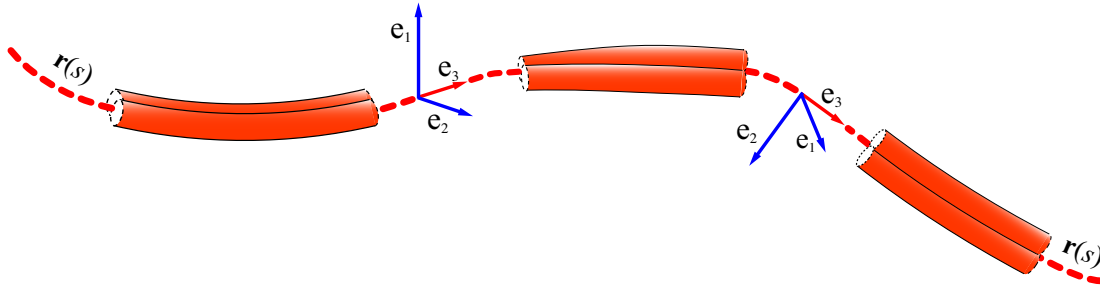


Figure 2.2: Definition of the right-handed coordinate system $\mathbf{e}_1(s), \mathbf{e}_2(s), \mathbf{e}_3(s)$ with $\mathbf{e}_3(s)$ tangential to the central line $\mathbf{r}(s)$ and $\mathbf{e}_1(s), \mathbf{e}_2(s)$ pointing towards material reference points.

The curvatures $\Omega_1(s), \Omega_2(s)$ and material twist $\Omega_3(s)$ are defined by following relations

$$\partial_s \begin{pmatrix} \mathbf{e}_1(s) \\ \mathbf{e}_2(s) \\ \mathbf{e}_3(s) \end{pmatrix} = \begin{pmatrix} 0 & \Omega_3(s) & -\Omega_2(s) \\ -\Omega_3(s) & 0 & \Omega_1(s) \\ \Omega_2(s) & -\Omega_1(s) & 0 \end{pmatrix} \begin{pmatrix} \mathbf{e}_1(s) \\ \mathbf{e}_2(s) \\ \mathbf{e}_3(s) \end{pmatrix} \quad (2.2)$$

Hence the quantities $\Omega_1(s), \Omega_2(s), \Omega_3(s)$ determine $\mathbf{e}_1(s), \mathbf{e}_2(s), \mathbf{e}_3(s)$ (up to translations and rotations) and therefore the shape of the axoneme and the configuration of the microtubule doublets.

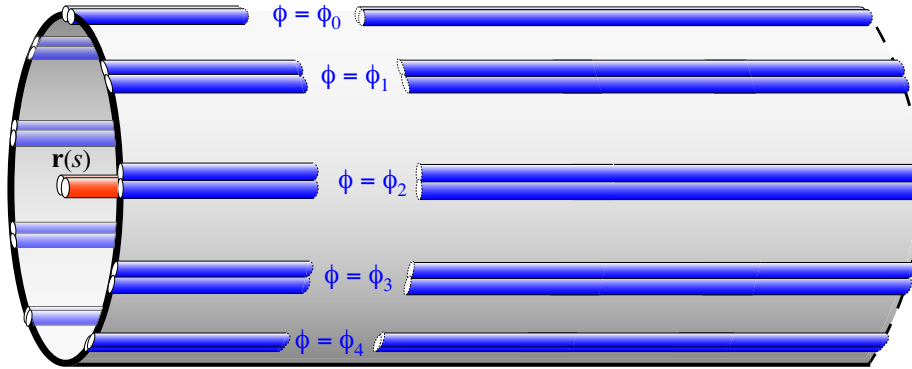


Figure 2.3: Illustration (not to scale) of the cylindrical surface of the axoneme in a straight configuration where the central line $\mathbf{r}(s)$ and lines of constant angle ϕ that can be thought of as the paths of the peripheral microtubule doublets are indicated.

2.2. Energetics

In order to determine the dynamic properties of the axoneme we need to find expressions for the elastic and viscous forces, which can be derived from a general enthalpy functional as formulated in this section. The elastic energy stored in a particular axonemal shape is given

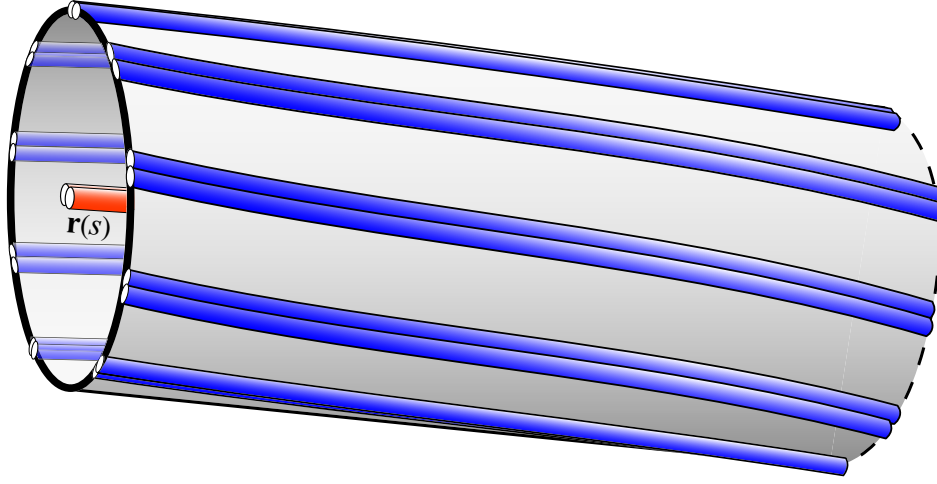


Figure 2.4: Illustration (not to scale) of the cylindrical surface of the axoneme in a bent and twisted configuration.

by integrals over the squared curvature and twist, respectively. So, denoting the length of the axoneme by L and defining the bending and twist rigidities as $\kappa_1, \kappa_2, \kappa_3$ we have

$$\mathcal{E}_{ela} = \int_0^L ds \left\{ \frac{\kappa_1}{2} \Omega_1(s)^2 + \frac{\kappa_2}{2} \Omega_2(s)^2 + \frac{\kappa_3}{2} \Omega_3(s)^2 \right\} .$$

Since we are interested in the change of the system's configuration as work is being done by the internal force generating elements, we look at the enthalpy rather than the energy of the system. Representing the activity of the motors by a local shear force density $f(s, \phi)$ in the direction tangential to the microtubules, i.e in the direction of $\mathbf{R}_s(s, \phi) \equiv \partial_s \mathbf{R}(s, \phi)$, the work done by the active elements is given by

$$\mathcal{E}_{act} = - \int_0^L ds \int_0^{2\pi} d\phi f(s, \phi) \Delta(s, \phi)$$

where $\Delta(s, \phi)$ is the infinitesimal local sliding displacement between neighbouring microtubule doublets. Subtracting \mathcal{E}_{act} from \mathcal{E}_{ela} and introducing a Lagrangian multiplier function $\Lambda(s)$, in order to ensure local inextensibility, the enthalpy functional of the axoneme is given by

$$G = \int_0^L ds \left\{ \frac{\kappa_1}{2} \Omega_1(s)^2 + \frac{\kappa_2}{2} \Omega_2(s)^2 + \frac{\kappa_3}{2} \Omega_3(s)^2 - \Lambda(s) + \int_0^{2\pi} d\phi f(s, \phi) \Delta(s, \phi) \right\} \quad (2.3)$$

Before we proceed we need to define consistently the somewhat arbitrary signs of the force density $f(s, \phi)$ and the infinitesimal local sliding $\Delta(s, \phi)$. They must be chosen to correctly reflect the chirality of the axoneme. The dynein motors are arranged such that they reach from one microtubule doublet to the neighbouring one in counterclockwise direction when viewed from the distal end² [25]. Recalling that dynein is a minus end directed motor and

²Recall that this is the conventional view in this thesis.

the microtubules are arranged such that their minus end corresponds to the basal end [12] it is natural to measure the shear force between neighbouring microtubule doublets as we go counterclockwise around the axoneme in distal direction, such that active motors correspond to a positive force. Hence, defining the sliding displacement as the difference in arclength between neighbouring microtubules as we go in counterclockwise direction, activity of motors will result in a negative sliding displacement.

In order to check whether these definitions reflect the axoneme's chirality, we look at the case in which all motors are active with a constant force at all times. As determined by the chirality of the motor-filament system, this will lead to a straight but twisted axoneme in which the peripheral microtubule doublets describe a right-handed helix. As apparent from Fig. 2.1 and Eq. (2.2) this corresponds to positive twist $\Omega_3(s)$. Hence, in our description such a force distribution should lead to an equilibrium configuration with positive twist $\Omega_3(s)$. This is indeed the case for our definitions as we show explicitly in the later section 5.1. Hence above definitions of $\Delta(s, \phi)$ and $f(s, \phi)$, which we use in the following, correctly represent the chirality of the biological structure.

2.2.1. Relating geometry to motor activity

There exists a one-to-one relationship between the geometrical configuration of the axoneme in three dimensions and the local sliding displacement. Hence we can find an expression for $\Delta(s, \phi)$ in terms of $\Omega_1(s), \Omega_2(s), \Omega_3(s)$, which we derive in the following by looking at the difference in arclength between neighbouring microtubules³. That is at a given point on the surface $\mathbf{R}(s, \phi)$ we go an infinitesimal distance in the direction that is orthogonal to the microtubule at $\mathbf{R}(s, \phi)$. So let $\mathbf{n}(s, \phi)$ be a unit vector that lies in the plane tangential to the axonemal surface at $\mathbf{R}(s, \phi)$ and satisfies $\mathbf{n}(s, \phi) \cdot \mathbf{R}_s(s, \phi) = 0$ as illustrated in Fig. 2.5, then the infinitesimal displacement is given by

$$\mathbf{R}(s', \phi') = \mathbf{R}(s, \phi) + \varepsilon \mathbf{n}(s, \phi) + \mathcal{O}(\varepsilon^2) \quad .$$

The arclength of the microtubule that goes through the point $\mathbf{R}(s, \phi)$ is given by

$$L(s, \phi) = \int_0^s ds' |\mathbf{R}_s(s', \phi)| \quad ,$$

and the quantity we are interested in is the rate of change of $L(s, \phi)$ in the direction of $\mathbf{n}(s, \phi)$, i.e.

$$\lim_{\varepsilon \rightarrow 0} \frac{L(s', \phi') - L(s, \phi)}{\varepsilon} \equiv \mathbf{n} \cdot \nabla L \quad , \quad (2.4)$$

where in the infinitesimal limit we have

$$L(s', \phi') - L(s, \phi) = (s' - s) \partial_s L(s, \phi) + (\phi' - \phi) \partial_\phi L(s, \phi) \quad . \quad (2.5)$$

Hence in order to determine the directional derivative, we need to determine the dependence of the infinitesimal co-ordinate changes $s' - s$ and $\phi' - \phi$ on ε , as described in the following.

³Or more precisely the change that corresponds to an infinitesimal displacement. Note, that in this section we often refrain from referring to densities and infinitesimal changes and for easier understanding simply refer to the equivalent quantities of the discrete structure.

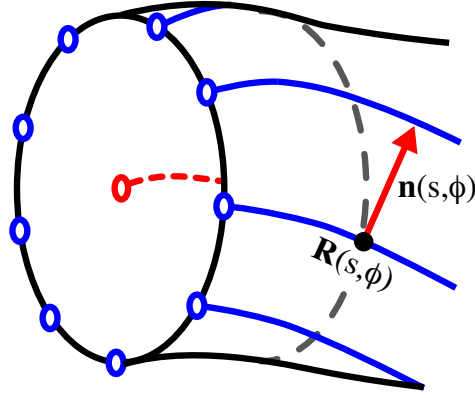


Figure 2.5: Sketch of the three dimensional geometry of the axonemal surface, illustrating with a red arrow the direction $\mathbf{n}(s, \phi)$ that is orthogonal to the microtubule at $\mathbf{R}(s, \phi)$. The dashed gray line indicates the $\mathbf{R}_\phi(s, \phi)$ direction. Note that in general for a non-zero $\Omega_3(s)$, the vectors defined by the partial derivatives $\mathbf{R}_s(s, \phi)$ and $\mathbf{R}_\phi(s, \phi)$ are not orthogonal to each other, implying that $\mathbf{n}(s, \phi)$ is not simply given by $\frac{\mathbf{R}_\phi}{|\mathbf{R}_\phi|}$.

Let us define the (non-orthogonal) unit vectors

$$\mathbf{e}_s = \frac{\mathbf{R}_s}{|\mathbf{R}_s|}, \quad \mathbf{e}_\phi = \frac{\mathbf{R}_\phi}{|\mathbf{R}_\phi|}$$

which span the tangent plane of the axonemal surface at $\mathbf{R}(s, \phi)$. Expressing $\mathbf{n}(s, \phi)$ in this co-ordinate system we have $\mathbf{n} = n_s \mathbf{e}_s + n_\phi \mathbf{e}_\phi$ and therefore in the infinitesimal limit

$$\varepsilon(n_s \mathbf{e}_s + n_\phi \mathbf{e}_\phi) = (s' - s) |\mathbf{R}_s| \mathbf{e}_s + (\phi' - \phi) |\mathbf{R}_\phi| \mathbf{e}_\phi \quad .$$

Multiplication with $\mathbf{e}_s, \mathbf{e}_\phi$ respectively, leads to a system of two equations, which yields

$$(\phi' - \phi) = \varepsilon \frac{n_\phi}{|\mathbf{R}_\phi|}, \quad (s' - s) = \varepsilon \frac{n_s}{|\mathbf{R}_s|}$$

which we can substitute into Eqs. 2.4 and 2.5 such that we arrive at

$$\mathbf{n} \cdot \nabla L = \frac{n_s}{|\mathbf{R}_s|} \partial_s L + \frac{n_\phi}{|\mathbf{R}_\phi|} \partial_\phi L \quad .$$

Using the above formulation, we can calculate the directional derivative, given expressions for $n_s, n_\phi, |\mathbf{R}_s|, |\mathbf{R}_\phi|, \partial_s L, \partial_\phi L$. As detailed in appendix A, this leads to the following result for $\Delta(s, \phi) = a \mathbf{n} \cdot \nabla L$ expanded in powers of a

$$\Delta(s, \phi) = -a^2 \Omega_3(s) + a \cos \phi \int_0^s \Omega_1(s') ds' + a \sin \phi \int_0^s \Omega_2(s') ds' + \mathcal{O}(a^3) \quad (2.6)$$

which can be written as

$$\Delta(s, \phi) = \Delta_0(s) + \Delta_1(s) \cos \phi + \Delta_2(s) \sin \phi + \text{h.o.t.} \quad (2.7)$$

where

$$\Delta_0(s) = -a^2 \Omega_3(s), \quad \Delta_1(s) = a \int_0^s \Omega_1(s') ds', \quad \Delta_2(s) = a \int_0^s \Omega_2(s') ds'$$

Note, that sign of $\mathbf{n}(s, \phi)$ is arbitrary, but the choice of signs in appendix A, corresponds to defining the normal $\mathbf{n}(s, \phi)$ such that it points leftward as seen from the tangent (going along the microtubules from base to tip). This is consistent with the definition of $\Delta(s, \phi)$ as discussed in the previous section as can be seen from Eq. (2.6), where a positive $\Omega_3(s)$ corresponds to a negative $\Delta(s, \phi)$.

This result for $\Delta(s, \phi)$ implies that the integral in the enthalpy functional defined by Eq. (2.3)

$$I = \int_0^{2\pi} d\phi f(s, \phi) \Delta(s, \phi)$$

only has contributions from following angular Fourier components of the force density

$$f(s, \phi) = f_0(s) + f_1(s) \cos \phi + f_2(s) \sin \phi + \text{h.o.t.}$$

with

$$\begin{aligned} I &= 2\pi \Delta_0 f_0 + \pi \Delta_1 f_1 + \pi \Delta_2 f_2 + \text{h.o.t.} \\ &= -2\pi a^2 \Omega_3 f_0 + a\pi f_1 \int_0^s \Omega_1(s') ds' + a\pi f_2 \int_0^s \Omega_2(s') ds' \end{aligned}$$

Where for $i = 1, 2$ we can integrate terms of following form by parts

$$\begin{aligned} \int_0^L f_i(s) ds \int_0^s \Omega_i(s') ds' &= \left[\int_0^s f_i(s') ds' \int_0^s \Omega_i(s') ds' \right]_{s=0}^{s=L} - \int_0^L \Omega_i(s) ds \int_0^s f_i(s') ds' \\ &= \int_0^L \Omega_i(s) ds \int_s^L f_i(s') ds' \end{aligned}$$

For notational convenience introducing $F_i(s) = -\int_s^L f_i(s') ds'$ we finally obtain

$$\begin{aligned} G = \int_0^L ds \left\{ \frac{\kappa_1}{2} \Omega_1(s)^2 + \frac{\kappa_2}{2} \Omega_2(s)^2 + \frac{\kappa_3}{2} \Omega_3(s)^2 - \Lambda(s) \right. \\ \left. - (2\pi a^2 \Omega_3(s) f_0(s) + a\pi \Omega_1(s) F_1(s) + a\pi \Omega_2(s) F_2(s)) \right\} \quad (2.8) \end{aligned}$$

which is the three dimensional generalisation of the enthalpy functional presented in [106] and extends the existing discussion of passive three-dimensional filament dynamics [11,107] to actively bending filaments.

2.2.2. Virtual displacements

We proceed by calculating the variations of G given small changes in the axonemal configuration. In order to do so, we first need to find expressions for $\delta(ds)$, $\delta\mathbf{e}_1$, $\delta\mathbf{e}_2$, $\delta\mathbf{e}_3$ in terms

of variations in the axonemal configuration, namely changes in $\mathbf{r}(s)$, $\mathbf{e}_1(s)$, $\mathbf{e}_2(s)$. As derived in appendix B we find

$$\begin{aligned}\delta\mathbf{e}_1 &= \delta\chi\mathbf{e}_2 - (\mathbf{e}_1 \cdot (\delta\mathbf{r})_s)\mathbf{e}_3 \\ \delta\mathbf{e}_2 &= -\delta\chi\mathbf{e}_1 - (\mathbf{e}_2 \cdot (\delta\mathbf{r})_s)\mathbf{e}_3 \\ \delta\mathbf{e}_3 &= (\delta\mathbf{r})_s - (\mathbf{e}_3 \cdot (\delta\mathbf{r})_s)\mathbf{e}_3 \\ \delta(ds) &= (\mathbf{e}_3 \cdot (\delta\mathbf{r})_s)ds\end{aligned}$$

where we have introduced the rotation angle

$$\delta\chi = \mathbf{e}_2 \cdot \delta\mathbf{e}_1 \quad .$$

Above quantities are related to $\delta\Omega_1(s)$, $\delta\Omega_2(s)$, $\delta\Omega_3(s)$ as shown below (and derived in appendix B)

$$\begin{aligned}\delta\Omega_1 &= \delta\chi\Omega_2 - \mathbf{e}_2 \cdot (\delta\mathbf{r})_{ss} - 2\Omega_1\mathbf{e}_3 \cdot (\delta\mathbf{r})_s \\ \delta\Omega_2 &= -\delta\chi\Omega_1 + \mathbf{e}_1 \cdot (\delta\mathbf{r})_{ss} - 2\Omega_2\mathbf{e}_3 \cdot (\delta\mathbf{r})_s \\ \delta\Omega_3 &= (\delta\chi)_s + (\Omega_1\mathbf{e}_1 + \Omega_2\mathbf{e}_2 - \Omega_3\mathbf{e}_3) \cdot (\delta\mathbf{r})_s \quad .\end{aligned}\tag{2.9}$$

These equations depend only on the geometry and are independent of the enthalpy functional. They have been derived previously in studies discussing different systems with the same geometrical set up, such as the filamentous structures formed by rod-shaped bacteria *B. subtilis* [107,108], and allow us to compute the variations of $G = \int_0^L dsH$

$$\delta G = \int_0^L \delta(dsH) = \int_0^L \delta(ds)H + \int_0^L ds\delta H$$

where

$$\delta H = (\kappa_1\Omega_1 - \pi aF_1)\delta\Omega_1 + (\kappa_2\Omega_2 - \pi aF_2)\delta\Omega_2 + (\kappa_3\Omega_3 - 2\pi a^2f_0)\delta\Omega_3$$

Partial integration (see appendix C) leads to

$$\delta G = \text{B.T.} + \int_0^L \left(\frac{\delta G}{\delta\mathbf{r}} \delta\mathbf{r} + \frac{\delta G}{\delta\chi} \delta\chi \right) ds$$

where

$$\boxed{\begin{aligned}\frac{\delta G}{\delta\mathbf{r}} &= \partial_s \left[\mathbf{e}_1 (2\pi a^2 f_0 \Omega_1 - a\pi (F_1 \Omega_3 + f_2) - (\kappa_3 - \kappa_1) \Omega_1 \Omega_3 + \kappa_2 \dot{\Omega}_2) \right. \\ &\quad + \mathbf{e}_2 (2\pi a^2 f_0 \Omega_2 - a\pi (F_2 \Omega_3 - f_1) - (\kappa_3 - \kappa_2) \Omega_2 \Omega_3 - \kappa_1 \dot{\Omega}_1) \\ &\quad \left. + \mathbf{e}_3 \left(\underbrace{\Lambda + \frac{\kappa_1}{2} \Omega_1^2 + \frac{\kappa_2}{2} \Omega_2^2 + \frac{\kappa_3}{2} \Omega_3^2}_{-\tau} \right) \right]\end{aligned}}\tag{2.10}$$

and

$$\boxed{\frac{\delta G}{\delta\chi} = a\pi (F_2 \Omega_1 - F_1 \Omega_2) + 2\pi a^2 f_0 - \kappa_3 \dot{\Omega}_3 + (\kappa_1 - \kappa_2) \Omega_1 \Omega_2}\tag{2.11}$$

In the above equation, and for the remainder of this thesis, dotted quantities refer to derivatives with respect to the arclength, e.g. $\dot{\Omega}_3 = \partial_s \Omega_3$. Note that as defined above the quantity $\tau(s)$ plays the role of the physical tension as can be seen from

$$\tau(s) = \mathbf{e}_3 \cdot \left(\mathbf{F}_{ext}(L) + \int_s^L ds' \frac{\delta G}{\delta \mathbf{r}} \right)$$

The boundary terms B.T. are detailed in appendix C.

2.3. Overdamped dynamics

The ratio of inertial forces and viscous forces for an object moving in a fluid is estimated by the dimensionless Reynolds number

$$Re = \frac{\rho v l}{\mu}$$

where l is a characteristic length scale⁴ of the moving object, v the velocity of the motion, ρ the fluid density and μ the fluid's dynamic viscosity. We substitute the values of $l = 10^{-6}\text{m}$, $v = 10^{-2}\frac{\text{m}}{\text{s}}$, $\rho = 10^3\frac{\text{kg}}{\text{m}^3}$ and $\mu = 10^{-3}\frac{\text{kg}}{\text{ms}}$, where the velocity corresponds to the highest observed beat frequency of 100Hz with an amplitude of $50\mu\text{m}$. The value for the velocity is an extreme estimate, leading to an upper bound of the Reynolds number of $Re \approx 10^{-2}$. Hence, we conclude that in the discussion of axonemal dynamics inertial terms can be neglected. Additionally, we simplify the problem by ignoring hydrodynamic interactions between different parts of the beating axoneme, which are expected to have minor effects [109]. Looking at the local fluid friction, this leads to following force and moment balancing equations, where we have introduced the perpendicular, tangential and rotational viscous friction coefficients $\xi_{\perp}, \xi_{\parallel}, \xi_r$ as illustrated in Fig. 2.6.

$$\partial_t \mathbf{r} = - \left(\frac{1}{\xi_{\perp}} (\mathbf{e}_1 \mathbf{e}_1 + \mathbf{e}_2 \mathbf{e}_2) + \frac{1}{\xi_{\parallel}} \mathbf{e}_3 \mathbf{e}_3 \right) \frac{\delta G}{\delta \mathbf{r}} \quad (2.12)$$

$$\partial_t \chi = - \frac{1}{\xi_r} \frac{\delta G}{\delta \chi} \quad (2.13)$$

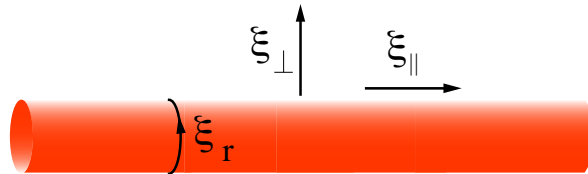


Figure 2.6: Using a local approximation we describe the hydrodynamic effects of the surrounding fluid on the cylindrical filament in the form of a parallel and perpendicular friction coefficient.

⁴Note, it is the diameter rather than the length of the flagellum that is of relevance in this problem [84].

2.3.1. Incompressibility constraint

In order to complete the equations that determine the dynamics we enforce local incompressibility, and therefore the total length of the axoneme. We require

$$\begin{aligned} |\mathbf{r}_s|^2 &= 1 \\ \Rightarrow \partial_t(\mathbf{r}_s \cdot \mathbf{r}_s) &= 2\mathbf{r}_s \cdot (\partial_t \mathbf{r})_s = 0 \end{aligned}$$

or equivalently

$$\mathbf{e}_3 \cdot (\partial_t \mathbf{r})_s = 0 \quad . \quad (2.14)$$

Which is a complicated non-linear expression in $\Omega_1, \Omega_2, \Omega_3, \tau$ of the form

$$\ddot{\tau} - \frac{\xi_{\parallel}}{\xi_{\perp}} (\Omega_1^2 + \Omega_2^2) \tau = \dots \quad (2.15)$$

where the right hand side is given in detail in appendix D.

2.3.2. Dynamic equations

Making use of Eq. (2.9) for $\delta \mathbf{r} = \mathbf{r}_t \delta t, \delta \chi = \chi_t \delta t$ together with the incompressibility constraint Eq. (2.14) we find

$$\begin{aligned} \partial_t \Omega_1 &= \chi_t - \mathbf{e}_2 \cdot \partial_{ss}(\mathbf{r}_t) \\ \partial_t \Omega_2 &= -\chi_t - \mathbf{e}_1 \cdot \partial_{ss}(\mathbf{r}_t) \\ \partial_t \Omega_3 &= \partial_s(\chi_t) + (\Omega_1 \mathbf{e}_1 + \Omega_2 \mathbf{e}_2) \cdot \partial_s(\mathbf{r}_t) \end{aligned}$$

To obtain the equations of motion for $\Omega_1, \Omega_2, \Omega_3, \tau$ we substitute the force and moment balancing equations (2.10) and (2.11) into these expressions, defining the dynamic equations of the form

$$\xi_{\perp} \partial_t \Omega_1 + \kappa_1 \ddot{\Omega}_1 - a\pi \ddot{\Gamma}_1 = \dots \quad (2.16)$$

$$\xi_{\perp} \partial_t \Omega_2 + \kappa_2 \ddot{\Omega}_2 - a\pi \ddot{\Gamma}_2 = \dots \quad (2.17)$$

$$\xi_r \partial_t \Omega_3 - \kappa_3 \ddot{\Omega}_3 + 2a^2 \pi \ddot{\Gamma}_0 = \dots \quad . \quad (2.18)$$

The rather long and complicated full expressions of the right hand sides can be found in appendix D.

2.3.3. Boundary conditions

The boundary terms as derived in appendix D are balanced by the externally applied forces, torques and moments at the ends implying that for general boundary conditions we

have:

At $s = 0$

$$\begin{aligned}\mathbf{F}_{ext} &= -[\mathbf{e}_1(2\pi a^2 f_0 \Omega_1 - a\pi(F_1 \Omega_3 + f_2) - (\kappa_3 - \kappa_1)\Omega_1 \Omega_3 + \kappa_2 \dot{\Omega}_2) \\ &\quad + \mathbf{e}_2(2\pi a^2 f_0 \Omega_2 - a\pi(F_2 \Omega_3 - f_1) - (\kappa_3 - \kappa_2)\Omega_2 \Omega_3 - \kappa_1 \dot{\Omega}_1) - \mathbf{e}_3 \tau] \\ T_{ext,1} &= -\kappa_2 \Omega_2 + \pi a F_2 \\ T_{ext,2} &= \kappa_1 \Omega_1 - \pi a F_1 \\ \mathbf{M} \cdot \mathbf{e}_3 &= -\kappa_3 \Omega_3 + 2\pi a^2 f_0\end{aligned}$$

At $s = L$

$$\begin{aligned}\mathbf{F}_{ext} &= \mathbf{e}_1(2\pi a^2 f_0 \Omega_1 - a\pi f_2 - (\kappa_3 - \kappa_1)\Omega_1 \Omega_3 + \kappa_2 \dot{\Omega}_2) \\ &\quad + \mathbf{e}_2(2\pi a^2 f_0 \Omega_2 + a\pi f_1 - (\kappa_3 - \kappa_2)\Omega_2 \Omega_3 - \kappa_1 \dot{\Omega}_1) - \mathbf{e}_3 \tau \\ T_{ext,1} &= \kappa_2 \Omega_2 \\ T_{ext,2} &= -\kappa_1 \Omega_1 \\ \mathbf{M} \cdot \mathbf{e}_3 &= \kappa_3 \Omega_3 - 2\pi a^2 f_0\end{aligned}$$

Looking at the case in which the base of the axoneme is clamped, we impose $\delta \mathbf{r} = (\delta \mathbf{r})_s = \delta \chi = 0$ at $s = 0$ implying that the necessary condition for the boundary terms to vanish at $s = 0$ is given by

$$\begin{aligned}\partial_t \mathbf{r}(0) &= 0 \\ \partial_t \mathbf{r}_s(0) &= 0 \\ \partial_t \chi(0) &= 0 \quad .\end{aligned}$$

These conditions can be expressed as conditions on $\Omega_1, \Omega_2, \Omega_3, \tau$ making use of equations (2.12) and (2.13) as detailed in appendix D. At the free end no external forces, torques or moments are acting. Hence we solve above expressions for $\mathbf{F}_{ext} = T_{ext,1} = T_{ext,2} = \mathbf{M} \cdot \mathbf{e}_3 = 0$ at $s = L$ leading to

$$\begin{aligned}\Omega_1(L) &= 0 & \Omega_2(L) &= 0 \\ \dot{\Omega}_1(L) &= \frac{a\pi f_1}{\kappa_1} & \dot{\Omega}_2(L) &= \frac{a\pi f_2}{\kappa_2} \\ \Omega_3(L) &= \frac{2\pi a^2 f_0}{\kappa_3} & \tau(L) &= 0\end{aligned}$$

Planar motion

In the previous chapter we derived general three-dimensional equations defining axonemal beat patterns. In order to compare quantitatively our results to experimental data from bull sperm [30] we look in the following at the limit in which we confine the solutions of equations (2.15)-(2.18) to two dimensions, i.e. we let

$$\kappa_2, \kappa_3, \rightarrow \infty \Rightarrow \Omega_2, \Omega_3 \rightarrow 0 \quad .$$

The quantity that is traditionally used to analyse flagellar beat patterns is the local shear angle – the angle between the flagellum and the axis defined by the position of the head, as illustrated in Fig. 3.1. Hence we change our notation from the curvature $\Omega_1(s)$ to the local shear angle $\psi(s)$ according to following relation

$$\psi(s, t) = \psi_0(t) + \int_0^s \Omega_1(s', t) ds' \quad .$$

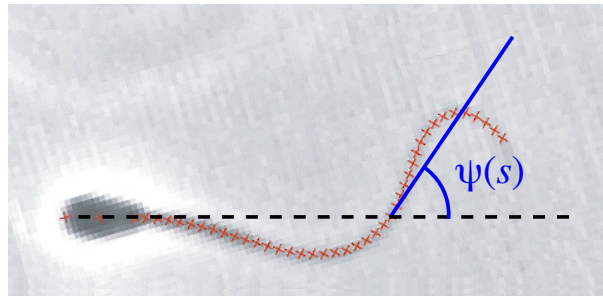


Figure 3.1: Definition of the local shear angle $\psi(s)$.

The constraints as defined above impose that Ω_2, Ω_3 as well as f_0, f_2 are zero. As derived in appendix D the planar limit Eq. (2.15)-(2.18) become (see appendix D)

$$\begin{aligned}\partial_t \psi &= \frac{1}{\xi_\perp} (-\kappa \ddot{\psi} + a\dot{f} + \dot{\tau}\dot{\psi} + \tau\ddot{\psi}) + \frac{1}{\xi_\parallel} (\kappa\dot{\psi}^2\ddot{\psi} - a\dot{f}\dot{\psi}^2 + \dot{\tau}\dot{\psi}) \\ \ddot{\tau} - \frac{\xi_\parallel}{\xi_\perp} \dot{\psi}^2 \tau &= a(\dot{f}\dot{\psi} + f\ddot{\psi}) - \kappa(\ddot{\psi}^2 + \dot{\psi}\ddot{\psi}) + \frac{\xi_\parallel}{\xi_\perp} (a\dot{f}\dot{\psi} - \kappa\dot{\psi}\ddot{\psi})\end{aligned}$$

where we have re-written $\kappa_1, \pi f_1$, as κ, f respectively. These coupled differential equations describe the planar beat of the three-dimensional axoneme and are the same as reported previously in [106]. Note that they can be derived from a two-dimensional enthalpy functional using the same variational approach in the zero Reynolds number limit as discussed in the preceding chapter.

$$G_0 = \int_0^L ds \left\{ \frac{\kappa}{2} C(s) + f(s)\Delta(s) - \Lambda(s) \right\} \quad (3.1)$$

where $C(s)$ is the curvature in the plane of beat, equivalent to $\Omega_1(s)$, and $\Delta(s)$ replaces $\Delta_1(s)$ of the three-dimensional sliding on the axonemal surface as defined in Eq. (2.7). This enthalpy functional can be interpreted as a “two-dimensional axoneme”, with two sliding filaments as indicated by Fig. 3.2 connected by molecular motors in both directions.

In this chapter we extend the existing discussion of planar beats [106] in several ways.

- We take into account that the connection of the microtubules at the base is not totally rigid and therefore introduce a finite stiffness k_s and friction γ describing the basal connection. As shown in this chapter the resulting non-zero basal sliding Δ_0 is an effect that significantly influences the possible beat patterns. This is the first study where this effect is proposed on theoretical grounds. Our analysis is supported by recent direct observation of basal sliding of microtubules in mouse spermatozoa [28].
- We unify and extend the existing discussion of boundary conditions by introducing a torsional spring with angular rigidity k_p , that effectively describes a pivoting connection of the basal body around a stationary reference point.
- Finally we solve the equations of motion not only in the limit of infinitesimal amplitudes, but for the first time discuss the system’s behaviour away from the bifurcation point enabling us to understand axonemal beat patterns as solutions to a non-linear wave equation.

The extensions at the boundary as described above leads to following additional terms

$$\begin{aligned}\mathcal{E}_s &= \frac{k_s}{2} \Delta_0^2 \\ \mathcal{E}_p &= \frac{k_p}{2} \psi(0)^2\end{aligned}$$

corresponding to the elastic energies of basal sliding and basal pivoting, such that the enthalpy functional takes the form

$$G = G_0 + \mathcal{E}_p + \mathcal{E}_s \quad . \quad (3.2)$$

In this two dimensional notation, the local sliding displacement $\Delta(s, t)$ is related to the shear-angle $\psi(s, t)$ as follows.

$$\Delta(s, t) = \Delta_0(t) + a(\psi(s, t) - \psi(0, t)) \quad , \quad (3.3)$$

such that the filament shape $\mathbf{r}(s, t)$ can be reconstructed from the local shear-angle $\psi(s, t)$ by

$$\mathbf{r}(s, t) = \mathbf{r}(0, t) + \int_0^s (\cos \psi(s', t), \sin \psi(s', t)) ds' \quad . \quad (3.4)$$

Note that the discussion presented in this section is equivalent to the one of a two-dimensional axoneme of width a . In order to interpret the results about basal sliding derived in the following we keep in mind that the quantities involved are the angular Fourier component $\Delta_1(s), f_1(s)$ of the three-dimensional quantities $\Delta(s, \phi), f(s, \phi)$ describing the forces and sliding in the three-dimensional axoneme.

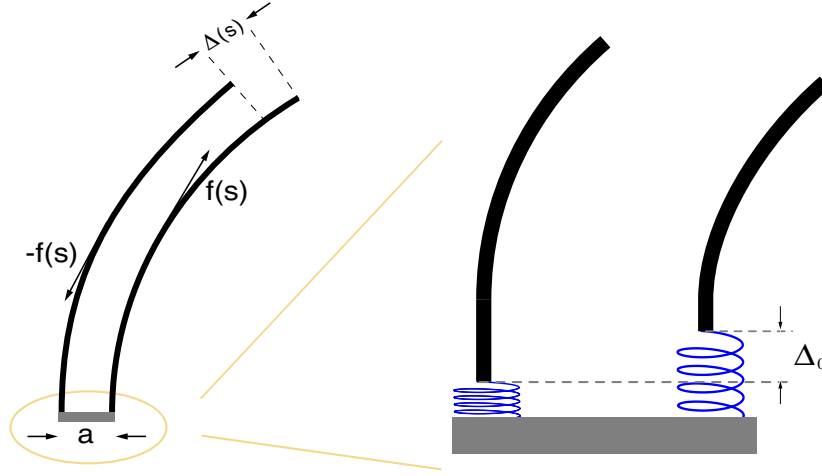


Figure 3.2: Illustrating the “two-dimensional axoneme” in which two filaments slider relative to each other. Indicated are the local sliding displacement $\Delta(s)$ the internal shear force $f(s)$ and the diameter a . Note the elastic connection of the microtubules at the base allowing for basal sliding.

3.1. Dynamic equations

Matching viscous and elastic forces at the basal body implies

$$\gamma \partial_t \Delta_0 = -\frac{\partial G}{\partial \Delta_0}$$

where the coefficient γ describes the effective friction of microtubules sliding at the basal end. This leads to an additional equation describing the dynamics of the basal sliding

$$\Delta_0 = -\frac{1}{i\omega\gamma + k_s} \int_0^L f(s) ds \quad . \quad (3.5)$$

The differential equations in $\psi(s, t)$ and $\tau(s, t)$ are supplemented by the appropriate boundary conditions. The three-dimensional boundary conditions lead to a two-dimensional limit as given in appendix D, which can be extended to include a pivoting head and basal sliding.

At $s = 0$	At $s = 1$
$\kappa\dot{\psi} + a \int_0^L f(s)ds - k_p\psi = 0$	$\dot{\psi} = 0$
$\kappa\ddot{\psi} - a\dot{f} - \dot{\psi}\tau = 0$	$\kappa\ddot{\psi} - af = 0$
$\kappa\dot{\psi}\ddot{\psi} - af\dot{\psi} + \dot{\tau} = 0$	$\tau = 0$

Which is the most general form of the boundary conditions, whose properties we discuss in following limiting cases:

- Clamped head without basal sliding $k_s, k_p \rightarrow \infty$
- Clamped head with basal sliding $k_p \rightarrow \infty$
- Freely pivoting head without basal sliding $k_s \rightarrow \infty, k_p \rightarrow 0$

Frequency representation

Making the following Fourier mode ansatz

$$\begin{aligned} f(s, t) &= \sum_n \tilde{f}^{(n)}(s) e^{in\omega t} \\ \Delta(s, t) &= \sum_n \tilde{\Delta}^{(n)}(s) e^{in\omega t} \\ \psi(s, t) &= \sum_n \tilde{\psi}^{(n)}(s) e^{in\omega t} \end{aligned}$$

we discuss the oscillatory motion in frequency space. In this representation we can make use of a previous result relating the first Fourier modes of the force and local sliding displacement of a collection of many molecular motors acting against an elastic element. It has been shown [101,110,111] that such a system undergoes a phase transition as it is driven away from equilibrium. Defining Ω as a critical parameter describing how far the system is out of equilibrium, the collective properties can be summarised as follows. For $\Omega < \Omega_c$ the force-velocity curve for such a system is similar to that of a single motor [112–115], whereas far enough away from equilibrium at $\Omega = \Omega_c$ the force-velocity curve exhibits a singularity which leads to hysteretic behaviour for $\Omega > \Omega_c$, with instabilities and discontinuities in the force-velocity curve as illustrated in Fig. 3.3. The signature of such a dynamical phase transition for a collection of molecular motors has been observed experimentally in an actin-myosin system [116]. This non-intuitive property of a collection of many molecular motors naturally leads to spontaneous oscillations as observed e.g. in skeletal muscle [102,103]. Such spontaneous oscillations due to a dynamic instability have been implicated as the underlying mechanisms in many cellular systems that exhibit oscillations [117,118]. In addition to the discussion of axonemal beat patterns [105,106] the most prominent examples are the hair cells of the inner ear [119–121] and mitotic spindle oscillations [122,123]. For small amplitudes close to the bifurcation point, the general expansion relating the first time-like Fourier modes can be truncated at the first non-linear term

$$\tilde{f}^{(1)} = \chi_{lin} \tilde{\Delta}^{(1)} + \chi_{nl} \tilde{\Delta}^{(1)} |\tilde{\Delta}^{(1)}|^2 + \text{h.o.t.} \quad (3.6)$$

which leads to three coupled ordinary differential equations for the dominant Fourier modes of ψ and τ . We discuss this non-linear problem treating χ_{lin}, χ_{nl} as constant, which enables

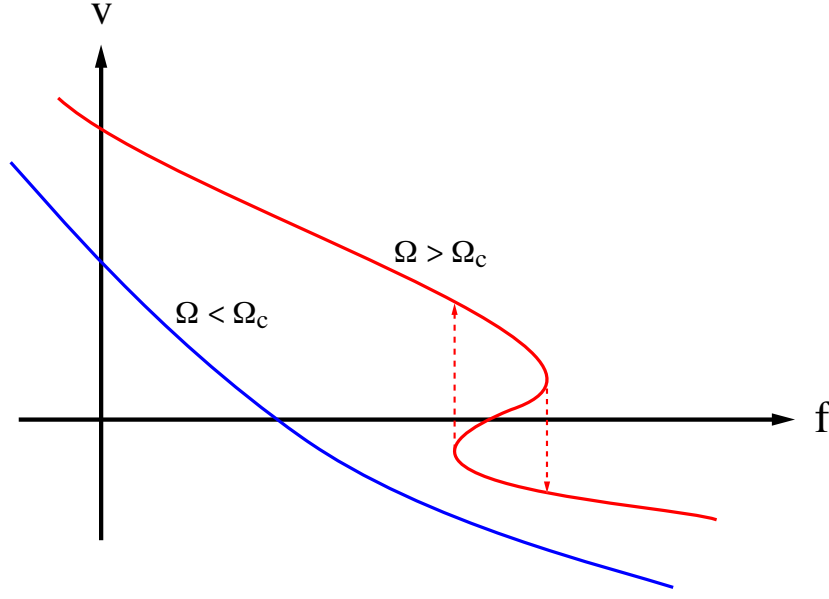


Figure 3.3: Sliding velocity of a collection of motors as a function of the resistive force as discussed in [101,110,111]. The blue curve describing the system's properties for $\Omega < \Omega_c$ resembles that of a single motor [112–115]. For $\Omega > \Omega_c$ the system's behaviour is qualitatively different and can lead to spontaneous oscillations as indicated by the dashed arrows on red curve.

us to determine of finite amplitude non-linear waves and see how they compare to linearly unstable solutions.

For notational brevity we conveniently drop the tildes and write $\psi = \tilde{\psi}^{(1)}$, $\Delta = \tilde{\Delta}^{(1)}$. Rescaling the parameters we arrive at following dimensionless quantities

$$\begin{aligned}
 \beta &= \frac{\xi_{\perp}}{\xi_{\parallel}} & \bar{\omega} &= \frac{\omega L^4}{\kappa} \xi_{\perp} \\
 \bar{\chi}_{lin} &= \frac{a^2 L^2}{\kappa} \chi_{lin} & \bar{\chi}_{nl} &= \frac{a^4 L^2}{\kappa} \chi_{nl} \\
 s' &= \frac{s}{L} & \tau'_i(s') &= \frac{L^2}{\kappa} \tau_i(s) \\
 \bar{k}_s &= \frac{a^2 L}{\kappa} k_s & \bar{\gamma} &= \frac{a^2}{L^3 \xi_{\perp}} \gamma \\
 \bar{k}_p &= \frac{L}{\kappa} k_p & \Delta'_0 &= \frac{1}{a} \Delta_0
 \end{aligned}$$

which leads to the following set of coupled ordinary differential equations.

$$\begin{aligned}
 i\bar{\omega}\psi &= -\ddot{\psi} + \bar{\chi}_{lin}\ddot{\psi} + \bar{\chi}_{nl}\partial_s^2[(\psi + \Delta_0^{lin} - \psi(0))|\psi + \Delta_0^{lin} - \psi(0)|^2] + \partial_s(\tau_0\dot{\psi} + \tau_2\dot{\psi}^*) \\
 &\quad + \beta \left[\partial_s(|\dot{\psi}|^2\dot{\psi}) - 2\bar{\chi}_{lin}(\psi + \Delta_0^{lin} - \psi(0))|\dot{\psi}|^2 - \bar{\chi}_{lin}^*(\psi^* + (\Delta_0^{lin})^* - \psi(0)^*)\dot{\psi}^2 + \dot{\tau}_0\dot{\psi} + \dot{\tau}_2\dot{\psi}^* \right] \\
 \ddot{\tau}_0 &= 2\text{Re}\{\bar{\chi}_{lin}\partial_s[(\psi + \Delta_0^{lin} - \psi(0))\dot{\psi}^*]\} - \partial_s^2(|\dot{\psi}|^2) + 2\beta^{-1} \left(|\dot{\psi}|^2 \text{Re}\{\bar{\chi}_{lin}\} - \text{Re}\{\dot{\psi}^*\ddot{\psi}\} \right) \\
 \ddot{\tau}_2 &= \bar{\chi}_{lin}\partial_s[(\psi + \Delta_0^{lin} - \psi(0))\dot{\psi}] - \partial_s(\dot{\psi}\ddot{\psi}) + \beta^{-1} \left(\bar{\chi}_{lin}\dot{\psi}^2 - \dot{\psi}\ddot{\psi} \right)
 \end{aligned}$$

(3.7)

Where the general boundary conditions for the Fourier modes are given by

$$\begin{aligned}
\bar{k}_p \psi(0) &= \dot{\psi}(0) + \bar{\chi}_{lin} \int_0^1 [\psi(s) + \Delta_0^{lin} - \psi(0)] ds \\
&\quad + \bar{\chi}_{nl} \int_0^1 [|\psi(s) + \Delta_0^{lin} - \psi(0)|^2 (\psi(s) + \Delta_0^{lin} - \psi(0))] ds \\
\ddot{\psi}(0) &= \bar{\chi}_{lin} \dot{\psi}(0) + \dot{\psi}(0) \tau_0(0) + \dot{\psi}^*(0) \tau_2(0) \\
&\quad + \bar{\chi}_{nl} (2|\Delta_0^{lin}|^2 \dot{\psi}(0) + (\Delta_0^{lin})^2 \dot{\psi}^*(0)) \\
\dot{\tau}_0(0) &= -\partial_s (|\dot{\psi}(0)|^2) + 2\text{Re} \left\{ \bar{\chi}_{lin} \Delta_0^{lin} \dot{\psi}^*(0) \right\} \\
\dot{\tau}_2 &= -\dot{\psi}(0) \ddot{\psi}(0) + \bar{\chi}_{lin} \Delta_0^{lin} \dot{\psi}(0) \\
\dot{\psi}(1) &= 0 \\
\ddot{\psi}(1) &= \bar{\chi}_{lin} (\psi(1) + \Delta_0^{nl} + \psi(0)) \\
&\quad + \bar{\chi}_{nl} |\psi(1) + \Delta_0^{lin} - \psi(0)|^2 (\psi(1) + \Delta_0^{lin} - \psi(0)) \\
\tau_0(1) &= 0 \\
\tau_2(1) &= 0
\end{aligned} \tag{3.8}$$

and Δ_0^{lin} and Δ_0^{nl} are the basal sliding terms expressed up to $\mathcal{O}(\psi)$ and $\mathcal{O}(\psi^3)$ respectively. They are explicitly given by

$$\begin{aligned}
\Delta_0^{lin} &= -\frac{\bar{\chi}_{lin}}{i\bar{\omega}\bar{\gamma} + \bar{k}_s + \bar{\chi}_{lin}} \int_0^1 \psi(s) ds \\
\Delta_0^{nl} &= \Delta_0^{lin} - \frac{\bar{\chi}_{nl}}{i\bar{\omega}\bar{\gamma} + \bar{k}_s + \bar{\chi}_{lin}} \int_0^1 |\psi(s) + \Delta_0^{lin}|^2 (\psi(s) + \Delta_0^{lin}) ds
\end{aligned}$$

In the limit of the our set of boundary conditions, the above expression simplifies as follows

- Clamped head without basal sliding $\Rightarrow \Delta_0^{lin}, \psi(0) = 0$
- Clamped head with basal sliding $\Rightarrow \psi(0) = 0$
- Freely pivoting head without basal sliding $\Rightarrow \Delta_0^{lin} = 0$

3.2. Non-linear solutions – an analytical expansion

In this section we discuss solutions to the non-linear problem close to the bifurcation. Making use of the linear modes, we find an analytical expression for the amplitude with which the solution grows out of the bifurcation point. That is for a point close to a bifurcation with $\bar{\chi}_{lin} = \bar{\chi}_c + \Delta\bar{\chi}, \bar{\omega} = \bar{\omega}_c + \Delta\bar{\omega}$ we expand the amplitude of the non-linear modes perturbatively up to $\mathcal{O}(\epsilon^3)$ by making the following ansatz

$$\Delta\bar{\chi} = \rho e^{i\theta} \epsilon^2 \text{ and } \Delta\bar{\omega} = \mu \epsilon^2 \tag{3.9}$$

$$\psi_{nl}(s) = \epsilon \psi_0(s) + \epsilon^3 \psi_1(s) + \text{h.o.t.} \tag{3.10}$$

$$\tau_{0,nl}(s) = \epsilon^2 \tau_0(s) + \text{h.o.t.} \tag{3.11}$$

$$\tau_{2,nl}(s) = \epsilon^2 \tau_2(s) + \text{h.o.t.} \tag{3.12}$$

for some unknown values of $\epsilon, \rho, \mu, \theta \in \mathbb{R}$. In order to match terms of different orders of ϵ we re-write the non-linear problem 3.7 using the linear operator

$$\mathcal{L}(\bar{\chi}_{lin}, \bar{\omega}) = i\bar{\omega} + \partial_s^4 - \bar{\chi}_{lin} \partial_s^2$$

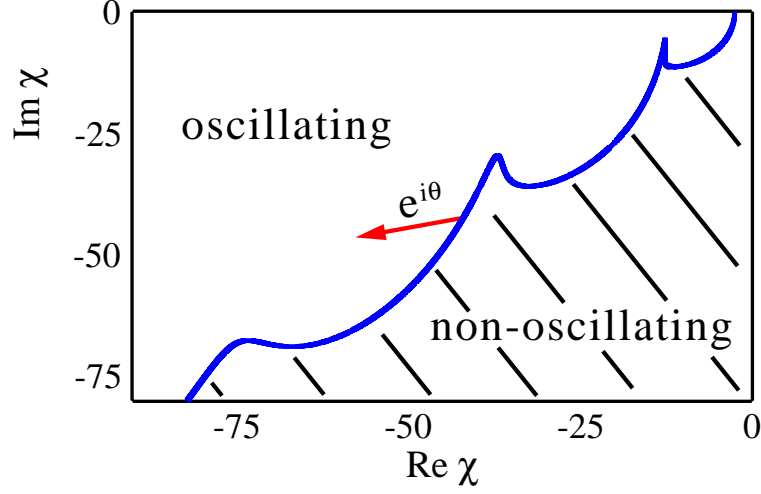


Figure 3.4: Schematic diagram, showing the critical line and how it separates a non-oscillatory region where the zero solution is stable, and an oscillatory region where a non-zero mode becomes linearly unstable. At a bifurcation point corresponding to a particular frequency ω_c the red arrow indicates the direction of $\Delta\chi \sim e^{i\theta}$ in which we go away from the instability in order to discuss finite amplitude oscillations.

which we can formally Taylor expand close to the bifurcation such that

$$\mathcal{L}(\bar{\chi}_{lin}, \bar{\omega}) = \underbrace{\mathcal{L}(\bar{\chi}_c, \bar{\omega}_c)}_{\mathcal{L}_c} - \Delta\bar{\chi}\partial_s^2 + i\Delta\bar{\omega} \quad . \quad (3.13)$$

Matching $\mathcal{O}(\epsilon)$ terms gives rise to a linear problem, defining $\psi_0(s)$ as a solution (arbitrarily normalised) to following linear differential equation

$$\mathcal{L}_c\psi_0(s) = 0 \quad (3.14)$$

subject to the appropriate boundary conditions, which for the three different cases are defined in equations (E.2,E.5,E.8) of appendix E.

Matching $\mathcal{O}(\epsilon^2)$ terms leads to the following definitions of the non-linear corrections of τ_0 and τ_2 ,

$$\begin{aligned} \ddot{\tau}_0(s) &= 2\text{Re}\{\bar{\chi}_c\partial_s[(\psi_0 + \Delta_0^0 - \psi_0(0))\dot{\psi}_0^*]\} - \partial_s^2(|\dot{\psi}_0|^2) + 2\beta^{-1}\left(|\dot{\psi}_0|^2\text{Re}\{\bar{\chi}_c\} - \text{Re}\{\dot{\psi}_0^*\ddot{\psi}_0\}\right) \\ &\equiv \mathcal{N}_2(\psi_0^2) \\ \ddot{\tau}_2(s) &= \bar{\chi}_c\partial_s[(\psi_0 + \Delta_0^0 - \psi_0(0))\dot{\psi}_0] - \partial_s(\dot{\psi}_0\ddot{\psi}_0) + \beta^{-1}\left(\bar{\chi}_c\dot{\psi}_0^2 - \dot{\psi}_0\ddot{\psi}_0\right) \\ &\equiv \mathcal{N}_3(\psi_0^2) \end{aligned}$$

where we have introduced

$$\Delta_0^0 = -\frac{\bar{\chi}_c}{i\bar{\omega}_c\bar{\gamma} + \bar{k}_s + \bar{\chi}_c} \int_0^1 \psi_0(s)ds$$

which can be solved for $\tau_0(s), \tau_2(s)$ using only knowledge of the linear solution ψ_0 , subject to the appropriate boundary conditions as defined in equations (E.3, E.6, E.9) of appendix E.

Matching $\mathcal{O}(\epsilon^3)$ terms gives rise to following relation

$$-\rho e^{i\theta} \partial_s^2 \psi_0 + i\mu \psi_0 + \mathcal{N}_1(\psi_0) + \mathcal{L}_c \psi_1 = 0 \quad (3.15)$$

where

$$\begin{aligned} \mathcal{N}_1(\psi_0) = & \bar{\chi}_{nl} \partial_s^2 [(\psi_0 + \Delta_0^0 - \psi_0(0)) |\psi_0 + \Delta_0^0 - \psi_0(0)|^2] + \partial_s (\tau_0 \dot{\psi}_0 + \tau_2 \dot{\psi}_0^*) \\ & + \beta \left[\partial_s (|\dot{\psi}_0|^2 \dot{\psi}_0) - 2\bar{\chi}_{lin}(\psi_0 + \Delta_0^0 - \psi_0(0)) |\dot{\psi}_0|^2 - \bar{\chi}_{lin}^*(\psi_0^* + \Delta_0^0 - \psi_0(0)^*) \dot{\psi}_0^2 + \dot{\tau}_0 \dot{\psi}_0 + \dot{\tau}_2 \dot{\psi}_0^* \right] \end{aligned}$$

Multiplying Eq. (3.15) with a conjugated linear mode ψ_0^+ and subsequent integration yields

$$\boxed{-\rho e^{i\theta} \int_0^1 \psi_0^+ \partial_s^2 \psi_0 ds + i\mu \int_0^1 \psi_0^+ \psi_0 + \int_0^1 \psi_0^+ \mathcal{N}_1(|\psi_0|^2 \psi_0) + Z = 0} \quad (3.16)$$

This equation captures the essence of how the non-linear solutions close to the bifurcation relate to the linearly unstable modes. The form of $Z = Z(\rho, \theta, \mu; \psi_0)$, and ψ_0^+ depend explicitly on the boundary conditions and are derived for the three different cases in appendix E. This complex equation relates the three real quantities ρ, θ and μ , enabling us, for example to determine the ρ and μ for a given value of θ , and hence the desired ϵ and ω for a given $\chi = \chi_c + \Delta\chi$ that satisfies $\arg(\Delta\chi) = \theta$. In the following we make use of it in order to determine the direction $\Delta\chi_{lin}$ in which the frequency of the solutions does not change. This relation then also allows us to determine how the amplitude ϵ grows as we go away from the bifurcation in the direction $\Delta\chi_{lin}$.

3.3. Numerical solutions

3.3.1. Mathematical structure and implementation

Equations (3.7) and (3.8) define a boundary value problem, which we solve by rewriting the three higher order complex equations as a system of fourteen real first order differential equations. Note that the problem is phase invariant, meaning that for the numerical procedure we arbitrarily fix the phase of the solution. We do so by imposing $\text{Im}\{\dot{\psi}(0)\} = -0.5\text{Re}\{\dot{\psi}(0)\}$. We proceed by using a “shoot and match” algorithm to solve the boundary problem. In the clamped head case without basal sliding that means determining seven parameters describing the unspecified boundary conditions at $s = 0$. To allow for basal sliding or a pivoting head, Δ_0 and $\psi(0)$ become additional parameters to be determined in a self-consistent fashion. Such a numerical “shoot and match” routine is very sensitive to initial guesses of the unknown parameters, which means that the algorithm does not converge for a random choice of initial values. To circumvent this problem we make use of the analytical expression for the amplitude of the solution in the close vicinity of the critical line

as discussed in the previous section. That is we take the linear solution with appropriate amplitude, $\epsilon\psi_0(s)$ to determine initial estimates for the unknown quantities. In the limit for $\epsilon \rightarrow 0$ our expansion becomes exact, meaning that as long as we are sufficiently close to the bifurcation point this method gives very good estimates for the initial guesses and the algorithm converges. We then use such a non-linear solution obtained in this way as a “seed” to find non-linear solutions further away from the critical line, by varying $\bar{\chi}_{lin}$ in small steps and estimating the unknown parameters with the help of the previously calculated solutions nearby.

3.3.2. Finite amplitude non-linear waves

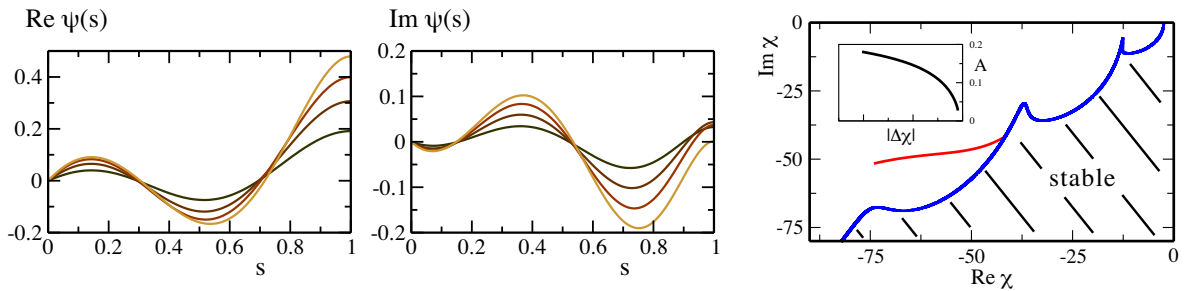


Figure 3.5: Illustrating how the 19Hz solution of the first branch of unstable modes grows as we go away from the bifurcation. On the left hand side numerical solutions to the non-linear equation are shown. As the real and imaginary parts of the shear angle $\psi(s)$ become lighter in colour the solution corresponds to points further away from the bifurcation. On the right hand side we show the amplitude of those solutions of equal frequency (inset) as well as the line in χ -space along which those iso-frequent solutions grow out of the critical line. Above results correspond to the clamped head boundary conditions without basal sliding. For the numerical calculations the ratio of friction coefficients $\xi_{\perp}, \xi_{\parallel}$ has been taken to be $\beta = 2$, as is a good approximation for a slender filament such as the axoneme.

In this section we present the resulting non-linear wave solutions for constant frequency as we go away from the bifurcation. The way we set up the problem is to treat χ_{nl} as a given constant, that we take arbitrarily of similar magnitude as χ_{lin} in the region of interest. In particular we set $\chi_{nl} = 42$ [124], as this ensures that the iso-frequent solutions that we discuss grow nicely into the unstable region in the frequency range of interest. In the real physical system both χ_{lin}, χ_{nl} depend in a non-trivial way on the frequency ω and control parameter Ω . In the physical system the frequency and bifurcation points are determined by the intersections of $\chi_{lin}(\omega, \Omega)$ with the critical lines. Hence our approach in this chapter discusses the properties of a selected few examples of any possible unstable modes. We follow this generic approach which has the advantage that the details of the motor response, which is captured in the functional dependence of $\chi_{lin}(\omega, \Omega)$ and $\chi_{nl}(\omega, \Omega)$, do not need to be specified.

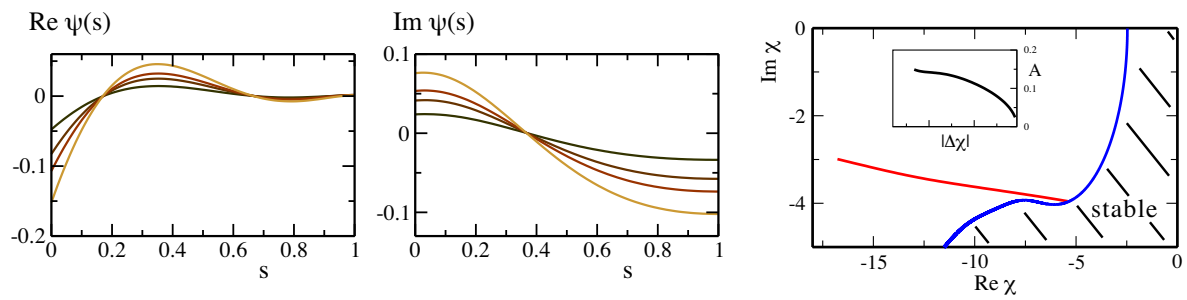


Figure 3.6: Same as Fig. 3.5, but now showing an example for the freely pivoting head boundary conditions, looking at the bifurcation corresponding to a frequency of approximately 3Hz.

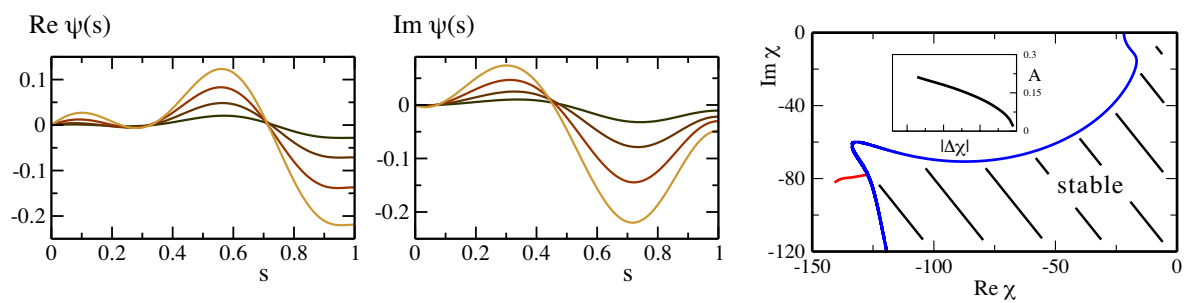


Figure 3.7: Same as Fig. 3.5, but now for the clamped head boundary conditions with basal sliding. Here we look at the bifurcation on the second branch of unstable modes corresponding to a frequency of approximately 18Hz. The mechanical properties of the basal connection were chosen such that the beat patterns resemble experimentally observed ones, as discussed in the following chapter.

Flagellar beats observed in vivo

4.1. Comparing linearly unstable modes to experimental beat patterns

In the previous part we showed that beats far away from the bifurcation are effectively described by linearly unstable modes right at the bifurcation multiplied with a finite amplitude. Hence in this chapter we look at those modes with which the system becomes unstable in greater detail and compare them with experimental data. The experimental results discussed in this section have been obtained by our collaborator Ingmar Riedel and were first presented in his dissertation [30]. These high precision data were extracted from videos (total recording time 4s) of defrosted bull sperm whose head was attached in a non-pivoting way to the cover slip, corresponding to the theoretical analysis of clamped head boundary conditions. The videos were recorded using a high speed camera (250 frames per second) and the flagellar shape was tracked automatically by an image analysis algorithm. In order to describe the very regular beat patterns quantitatively their zeroth and first Fourier mode were extracted. The resulting modes approximate the observed beat patterns very well [30], i.e. we have

$$\psi(s,t) \approx \tilde{\psi}^{(0)}(s) + \frac{1}{2}\tilde{\psi}^{(1)}(s)e^{i\omega t} + \text{c.c.}$$

Note that in previous studies a Fourier analysis has been used to extract the frequency of flagellar beats by (manually) following the time course of a pair of points along the flagellum [125]. The shape of the beating bull sperm has also been tracked with an automated digital image analysis previously [126], but the two approaches had not been combined to quantify the first Fourier mode of the flagellar beat before¹.

Calling for simplicity the linearly unstable solutions of the first Fourier mode ψ , (i.e. dropping the tilde, super- and subscripts) discussing the linearly unstable modes in the clamped

¹Which is somewhat surprising, since the spatial Fourier coefficients of snapshots of flagellar beats were already analysed in a study from a different technological age, in which the experimental set-up consisted of cine film, photosensitive detectors controlled by an analogue computer and punched paper tape recordings [127].

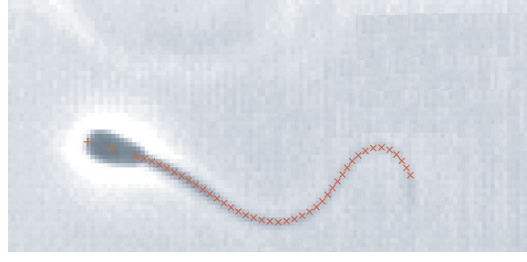


Figure 4.1: Typical snapshot of a beating bull sperm with an automatically tracked flagellum [30].

head case ($k_p \rightarrow \infty$) corresponds to solving

$$\boxed{i\bar{\omega}_c\psi + \overset{\cdot\cdot\cdot}{\psi} - \bar{\chi}_c\overset{\cdot\cdot}{\psi} = 0}$$

subject to the following boundary conditions

At $s = 0$	At $s = 1$
$\psi = 0$	$\overset{\cdot}{\psi} = 0$
$\overset{\cdot\cdot\cdot}{\psi} - \bar{\chi}_c\overset{\cdot\cdot}{\psi} = 0$	$\overset{\cdot\cdot}{\psi} - \bar{\chi}_c(\psi + \Delta_0) = 0$

where the basal sliding is given by

$$\Delta_0 = -\frac{\bar{\chi}_c}{i\bar{\omega}_c\bar{\gamma} + \bar{k}_s + \bar{\chi}_c} \int_0^1 \psi(s) ds \quad .$$

We discuss the theoretical solutions by using k_s and γ , which describe the previously undiscussed effective mechanical properties of the basal connection as fit parameters, in order obtain linearly unstable modes that reproduce quantitatively the high precision experimental data. Analysis of datasets from six different beating bull sperm (presented in appendix F) resulted in following dimensionless best fit parameters $\bar{k}_s = 129.1 \pm 4.1$ and $\bar{\gamma} = (131.0 \pm 2.6) \times 10^{-4}$ (mean \pm s.d.), which in physical dimensions are equivalent to

$$\begin{aligned} k_s &= (85.8 \pm 2.8) \frac{\text{pN}}{\text{nm}} \\ \gamma &= (0.286 \pm 0.006) \frac{\text{pNs}}{\text{nm}} \end{aligned}$$

where we have taken following values for $\xi_{\perp} = 10^{-3} \text{kg}(\text{ms})^{-1}$, $\kappa = 4 \times 10^{-22} \text{Nm}^2$, $a = 100 \text{nm}$, which are reasonable estimates for the perpendicular friction coefficient of the surrounding fluid used in the experiments [30] and the bending rigidity [106] as well as the radius of the axoneme. Note that from above datasets, values for the mechanical properties of the basal connection were estimated previously [30] by simple substitution of experimental curves for $\psi(s)$ into the theoretical equation. The results presented in this section are based on a different approach and were obtained by direct comparison of theoretical solutions to experimentally observed curves.

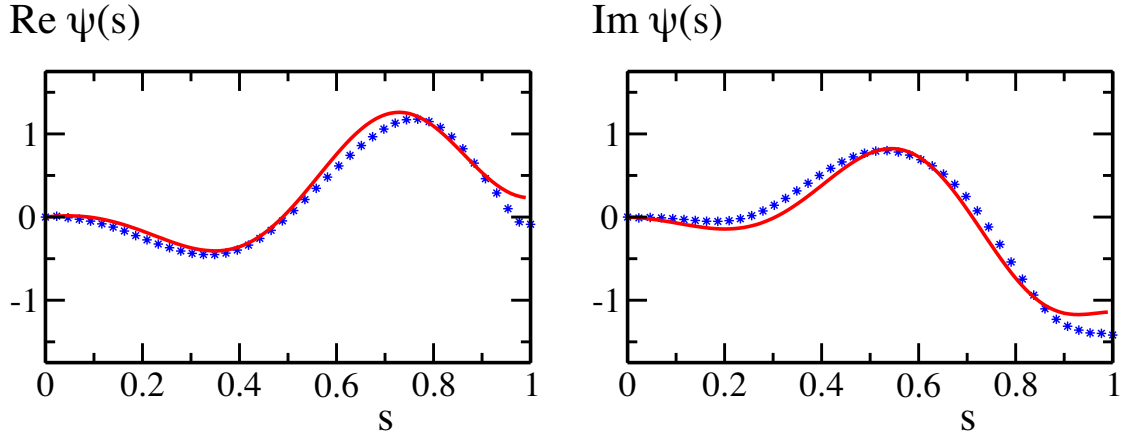


Figure 4.2: The theoretical result for the first Fourier mode of the shear angle ψ (red line) compared with the data (blue stars) from a particular bull sperm (S5) beating with $f \approx 20.28\text{Hz}$. The corresponding best fit values were $k_s = 84.8 \frac{\text{pN}}{\text{nm}}$, $\gamma = 0.283 \frac{\text{pNs}}{\text{nm}}$. The amplitude of the linear mode was fixed to match the experimental data. The corresponding graphs comparing theoretical solutions to the other experimental datasets, can be found in appendix F.

The corresponding amplitude of sliding oscillations at the base, can be determined from the absolute value of the first Fourier mode $|\Delta_0|$ as defined above in Eq. (4.1). In order to interpret the resulting value as the basal sliding of the three-dimensional axoneme, we recall that the $\Delta(s)$ used in the planar discussion corresponds to the angular Fourier component $\Delta_1(s)$ of the “three-dimensional” sliding $\Delta(s, \phi)$. Hence recalling Eq. (2.7) the relative sliding between two basal microtubule ends lying opposite of each other as indicated in Fig. 4.3 is given by

$$\Delta_A^B = \int_{-\frac{\pi}{2}}^{\frac{\pi}{2}} \Delta(s=0, \phi) d\phi = \Delta_1(0, \phi) \int_{-\frac{\pi}{2}}^{\frac{\pi}{2}} \cos(\phi) d\phi = 2\Delta_1(0) \equiv 2\Delta_0 \quad .$$

Hence the amplitude of basal sliding is given by $2|\Delta_0|$, which for the above best fit values of k_s and γ equates to $(360 \pm 38)\text{nm}$.

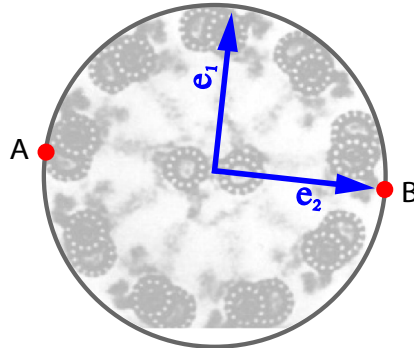


Figure 4.3: Relative sliding Δ_A^B between two basal points A and B corresponding to $R(0, \pm\frac{\pi}{2})$ on the axonemal surface. As discussed in the text $\Delta_A^B = 2\Delta_0$.

In the recent study in which the direct observation of basal sliding in chinchilla spermatozoa was reported, the amplitude of basal sliding was estimated to be of the order of 80nm. Whether larger basal sliding occurs in bull sperm flagella is not known, although a value of the order of 360nm, should be directly observable by electron microscopy (if the basal sliding could be stabilised). However, even if our theoretical value for basal sliding turns out to be too large, it is of the right order of magnitude giving us confidence that our theoretical values for k_s and γ will serve as a useful order of magnitude estimate for the mechanical properties of the basal connection.

Note that without allowing for a non-zero basal sliding Δ_0 it is not possible to achieve a qualitatively agreeing fit, implying that basal sliding has a significant effect on the beat pattern. Whether other effects such as an inhomogeneous structure of the axoneme along its length, could potentially play a similar role remains to be discussed in the future. But our results suggest the so far undiscussed possibility of beat pattern control via the mechanical properties of the basal connection, which we detail in the following section.

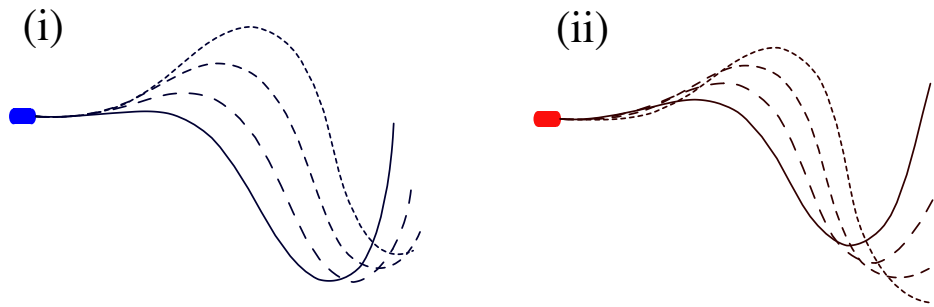


Figure 4.4: Direct comparison between (i) experimental beat pattern (blue head) and (ii) theoretical beat pattern (red head). The flagellar shape $\mathbf{r}(s)$ was reconstructed from the shear-angle $\psi(s)$ given in Fig. 4.2 as defined in Eq. (3.4). We show the first quarter of the beat cycle equally spaced in time.

4.2. Beat pattern control via the basal apparatus

Note that so far we have discussed the generic properties of the unstable Fourier modes at any hypothetical bifurcation point $\chi_c(\omega_c)$. Which of the modes becomes unstable is dependent on the microscopic details characterising the active and passive response of a given system. Furthermore our approach of looking at unstable Fourier modes does not allow us to conclude what happens when more than one mode is unstable. Mode co-existence, complicated interactions between the modes or the domination of one of the unstable modes could occur. However, in discussing a particular motor model we can still look at how the first unstable mode changes upon introduction of finite elasticity and friction at the head, enabling us to show as a “proof of principle” that beat patterns can be controlled by changing the elastic properties of the basal connection.

In order to relate our results to the physical behaviour of a given system, we discuss the microscopic origin of χ , because in a physical system χ is not a parameter but determined by mechanical and chemical properties of the motor system. All hypothetical motor models that lead to an oscillatory instability can be described close to the bifurcation by an effective

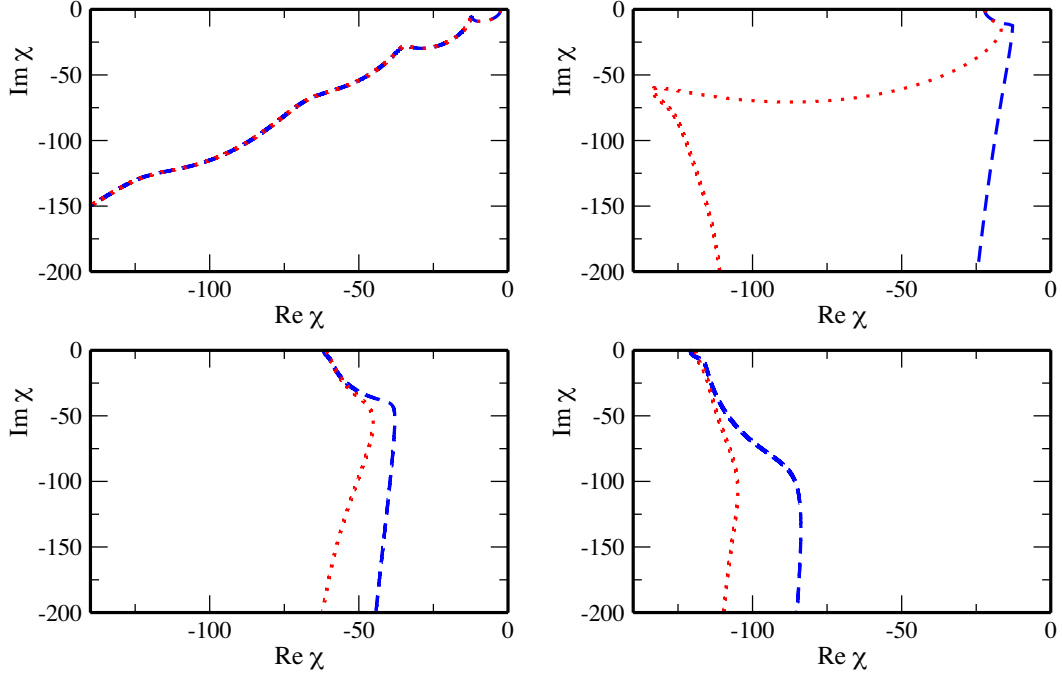


Figure 4.5: The critical lines taking the resulting best fit values for k_s, γ (blue lines) compared with the no-basal sliding case (red lines). Not plotted in the same diagram for readability. Notice the significant effect basal sliding has on the second branch of the critical points $\chi_c(\omega)$

response coefficient, but the exact nature of the dependence of χ on the frequency ω and control parameter Ω does depend on the assumed microscopic details. In order to illustrate the point that the mechanical properties of the basal connection can influence the possible beat patterns, we discuss the previously described two-state motor model that leads to the following response at frequency ω [106]

$$\chi(\omega, \Omega) = K + i\lambda\omega - \rho k\Omega \frac{i\frac{\omega}{\alpha} + (\frac{\omega}{\alpha})^2}{1 + (\frac{\omega}{\alpha})^2} \quad (4.1)$$

where K is the elastic modulus of a motor, λ the internal friction associated with a motor, ρ the density of motors on the axoneme, k the cross-bridge elasticity and α is a characteristic ATP turnover rate. Ω plays the role of a control parameter describing how far the system is driven away from equilibrium, with $0 < \Omega < \pi^2$. A given physical system with fixed parameters cannot exhibit bifurcations at arbitrary frequencies. The bifurcation points and frequencies are determined by the intersections of the above lines $\chi(\omega, \Omega)$ with the critical lines $\chi_c(\omega_c)$ with $\omega = \omega_c$. Since χ is complex but Ω is real, this means that the frequency with which it becomes unstable is intrinsically determined by the equation $\chi_c(\omega_c) = \chi(\omega_c, \Omega_c)$. In the case of the axoneme we have a discrete spectrum of critical lines $\chi_c(\omega_c)$ which means that there is more than just one bifurcation at which modes become unstable. The phase diagram specifying which mode becomes unstable with frequency ω and at which value of the control parameter Ω_c depends on the values of those parameters. For the motor model we have taken $K = 1.8 \times 10^4 \text{kgm}^{-1}\text{s}^{-2}$, $\lambda = 0.86 \text{kg}(\text{ms})^{-1}$, $\alpha = 6.6 \text{s}^{-1}$, $\rho = 5 \times 10^8 \text{m}^{-1}$, $k = 10^{-3} \text{Nm}^{-1}$. We discuss the unstable linear modes for these values of the parameters.

As the control parameter is increased under both conditions (no basal sliding, with basal sliding) the system will at some point become unstable. For $0.03743 < \Omega < 0.03745$ only the leading instability is unstable. The unstable modes for the two cases differ significantly as illustrated in Fig. 4.6. These modes do not correspond to commonly observed flagellar beat patterns, but they demonstrate directly that the mechanical properties of the basal connection can change the kind of beat pattern generated by an otherwise identical system. Our approach of looking at unstable Fourier modes does not allow us to determine the system's behaviour once several modes have become unstable. Different scenarios such as co-existence, mode-interaction or mode-dominance are possible. However, in order to indicate how significant the effect of basal sliding is as far as the linearly unstable modes are concerned, we compare in Fig. 4.6 the instability that occurred just before the range $0.03923 < \Omega < 0.04058$ in the two cases respectively. The system with basal sliding shows a nicely travelling wave solution as observed experimentally, whereas the system without basal sliding does not exhibit such behaviour. It is worth noting that the latter result is not due to our particular choice of parameters, but true in general, i.e. it is not possible to find solutions quantitatively reproducing experimental beat patterns as in the basal sliding case shown for example in Fig. 4.2. For completeness in appendix G we present the first six instabilities for the two different cases and detail at which values of Ω_c they become unstable with which critical frequencies.

So we conclude that beat patterns can indeed be regulated by changing the mechanical properties of the basal connection. From an evolutionary point of view this suggests that the different axonemal beat patterns that we see might be a result of different basal body structures [128]. But it also opens up the possibility that some of the observed changes of axonemal beat patterns due to an outside stimulus could be achieved by a change of the basal body structure on a short time scale, by proteins that interact (symmetrically and asymmetrically) with the basal body, as reported in [129,130].

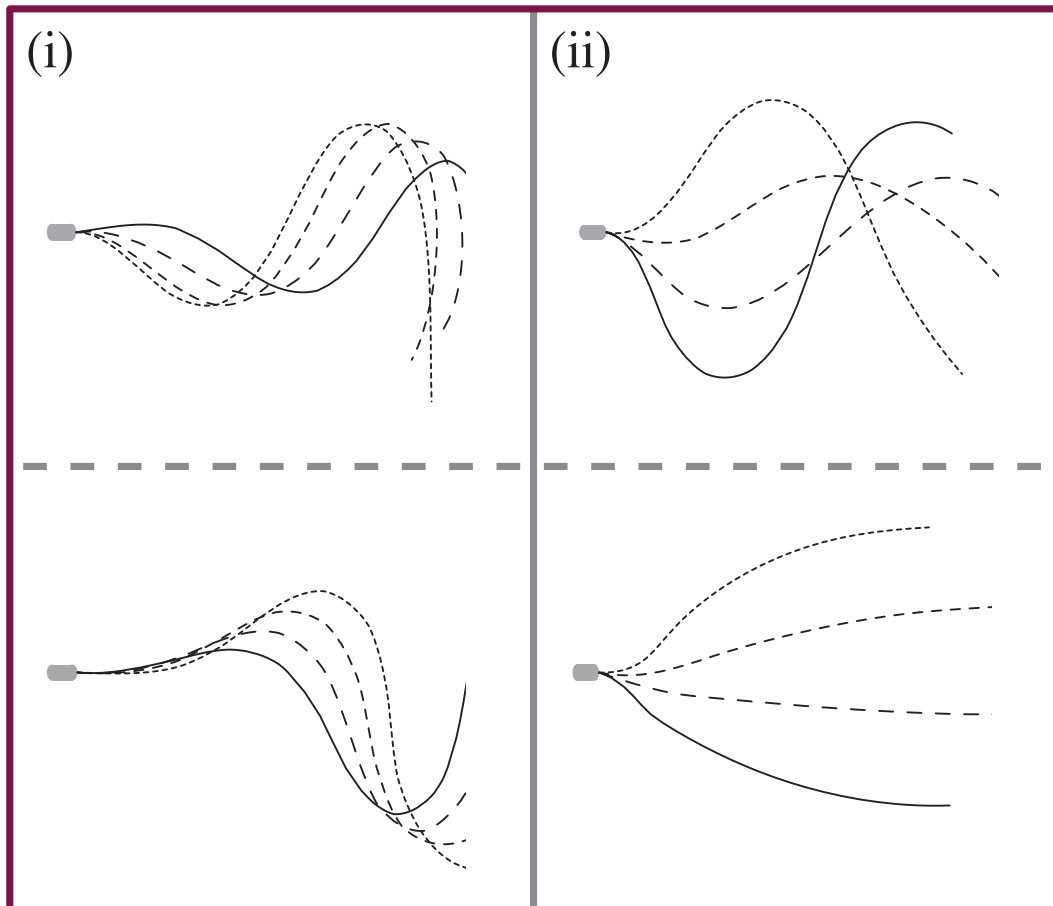


Figure 4.6: The first and fourth linearly unstable modes. Comparison between (i) basal sliding and (ii) no basal sliding beat patterns. In the first case the basal connection is characterised by a finite elasticity of $k_s = 85.8 \frac{\mu N}{nm}$ and a friction $\gamma = 0.286 \frac{\mu N s}{nm}$. For the choice of parameters describing the motors as specified in the text, above first modes (upper part) are unstable in the range of $0.03743 < \Omega < 0.03745$. The respective frequencies are (i) 28Hz and (ii) 14Hz. In the range $0.03923 < \Omega < 0.04058$ above fourth modes (lower part) are unstable with respective frequencies of (i) 20Hz and (ii) 5Hz. Shown here are snapshots of the flagellar shape during a quarter of the beat cycle.

Three dimensional beat patterns

5.1. Equilibrium configuration and linearly unstable modes

The full description of non-linear dynamics of the axoneme in three dimensions is given by equations (2.16)-(2.18). In this chapter we first determine the equilibrium configuration for an axoneme in which all motors exhibit a constant background activity, and then linearise around this equilibrium state to determine the modes with which the system becomes unstable. Similar to the preceding chapter this will prove instructive in discussing the kind of beat patterns the system will exhibit.

Assuming there is a time-independent contribution to the activity of the motors, we write

$$f_0(s, t) = f_0^c(s) + f_0^t(s, t)$$

implying that there is a constantly active motor force $f_0^c(s)$ acting along the axoneme, which we expect to lead to a non-zero equilibrium twist. Hence we also split the twist angle Ω_3 into a stationary and a time-dependent part

$$\Omega_3(s, t) = \Omega_3^c(s) + \Omega_3^t(s, t)$$

where $\Omega_3^c(s)$ is determined by $f_0^c(s)$ as shown below.

Substitution of above expression into the differential equation for the twist angle Eq. (2.18) yields to linear order

$$-\xi_r \partial_t \Omega_3^t = 2\pi a^2 (\ddot{f}_0^c(s) + \ddot{f}_0^t(s, t)) - \kappa_3 (\ddot{\Omega}_3^c(s) + \ddot{\Omega}_3^t(s, t)) \quad .$$

Matching the time independent terms leads to

$$\kappa_3 \ddot{\Omega}_3^c(s) = 2\pi a^2 \ddot{f}_0^c(s)$$

with the following linear order boundary conditions

$$\dot{\Omega}_3^c(0) = 0 \quad \Omega_3^c(L) = \frac{2\pi a^2}{\kappa_3} f_0^c$$

$$\Rightarrow \Omega_3^c(s) = \frac{2\pi a^2}{\kappa_3} f_0^c(L) - \int_s^L \int_0^{s'} \ddot{f}_0^c(s') ds' .$$

For the sake of simplicity assuming that the time-independent part of the force is homogeneous along the axoneme, i.e.

$$\begin{aligned} f_0^c(s) &= \text{const} \\ \Rightarrow \ddot{f}_0^c &= 0 \end{aligned}$$

and hence

$$\begin{aligned} \Omega_3^c(s) &= \frac{2\pi a^2}{\kappa_3} f_0^c \\ &\equiv A . \end{aligned}$$

Meaning that the equilibrium configuration is given by

$$\begin{aligned} \Omega_1(s) &= 0 \\ \Omega_2(s) &= 0 \\ \Omega_3(s) &= A \end{aligned}$$

which defines a straight rod with a constant twist.

We linearise around this state by taking $(\Omega_1(s), \Omega_2(s), \Omega_3^t(s)) = (\bar{\Omega}_1(s), \bar{\Omega}_2(s), A + \bar{\Omega}_3^t(s))$. Assuming that A is small (i.e. neglecting $\mathcal{O}(A^2)$ terms), we arrive at the equations of motion for the solutions of infinitesimally small amplitude, for which terms of order $\mathcal{O}(\Omega^2)$ become negligible

$$\begin{aligned} \xi_{\perp} \partial_t \Omega_1 &= -\kappa_1 \ddot{\bar{\Omega}}_1 + a\pi \ddot{f}_1 + 4A(\kappa_2 \ddot{\bar{\Omega}}_2 - a\pi \ddot{f}_2) \\ \xi_{\perp} \partial_t \Omega_2 &= -\kappa_2 \ddot{\bar{\Omega}}_2 + a\pi \ddot{f}_2 - 4A(\kappa_1 \ddot{\bar{\Omega}}_1 - a\pi \ddot{f}_1) \\ \xi_r \partial_t \Omega_3^t &= \kappa_3 \ddot{\bar{\Omega}}_3^t - 2a^2 \pi \ddot{f}_0^t \\ \dot{\tau} &= 0 \end{aligned} \tag{5.1}$$

where we immediately dropped the overbars for notational convenience. Together with the following linearised boundary conditions these equations define the linear modes in the limit of small amplitudes.

At $s = 0$	At $s = L$
$\kappa_1 \ddot{\bar{\Omega}}_1 = a\pi \dot{f}_1 + 2A(\kappa_2 \dot{\bar{\Omega}}_2 - a\pi f_2)$	$\Omega_1 = 0$
$\kappa_1 \ddot{\bar{\Omega}}_2 = a\pi \dot{f}_2 - 2A(\kappa_1 \dot{\bar{\Omega}}_1 - a\pi f_1)$	$\Omega_2 = 0$
$\kappa_1 \ddot{\bar{\Omega}}_1 = a\pi \dot{f}_1 + 3A(\kappa_2 \ddot{\bar{\Omega}}_2 - a\pi \dot{f}_2)$	$\dot{\Omega}_1 = \frac{a\pi f_1}{\kappa_1}$
$\kappa_1 \ddot{\bar{\Omega}}_2 = a\pi \dot{f}_2 - 3A(\kappa_1 \dot{\bar{\Omega}}_1 - a\pi f_1)$	$\dot{\Omega}_2 = \frac{a\pi f_2}{\kappa_2}$
$\dot{\Omega}_3^t = 0$	$\Omega_3^t = \frac{2\pi a^2}{\kappa_3} f_0^t$
$\dot{\tau} = 0$	$\tau = 0$

(5.2)

In order to study oscillatory solutions to the above equations of motion, we analyse the equations describing the Fourier modes of the time-dependent quantities.

Frequency representation

Similarly to the previous discussion of planar beats we make the following Fourier mode ansatz

$$\begin{aligned} f(s, \phi; t) &= \sum_n \tilde{f}^{(n)}(s, \phi) e^{in\omega t} \\ \Delta(s, \phi; t) &= \sum_n \tilde{\Delta}^{(n)}(s, \phi) e^{in\omega t} \\ \Omega_i(s, \phi; t) &= \sum_n \tilde{\Omega}_i^{(n)}(s, \phi) e^{in\omega t} \end{aligned}$$

and assume the following relation between the first time like Fourier modes, as previously derived for a system of many motors [101]

$$\tilde{f}^{(1)}(s, \phi) = \chi \tilde{\Delta}^{(1)}(s, \phi) + \text{h.o.t.} \quad , \quad (5.3)$$

which for the first Fourier modes of the angular components gives us

$$\begin{aligned} \tilde{f}_0^{(1)}(s) &= \chi \tilde{\Delta}_0^{(1)}(s) = -a^2 \chi \tilde{\Omega}_3^{t,(1)}(s) \\ \tilde{f}_1^{(1)}(s) &= \chi \tilde{\Delta}_1^{(1)}(s) = a\chi \int_0^s \tilde{\Omega}_1^{(1)}(s') ds' \\ \tilde{f}_2^{(1)}(s) &= \chi \tilde{\Delta}_2^{(1)}(s) = a\chi \int_0^s \tilde{\Omega}_2^{(1)}(s') ds' \quad . \end{aligned}$$

This leads to the following set of coupled ordinary differential equations describing the modes with which the system becomes linearly unstable (dropping the tilde and superscript denoting the Fourier modes so as not to overburden the notation)

$$\begin{aligned} i\omega \xi_{\perp} \Omega_1 &= -\kappa_1 \ddot{\Omega}_1 + a^2 \pi \chi \ddot{\Omega}_1 + 4A(\kappa_2 \ddot{\Omega}_2 - a^2 \pi \chi \dot{\Omega}_2) \\ i\omega \xi_{\perp} \Omega_2 &= -\kappa_2 \ddot{\Omega}_2 + a^2 \pi \chi \ddot{\Omega}_2 - 4A(\kappa_1 \ddot{\Omega}_1 - a^2 \pi \chi \dot{\Omega}_1) \\ i\omega \xi_r \Omega_3^t &= (\kappa_3 + 2a^4 \pi \chi) \ddot{\Omega}_3^t \\ \ddot{\tau} &= 0 \end{aligned} \quad (5.4)$$

subject to boundary conditions

$$\begin{array}{c|c} \underline{\text{At } s=0} & \underline{\text{At } s=L} \\ \hline \kappa_1 \ddot{\Omega}_1 = a^2 \pi \chi \Omega_1 + 2A\kappa_2 \Omega_1' & \Omega_1 = 0 \\ \kappa_1 \ddot{\Omega}_2 = a^2 \pi \chi \Omega_2 - 2A\kappa_1 \Omega_2' & \Omega_2 = 0 \\ \kappa_1 \ddot{\Omega}_1 = a^2 \pi \chi \dot{\Omega}_1 + 3A(\kappa_2 \ddot{\Omega}_2 - a^2 \pi \chi \Omega_2) & \dot{\Omega}_1 = \frac{a^2 \pi \chi}{\kappa_1} \int_0^L \Omega_1(s') ds' \\ \kappa_1 \ddot{\Omega}_2 = a^2 \pi \chi \dot{\Omega}_2 - 3A(\kappa_1 \Omega_1'' - a^2 \pi \chi \Omega_1) & \dot{\Omega}_2 = \frac{a^2 \pi \chi}{\kappa_1} \int_0^L \Omega_2(s') ds' \\ \dot{\Omega}_3^t = 0 & \Omega_3^t (1 + \frac{2a^4 \pi}{\kappa_3} \chi) = 0 \\ \dot{\tau} = 0 & \tau = 0 \end{array} \quad (5.5)$$

5.2. Beating patterns for symmetric bending rigidities

Motivated by the important dynamics of the nodal cilia, that have a 9+0 axoneme, we discuss the case of symmetric bending rigidities, i.e. $\kappa_1 = \kappa_2 \equiv \kappa$. For notational convenience we introduce the vectorial quantity

$$\mathbf{z} = \begin{pmatrix} \Omega_1 \\ \Omega_2 \end{pmatrix} \quad (5.6)$$

We rewrite the differential equations and boundary conditions in Ω_1, Ω_2 of equations (5.4) and (5.5) using Eq. (5.6). After rescaling $s \rightarrow \frac{s}{L}$, $AL \rightarrow A$ and introducing the dimensionless quantities $\bar{\omega} = \frac{\omega L^4}{\kappa} \xi_{\perp}$, $\bar{\chi} = \frac{\pi a^2 L^2}{\kappa} \chi$ we obtain

$$\boxed{i\bar{\omega}\mathbf{z} = -\ddot{\mathbf{z}} + \bar{\chi}\dot{\mathbf{z}} + 4AM(\ddot{\mathbf{z}} - \bar{\chi}\dot{\mathbf{z}})} \quad (5.7)$$

At $s = 0$	At $s = L$
$-\ddot{\mathbf{z}} + \bar{\chi}\dot{\mathbf{z}} + 2AM\dot{\mathbf{z}} = 0$	$\mathbf{z} = 0$
$-\ddot{\mathbf{z}} + \bar{\chi}\dot{\mathbf{z}} + 3AM(\ddot{\mathbf{z}} - \bar{\chi}\dot{\mathbf{z}}) = 0$	$-\dot{\mathbf{z}} + \bar{\chi} \int_0^L \mathbf{z}(s) ds + AM\mathbf{z} = 0$

(5.8)

where the coupling matrix is given by

$$\mathbf{M} = \begin{pmatrix} 0 & 1 \\ -1 & 0 \end{pmatrix} .$$

We find the solutions to the above problem by making an exponential ansatz

$$\mathbf{z}(s) = \mathbf{z}_0 e^{qs}$$

which leads us to the following equation

$$i\bar{\omega}\mathbf{z}_0 = -q^4\mathbf{z}_0 + q^2\bar{\chi}\mathbf{z}_0 + 4AM(q^3\mathbf{z}_0 - q\bar{\chi}\mathbf{z}_0) .$$

Let \mathbf{z}_0 be an eigenvector of \mathbf{M} with eigenvalue λ , i.e. $\mathbf{M}\mathbf{z}_0 = \lambda\mathbf{z}_0$, then q satisfies the following fourth order polynomial equation

$$q^4 - q^2\bar{\chi} - 4A\lambda(q^3 - q\bar{\chi}) + i\bar{\omega} = 0 .$$

Let q_n be solutions to the above equation for $\lambda = i$ then the general solution to the differential equation is given by

$$\boxed{\mathbf{z}(s) = \sum_{n=1}^{n=4} C_n \mathbf{z}_1 e^{q_n s} + D_n \mathbf{z}_2 e^{-q_n s}} \quad (5.9)$$

where $\mathbf{z}_1, \mathbf{z}_2$ are the eigenvectors of \mathbf{M} with eigenvalues $\lambda_1 = i, \lambda_2 = -i$ given by

$$\mathbf{z}_1 = \begin{pmatrix} 1 \\ i \end{pmatrix}, \mathbf{z}_2 = \begin{pmatrix} 1 \\ -i \end{pmatrix}$$

The eight unknown complex constants C_n, D_n of the general solution are determined by the boundary conditions. Substituting Eq. (5.9) into Eq. (5.8) and introducing the vectors $\mathbf{c} = (C_1, C_2, C_3, C_4)$ and $\mathbf{d} = (D_1, D_2, D_3, D_4)$ leads to the following matrix equation

$$\mathbf{Q}^{(1)}(\bar{\chi}, \bar{\omega})\mathbf{c} = 0 \quad \mathbf{Q}^{(2)}(\bar{\chi}, \bar{\omega})\mathbf{d} = 0$$

where the matrices $\mathbf{Q}^{(1)}, \mathbf{Q}^{(2)}$ depend on $\bar{\chi}$ and $\bar{\omega}$ as defined in appendix H. The necessary condition for non-zero solutions to exist, namely $\det \mathbf{Q}^{(1)} = 0$ or $\det \mathbf{Q}^{(2)} = 0$ leads to a discrete spectrum of $\bar{\chi}$ for which the system has non-zero solutions for a given value of $\bar{\omega}$. This can be visualised as critical branches of $\bar{\chi}_c(\bar{\omega}_c)$ in the complex plane for a whole range of critical frequencies $\bar{\omega}_c$ as illustrated in Fig. 5.1. For the numerical calculations we have taken the symmetry breaking term to be of value $A = 0.01$, which for a reasonable estimate of twist rigidity corresponds to a small background motor activity¹.

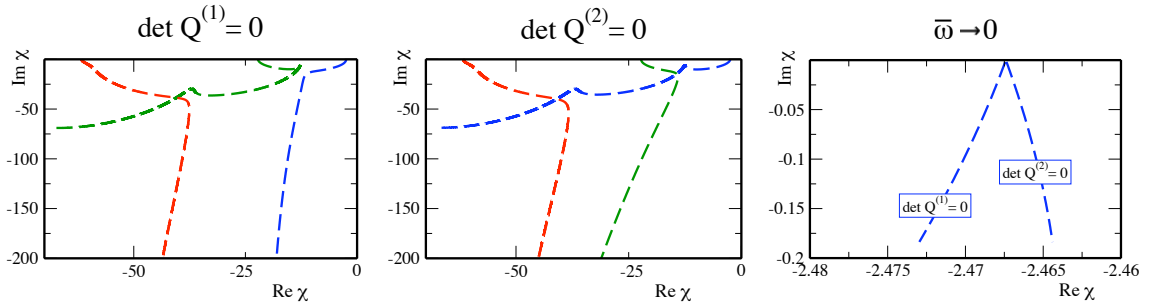


Figure 5.1: Critical values $\bar{\chi}_n(\bar{\omega})$ for which the two matrices describing clamped head boundary conditions become singular. The small symmetry braking pre-twist has been taken as $A = 0.01$ and the lines start for $\bar{\omega} = 0$ on the real axis where $\bar{\chi}_n = -(\frac{2n+1}{2}\pi)^2$. See appendix H for detailed derivation. The dashed lines on the left correspond to $\det \mathbf{Q}^{(1)} = 0$ and the ones in the middle correspond to $\det \mathbf{Q}^{(2)} = 0$. The right hand side shows a detailed view of the first branch of critical lines for small values of $\bar{\omega}$. The left branch corresponds to solutions that twirl in a clockwise fashion whereas the right branch corresponds to solutions that twirl in a counterclockwise fashion.

Similarly to above discussion of $\bar{\chi}_c(\bar{\omega}_c)$ that leads to non-zero solutions in $\Omega_1(s), \Omega_2(s)$, there exist values for which $\Omega_3^t(s)$ exhibits non-zero solutions, corresponding to twist oscillations. However, motivated by the observed bending modes of nodal cilia we concentrate on the instabilities for which $\Omega_3^t = 0$. Examples of theoretical bending modes of appropriate frequency on the first branch of instabilities are illustrated in Figs. 5.2 and 5.3. Note that they are twirling solutions that reproduce qualitatively the experimentally observed vortical beat patterns of nodal cilia [3].

Note that our way of characterising the unstable modes of the system is independent of the microscopic details. These modes are generic in so far as that any motor model that leads to a response function like Eq. (5.3) will lead to such a set of unstable solutions on the critical lines $\bar{\chi}_c(\omega_c)$. But this also means that in order to interpret such a χ -diagram we

¹With ten inner and four outer dynein arms per 96nm repeat along the nine microtubule doublets [131], a maximum force generated per motor estimated to be 6pN [78] and a twist rigidity $\kappa_3 \approx 2.2\kappa_1 \approx 9 \times 10^{-22}\text{Nm}^2$ [98] such a small pre-twist of $A = 0.01$ over the length of a $3\mu\text{m}$ long cilium corresponds to approximately 5% of the maximum twist that could be generated by the motors.

need to discuss a particular motor model explicitly describing the dependence of χ on the frequency and control parameter similarly to the discussion in section 4.2.

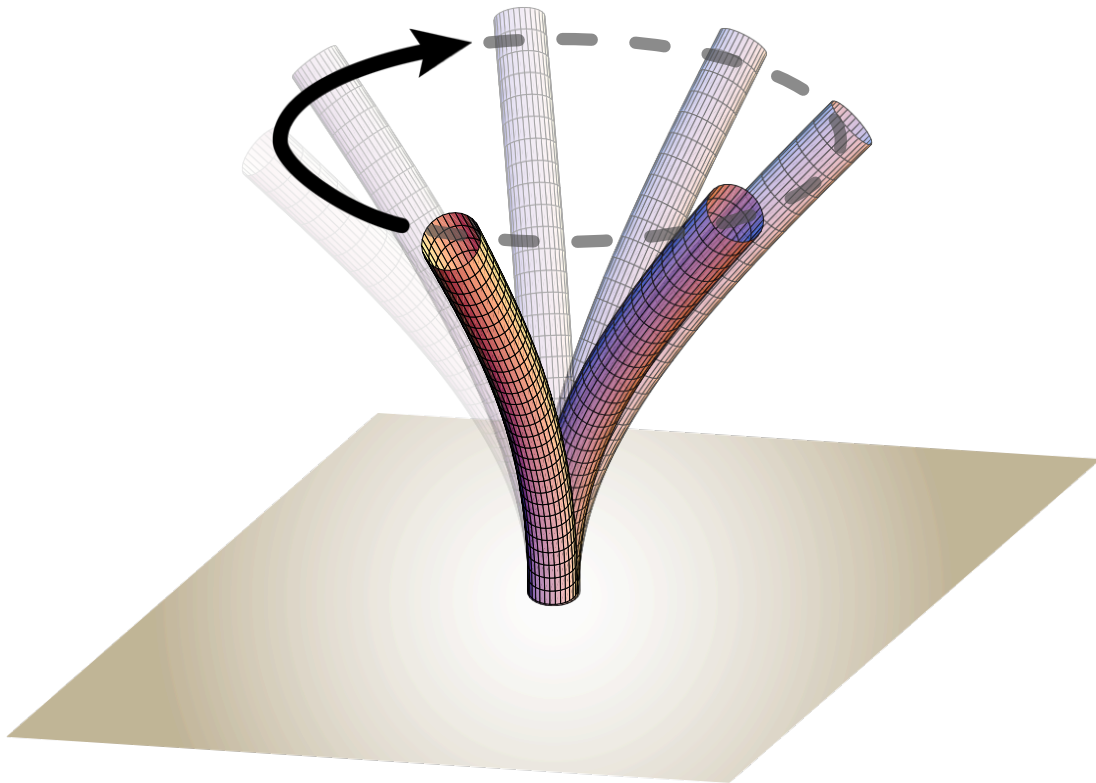


Figure 5.2: Three dimensional shape of a “twirling” solution for a symmetric cilium of length $L \approx 3\mu m$ beating with $f \approx 10Hz$, corresponding to unstable modes on the first branch of $\det \mathbf{Q}^{(1)} = 0$ (clockwise rotation) for $A = 0.01$. In order to obtain these graphical solutions of the axoneme in cartesian co-ordinates we numerically integrated the system of coupled ODEs given by Eq. (2.2) to reconstruct $\mathbf{r}(s)$ from $\tilde{\Omega}_1(s), \tilde{\Omega}_2(s), \tilde{\Omega}_3(s)$.

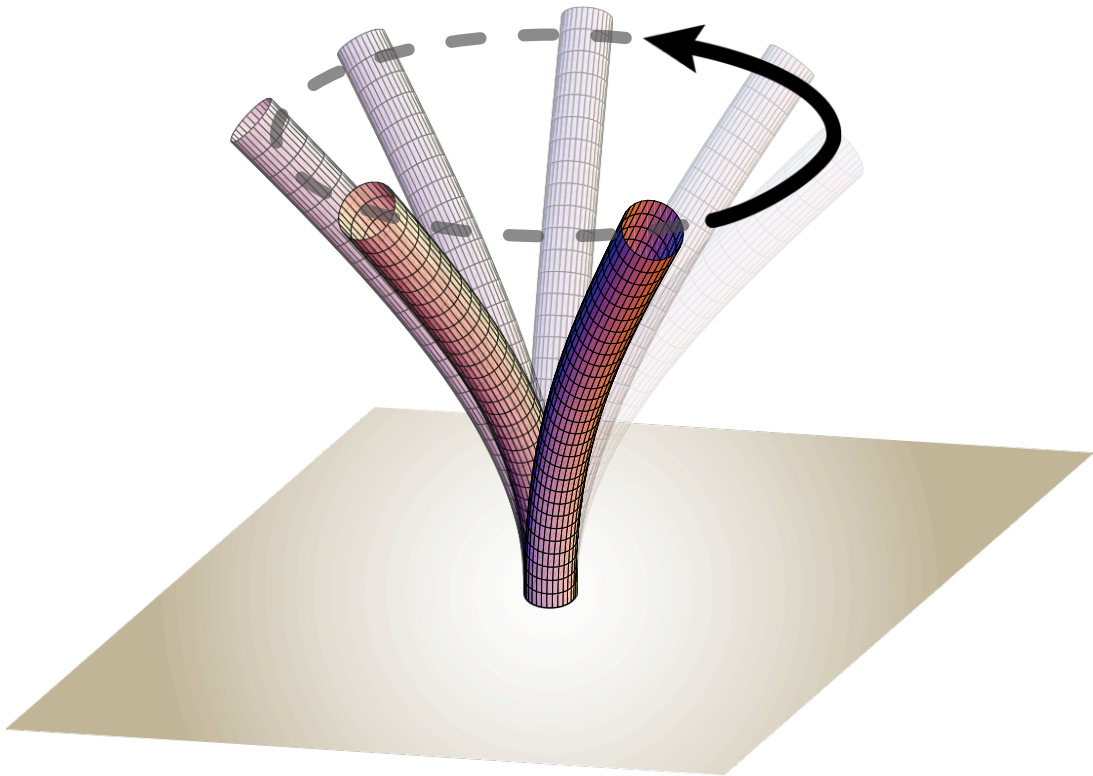


Figure 5.3: Three dimensional shape of a “twirling” solution for a symmetric cilium of length $L \approx 3\mu m$ beating with $f \approx 10Hz$, corresponding to unstable modes on the first branch of $\det \mathbf{Q}^{(2)} = 0$ (counter-clockwise rotation) for $A = 0.01$. In order to obtain these graphical solutions of the axoneme in cartesian co-ordinates we numerically integrated the system of coupled ODEs given by Eq. (2.2) to reconstruct $\mathbf{r}(s, t)$ from $\tilde{\Omega}_1(s), \tilde{\Omega}_2(s), \tilde{\Omega}_3(s)$.

Conclusions and discussion

The motility of cilia and flagella lies at the heart of many different biological processes discussed in fields ranging as varied as developmental biology, the swimming of microorganisms, and otolaryngological¹ medicine. Over the past four decades much progress has been made in elucidating the microscopic structure of the axoneme that forms the active core of cilia and flagella. However, progress on finding a control mechanism that explains the orchestrated activity of the the force generating molecular motors, in all these different circumstances, has remained unsatisfactorily vague. No simple answer has emerged, because there is no explanation of the simple kind people were looking for. The dynamics of cilia and flagella cannot be understood by cataloguing parts and drawing schematic interaction diagrams, for two reasons. Firstly, a system consisting of thousands of interacting force generators exhibits collective properties that cannot be explored by means of qualitative reasoning, but can only be uncovered by a rigorous mathematical analysis. Secondly, ciliary and flagellar beat patterns are a fundamentally dynamic effect, which means that studying this problem requires an understanding of the physical forces that govern this dynamics. Those physical forces can be understood within the theoretical framework described in this thesis. As a result of our work a picture emerges, that offers a unifying viewpoint on the dynamics of flagella, primary cilia and “conventional” cilia – to follow the traditional, somewhat arbitrary classification of axonemal structures.

We showed that the axonemal structure is fundamentally capable of generating many different oscillatory beat patterns, and provide evidence that subtle influences such as the boundary conditions lead to a selection and modulation of these beat patterns. We hope that these insights, as summarised below, contribute to the understanding of the fascinating dynamics of cilia and flagella.

¹Ear, Nose, Throat.

6.1. Summary of our results

- We analysed the low Reynolds number² dynamics of a cylindrical structure that actively changes its shape. This analysis applies to cilia and flagella in which the axoneme drives the motility due internally generated forces. The equations derived in chapter two allow for the discussion of a general force distribution along the axoneme and provide a powerful theoretical framework that describes the dynamics of cilia and flagella for any hypothesised form of time-dependent motor activity.
- Following the previously formulated idea of spontaneous oscillations of a system of many molecular motors described by a Hopf bifurcation [101,106], we examined the two-dimensional limit of our theoretical description. Explicitly discussing the mechanical properties of the basal connection of the axoneme we show that a non-linear “wave equation” leads to oscillatory solutions that resemble experimentally observed flagellar beat patterns and determine the amplitude of those solutions analytically close to the instability.
- We noticed that the non-linear, finite-amplitude waves are similar to the linear modes with which the system becomes unstable right at the bifurcation. By comparing linear modes to previously presented quantitative data [30] from beating bull sperm, we estimate the effective elasticity and friction of the basal connection to be $k_s = (85.8 \pm 2.8) \frac{\text{pN}}{\text{nm}}$ and $\gamma = (0.286 \pm 0.006) \frac{\text{pNs}}{\text{nm}}$ respectively, leading to non-zero basal sliding as directly supported by experimental observation [28].
- We showed that planar beat patterns can be altered significantly by changing the mechanical properties of the basal connection and thereby with this “proof of principle” propose a way of beat pattern control via the basal apparatus.
- Finally, we examined the three dimensional equations by discussing linearly unstable modes in the case of symmetric bending rigidities. We showed that an un-regulated 9+0 axoneme is capable of generating oscillatory solutions resembling the observed vortical beat patterns of nodal cilia, that play a crucial role in determining the left-right axis during embryological development.

We conclude that that due to the collective properties of a system of many molecular motors, commonly observed beat patterns of cilia and flagella can be achieved by the axonemal structure in the absence of any biochemical regulation. Although this does not imply that biochemical regulations are irrelevant, our result that the unregulated axoneme can oscillate spontaneously, naturally leads to the assumption that self-organisation is the fundamental principle by which basic beat patterns are generated.

²That is where viscous forces dominate, meaning that inertial effects can be neglected as is the case for axonemal dynamics.

6.2. Outlook on future work

6.2.1. Generic properties vs microscopic details of physical systems

The presented derivation of the equations defining the time-evolution of the axonemal configuration, and our analysis of these time-dependent equations in terms of oscillatory solutions elucidate the system's generic properties. As discussed in section 4.2 the microscopic details of a given motor model determine which of the modes will become unstable, and with which frequency at which value of the control parameter the instability occurs. However, once more than one such mode is unstable our approach does not allow us to deduce the system's behaviour. Different scenarios such as mode domination, mode co-existence or more complicated mode interactions are possible. In order to determine what happens under given circumstances it is necessary to study the time-dependent problem directly, either by numerical integration of the partial differential equations, or – which could be preferable for stability reasons – by introducing a discrete formulation of the axonemal structure.

In order to make a general point about finite amplitude oscillations and how they relate to linearly unstable modes, we took a constant value for the non-linear response coefficient χ_{nl} . It will be instructive to explicitly take the dependence of the non-linear response coefficient on the beat frequency and the control parameter into account. This would complement our theory so that it could describe the system's behaviour as a function of the order parameter such as the ATP concentration for a given set of microscopic and macroscopic parameters.

6.2.2. Discussing asymmetry - on which side lies your heart?

The fact that among vertebrate species as different as mice, zebrafish, rabbits and in all likelihood us humans, it is a fluid flow generated by the rotation of cilia that is responsible for breaking the left-right symmetry of the embryo, is a fascinating discovery that has received an immense amount of recent attention [2,3,8,25,54,55,132–135]. We showed that cilia are capable of generating such vortical motion, but also that the axonemal structure fundamentally leads to rotations in both clockwise and counterclockwise directions. In nature both circling patterns are observed, however in the case of nodal cilia it seems crucial that the cilia all rotate in the same direction³ to produce a fluid flow to the left of the body axis⁴. This raises the intriguing question – that has not featured as prominently in the existing literature as it deserves – namely, how it is achieved that the cilia rotate in this and not in the other direction when required? This is an aspect of the fundamental question of how the axoneme can generate the appropriate beat pattern in a given environment.

Addressing this question is fundamental to the understanding of cilia and flagella, since it is their versatility that lies at the heart of their importance, as highlighted by the fact that ongoing research continues to discover an ever increasing number of systems where the beating of cilia and flagella is crucial [56]⁵.

Based on the results of our work we put forward the hypothesis that the mechanical properties of the basal body are important in selecting and modulating basal beat patterns. The

³Clockwise when viewed from the tip, in the case for mouse embryos.

⁴As a result of a posteriorly tilted axis of the cilia.

⁵And thereby overthrows “conventional wisdom” regarding primary cilia that have long been thought to be immotile.

experimental observation that *The diversity of structural organization of the basal apparatus between animals is considerable* [128] characterises this hypothesis as a logical candidate to explain the versatility of cilia and flagella. It is intriguing that even in the first report of rotating primary cilia [52] it was stressed that their basal bodies differ significantly from the ones of “normal” epithelial cilia (whose power stroke lies in a plane defined by their basal foot [136]). The analysis presented in this thesis, twenty years after that observation, lends itself to address the effect of different basal body structures on ciliary beat patterns.

Hence, it is with great excitement that we look forward to exploring the effects of asymmetric boundary conditions representing the basal connection on an otherwise symmetric 9+0 axoneme. This, as well as other aspects such as asymmetric bending rigidities, representing the central pair of the 9+2 structure, or the effect of Ca^{2+} on the overall activity of the motors, should be at the centre of future research that will shed more light on the dynamics of cilia and flagella in a wide range of different systems, and maybe answer questions such as why it is that your heart lies on the left side.

A

Local sliding expression

In this appendix we derive an expression for the local sliding displacement $\Delta(s, \phi)$ in terms of the geometrical quantities $\Omega_i(s)$ that define the configuration of the axoneme in three-dimensions.

We are interested in the derivative of $L(s, \phi)$ in the direction of $\mathbf{n}(s, \phi)$ as discussed in section 2.2.1. In the (non-orthogonal) co-ordinate system with unit vectors

$$\mathbf{e}_s = \frac{\mathbf{R}_s}{|\mathbf{R}_s|}, \mathbf{e}_\phi = \frac{\mathbf{R}_\phi}{|\mathbf{R}_\phi|} \quad ,$$

we have

$$\mathbf{n} = n_s \mathbf{e}_s + n_\phi \mathbf{e}_\phi \quad .$$

Orthogonality of $\mathbf{n}(s, \phi)$ to $\mathbf{R}_s(s, \phi)$ yields

$$n_s = -n_\phi \mathbf{e}_s \cdot \mathbf{e}_\phi$$

and normality of \mathbf{n} implies

$$n_s^2 + n_\phi^2 + 2n_s n_\phi \mathbf{e}_s \cdot \mathbf{e}_\phi = 1$$

which we can solve for n_s, n_ϕ (choosing the sign appropriately, as discussed in section 2.2.1)

$$\begin{aligned} n_s &= -\frac{\mathbf{e}_s \cdot \mathbf{e}_\phi}{\sqrt{1 - (\mathbf{e}_s \cdot \mathbf{e}_\phi)^2}} \\ n_\phi &= \frac{1}{\sqrt{1 - (\mathbf{e}_s \cdot \mathbf{e}_\phi)^2}} \quad . \end{aligned}$$

The arclength of a microtubule at point $\mathbf{R}(s, \phi)$ is given by $L(s, \phi) = \int_0^s ds' |\mathbf{R}_s(s', \phi)|$

such that the partial derivatives read

$$\begin{aligned}\partial_s L &= \sqrt{\mathbf{R}_s(s, \phi) \cdot \mathbf{R}_s(s, \phi)} \\ \partial_\phi L &= \int_0^s ds' \partial_\phi \sqrt{\mathbf{R}_{s'}(s', \phi) \cdot \mathbf{R}_{s'}(s', \phi)} \\ &= \int_0^s ds' \frac{\mathbf{R}_{s'}(s', \phi) \cdot \mathbf{R}_{s', \phi}(s', \phi)}{\sqrt{\mathbf{R}_{s'}(s', \phi) \cdot \mathbf{R}_{s'}(s', \phi)}}.\end{aligned}$$

In order to complete the list of quantities needed to determine the directional derivative, we calculate the various derivatives of $\mathbf{R}(s, \phi)$. Recalling that

$$\mathbf{R}(s, \phi) = \mathbf{r}(s) + a\mathbf{e}_1(s) \cos \phi + a\mathbf{e}_2(s) \sin \phi$$

we derive

$$\begin{aligned}\mathbf{R}_\phi &= -a\mathbf{e}_1 \sin \phi + a\mathbf{e}_2 \cos \phi \\ \mathbf{R}_s &= -\mathbf{e}_1 a\Omega_3 \sin \phi + \mathbf{e}_2 a\Omega_3 \cos \phi + \mathbf{e}_3(1 - a(\Omega_2 \cos \phi - \Omega_1 \sin \phi)) \\ \mathbf{R}_{s, \phi} &= -a\Omega_3(\mathbf{e}_1 \cos \phi + \mathbf{e}_2 \sin \phi) + a\mathbf{e}_3(\Omega_1 \cos \phi + \Omega_2 \sin \phi)\end{aligned}$$

and therefore

$$\begin{aligned}\mathbf{R}_\phi \cdot \mathbf{R}_\phi &= a^2 \\ \mathbf{R}_\phi \cdot \mathbf{R}_s &= a^2 \Omega_3 \\ \mathbf{R}_s \cdot \mathbf{R}_s &= 1 - 2a(\Omega_2 \cos \phi - \Omega_1 \sin \phi) + a^2(\Omega_3^2 + (\Omega_2 \cos \phi - \Omega_1 \sin \phi)^2) \\ \mathbf{R}_{s, \phi} \cdot \mathbf{R}_s &= a(1 - a(\Omega_2 \cos \phi - \Omega_1 \sin \phi))(\Omega_1 \cos \phi + \Omega_2 \sin \phi)\end{aligned}$$

Putting all the above expressions together and substituting them into

$$\mathbf{n} \cdot \nabla L = \frac{n_s}{|\mathbf{R}_s|} \partial_s L + \frac{n_\phi}{|\mathbf{R}_\phi|} \partial_\phi L$$

we can expand the result in powers of a , finally leading to

$$\mathbf{n} \cdot \nabla L = -a\Omega_3 + \cos \phi \int_0^s \Omega_1(s') ds' + \sin \phi \int_0^s \Omega_2(s') ds' + \mathcal{O}(a^2),$$

implying that

$$\Delta(s, \phi) = -a^2 \Omega_3(s) + a \cos \phi \int_0^s \Omega_1(s') ds' + a \sin \phi \int_0^s \Omega_2(s') ds' + \mathcal{O}(a^3).$$

For completeness we present the informative expansions of $n_s, n_\phi, \partial_\phi L, \partial_s L, |\mathbf{R}_\phi|, |\mathbf{R}_s|$ below

$$\begin{aligned}
|\mathbf{R}_\phi| &= a \\
|\mathbf{R}_s| &= 1 - a(\Omega_2 \cos \phi - \Omega_1 \sin \phi) + \mathcal{O}(a^2) \\
n_s &= -\Omega_3 a - \Omega_3 a^2 (\Omega_2 \cos \phi - \Omega_1 \sin \phi) + \mathcal{O}(a^3) \\
n_\phi &= 1 + \frac{1}{2} \Omega_3^2 a^2 + \mathcal{O}(a^3) \\
\partial_s L &= 1 - a(\Omega_2 \cos \phi - \Omega_1 \sin \phi) + \mathcal{O}(a^2) \\
\partial_\phi L &= a \sin \int_0^s \Omega_2(s') ds' + a \cos \phi \int_0^s \Omega_1(s') ds' + \mathcal{O}(a^3) \quad .
\end{aligned}$$

Variational discussion

Here we derive the variational terms of the 3D enthalpy functional. The starting point is the group of relations that define the curvatures and twist of our right handed orthonormal co-ordinate system Eq. (2.2). In the following we will derive how the quantities Ω_i change given small variations of the axonemal configuration (i.e. when $\mathbf{r} \rightarrow r + \delta\mathbf{r}$, $\mathbf{e}_1 \rightarrow \mathbf{e}_1 + \delta\mathbf{e}_1$ and $\mathbf{e}_2 \rightarrow \mathbf{e}_2 + \delta\mathbf{e}_2$). In order to do this we first have to derive equations for the change in the basis vectors \mathbf{e}_i . First of all note that due to the constraint that s has to remain the arclength under variations

$$\delta\mathbf{e}_3 = \delta(\mathbf{r}_s) \neq (\delta\mathbf{r})_s \quad .$$

Let

$$\mathbf{r} \rightarrow \mathbf{r} + \delta\mathbf{r}$$

then the following vectors will be tangential to the new curve

$$\mathbf{r}_s + (\delta\mathbf{r})_s \quad .$$

For small variations the normalisation factor will then be given by

$$\frac{1}{|\mathbf{r}_s + (\delta\mathbf{r})_s|} = \frac{1}{\sqrt{\mathbf{r}_s \cdot \mathbf{r}_s + 2(\delta\mathbf{r})_s \cdot \mathbf{r}_s + \text{h.o.t.}}} \simeq 1 - (\delta\mathbf{r})_s \cdot \mathbf{r}_s \quad ,$$

and hence the unit tangent vectors

$$\mathbf{r}_s + (\delta\mathbf{r})_s - ((\delta\mathbf{r})_s \cdot \mathbf{r}_s) \mathbf{r}_s \quad .$$

Defining the change in the unit tangent vector

$$\mathbf{e}_3 \rightarrow \mathbf{e}_3 + \delta\mathbf{e}_3$$

we arrive at

$$\boxed{\delta\mathbf{e}_3 = (\delta\mathbf{r})_s - ((\delta\mathbf{r})_s \cdot \mathbf{r}_s) \mathbf{r}_s}$$

The corresponding relations for $\delta\mathbf{e}_2, \delta\mathbf{e}_2$ follow from the orthogonality of $\mathbf{e}_1, \mathbf{e}_2, \mathbf{e}_3$. Let

$$\begin{aligned}\mathbf{e}_1 &\rightarrow \mathbf{e}_1 + \delta\mathbf{e}_1 \\ \mathbf{e}_2 &\rightarrow \mathbf{e}_2 + \delta\mathbf{e}_2 \quad ,\end{aligned}$$

then orthogonality implies

$$\begin{aligned}(\mathbf{e}_1 + \delta\mathbf{e}_1) \cdot (\mathbf{e}_3 + \delta\mathbf{e}_3) &= 0 \\ (\mathbf{e}_2 + \delta\mathbf{e}_2) \cdot (\mathbf{e}_3 + \delta\mathbf{e}_3) &= 0\end{aligned}$$

and therefore

$$\begin{aligned}\mathbf{e}_3 \cdot \delta\mathbf{e}_1 + \mathbf{e}_1 \cdot (\delta\mathbf{r})_s &= 0 \\ \mathbf{e}_3 \cdot \delta\mathbf{e}_2 + \mathbf{e}_2 \cdot (\delta\mathbf{r})_s &= 0 \quad .\end{aligned}$$

Multiplication with \mathbf{e}_3 yields

$$\begin{aligned}(\delta\mathbf{e}_1 \cdot \mathbf{e}_3)\mathbf{e}_3 &= -(\mathbf{e}_1 \cdot (\delta\mathbf{r})_s)\mathbf{e}_3 \\ (\delta\mathbf{e}_2 \cdot \mathbf{e}_3)\mathbf{e}_3 &= -(\mathbf{e}_2 \cdot (\delta\mathbf{r})_s)\mathbf{e}_3 \quad .\end{aligned}$$

Since $\delta\mathbf{e}_1 \cdot \mathbf{e}_1 = \delta\mathbf{e}_2 \cdot \mathbf{e}_2 = 0$ we can write

$$\begin{aligned}\delta\mathbf{e}_1 &= (\delta\mathbf{e}_1 \cdot \mathbf{e}_2)\mathbf{e}_2 + (\delta\mathbf{e}_1 \cdot \mathbf{e}_3)\mathbf{e}_3 \\ \delta\mathbf{e}_2 &= (\delta\mathbf{e}_2 \cdot \mathbf{e}_1)\mathbf{e}_1 + (\delta\mathbf{e}_2 \cdot \mathbf{e}_3)\mathbf{e}_3\end{aligned}$$

leading to

$$\begin{aligned}\delta\mathbf{e}_1 &= (\delta\mathbf{e}_1 \cdot \mathbf{e}_2)\mathbf{e}_2 - (\mathbf{e}_1 \cdot (\delta\mathbf{r})_s)\mathbf{e}_3 \\ \delta\mathbf{e}_2 &= (\delta\mathbf{e}_2 \cdot \mathbf{e}_1)\mathbf{e}_1 - (\mathbf{e}_2 \cdot (\delta\mathbf{r})_s)\mathbf{e}_3 \quad .\end{aligned}$$

Defining the rotation angle $\delta\chi = \mathbf{e}_2 \cdot \delta\mathbf{e}_1$ and making use of $(\mathbf{e}_1 + \delta\mathbf{e}_1) \cdot (\mathbf{e}_2 + \delta\mathbf{e}_2) = 0$ which implies $\mathbf{e}_1 \cdot \delta\mathbf{e}_2 = -\mathbf{e}_2 \cdot \delta\mathbf{e}_1$ we arrive at

$$\boxed{\begin{aligned}\delta\mathbf{e}_1 &= \delta\chi\mathbf{e}_2 - (\mathbf{e}_1 \cdot (\delta\mathbf{r})_s)\mathbf{e}_3 \\ \delta\mathbf{e}_2 &= -\delta\chi\mathbf{e}_1 - (\mathbf{e}_2 \cdot (\delta\mathbf{r})_s)\mathbf{e}_3\end{aligned}} \quad .$$

Now that we have expressed $\delta\mathbf{e}_i$ in terms of the principal variations $\delta\mathbf{r}$ and $\delta\chi$ we can determine the resulting variations $\delta\Omega_i$. They can be read off from the relations of the varied unit normal vectors $\partial_s\mathbf{e}_i \rightarrow \partial_{s'}(\mathbf{e}_i + \delta\mathbf{e}_i)$ where s' is the arclength of the varied system and defined by

$$\begin{aligned}\frac{ds}{ds'} &= \frac{1}{\sqrt{1 + 2(\delta\mathbf{r})_s \cdot \mathbf{r}_s + \text{h.o.t.}}} \\ &\simeq 1 - (\delta\mathbf{r})_s \cdot \mathbf{r}_s \quad .\end{aligned}$$

Let

$$\begin{aligned}ds' &= ds + \delta(ds) \\ &\simeq (1 + (\delta\mathbf{r})_s \cdot \mathbf{e}_3)ds \\ &\Rightarrow \delta(ds) = ((\delta\mathbf{r})_s \cdot \mathbf{e}_3)ds \quad .\end{aligned}$$

Hence writing Eq. (2.2) as

$$\partial_s \mathbf{e}_i = \boldsymbol{\Omega} \times \mathbf{e}_i$$

where $\boldsymbol{\Omega} = \sum_i \Omega_i \mathbf{e}_i$, the following equation with $\delta \boldsymbol{\Omega} = \delta \Omega_i \mathbf{e}_i$

$$(1 - (\delta \mathbf{r})_s \cdot \mathbf{r}_s) \partial_s (\mathbf{e}_i + \delta \mathbf{e}_i) = (\boldsymbol{\Omega} + \delta \boldsymbol{\Omega}) \times (\mathbf{e}_i + \delta \mathbf{e}_i)$$

defines $\delta \Omega_i$ by simple (but tedious) substitution of the previous result for $\delta \mathbf{e}_i$, finally leading to the following result

$$\begin{aligned} \delta \Omega_1 &= \delta \chi \Omega_2 - \mathbf{e}_2 \cdot (\delta \mathbf{r})_{ss} - 2\Omega_1 \mathbf{e}_3 \cdot (\delta \mathbf{r})_s \\ \delta \Omega_2 &= -\delta \chi \Omega_1 + \mathbf{e}_1 \cdot (\delta \mathbf{r})_{ss} - 2\Omega_2 \mathbf{e}_3 \cdot (\delta \mathbf{r})_s \\ \delta \Omega_3 &= (\delta \chi)_s + (\Omega_1 \mathbf{e}_1 + \Omega_2 \mathbf{e}_2 - \Omega_3 \mathbf{e}_3) \cdot (\delta \mathbf{r})_s \quad . \end{aligned}$$

Integrating variational terms by parts

Here we present the detailed derivation of the terms determined by partially integrating the variational terms. Substituting the expressions for $\delta(ds)$, $\delta\Omega_1(s)$, $\delta\Omega_2(s)$, $\delta\Omega_3(s)$ into the equation for δG we get

$$\begin{aligned} \delta G = & \int_0^L [H\mathbf{e}_3 \cdot (\delta\mathbf{r})_s + (\kappa_1\Omega_1 - \pi aF_1)(\delta\chi\Omega_2 - \mathbf{e}_2 \cdot (\delta\mathbf{r})_{ss} - 2\Omega_1\mathbf{e}_3 \cdot (\delta\mathbf{r})_s) \\ & + (\kappa_2\Omega_2 - \pi aF_2)(-\delta\chi\Omega_1 + \mathbf{e}_1 \cdot (\delta\mathbf{r})_{ss} - 2\Omega_2\mathbf{e}_3 \cdot (\delta\mathbf{r})_s) \\ & + (\kappa_3\Omega_3 - 2\pi a^2f_0)((\delta\chi)_s + (\Omega_1\mathbf{e}_1 + \Omega_2\mathbf{e}_2 - \Omega_3\mathbf{e}_3) \cdot (\delta\mathbf{r})_s)] ds \quad . \end{aligned}$$

Ordering terms we write

$$\delta G = I_1 + I_2 + I_3 + I_4 \quad ,$$

where

$$\begin{aligned} I_1 = & \int_0^L [(\mathbf{e}_3H - 2\Omega_1\mathbf{e}_3(\kappa_1\Omega_1 - \pi aF_1) - 2\Omega_2\mathbf{e}_3(\kappa_2\Omega_2 - \pi aF_2) \\ & + (\kappa_3\Omega_3 - 2\pi a^2f_0)(\Omega_1\mathbf{e}_1 + \Omega_2\mathbf{e}_2 - \Omega_3\mathbf{e}_3)) \cdot (\delta\mathbf{r})_s] ds \\ I_2 = & \int_0^L [(-\mathbf{e}_2(\kappa_2\Omega_2 - \pi aF_2) + \mathbf{e}_1(\kappa_2\Omega_2 - \pi aF_2)) \cdot (\delta\mathbf{r})_{ss}] ds \\ I_3 = & \int_0^L [(\kappa_3\Omega_3 - 2\pi a^2f_0)(\delta\chi)_s] ds \\ I_4 = & \int_0^L [(\Omega_2(\kappa_1\Omega_1 - \pi aF_1) - \Omega_1(\kappa_2\Omega_2 - \pi aF_2))\delta\chi] ds \quad . \end{aligned}$$

Re-ordering the terms and integrating by parts yields

$$\begin{aligned}
I_1 &= \left[(\mathbf{e}_1 \Omega_1 (\kappa_3 \Omega_3 - 2\pi a^2 \mathbf{f}_0) + \mathbf{e}_2 (\kappa_3 \Omega_3 - 2\pi a^2 \mathbf{f}_0) \right. \\
&\quad \left. + \mathbf{e}_3 \left(-\frac{3}{2} \kappa_1 \Omega_1^2 - \frac{3}{2} \kappa_2 \Omega_2^2 - \frac{1}{2} \kappa_3 \Omega_3^2 - \Lambda + \pi a (\Omega_1 F_1 + \Omega_2 F_2) \right) \right]_{s=0}^{s=L} (\delta \mathbf{r}) \\
&\quad - \int_0^L \left\{ \partial_s \left(\mathbf{e}_1 \Omega_1 (\kappa_3 \Omega_3 - 2\pi a^2 \mathbf{f}_0) + \mathbf{e}_2 (\kappa_3 \Omega_3 - 2\pi a^2 \mathbf{f}_0) \right. \right. \\
&\quad \left. \left. + \mathbf{e}_3 \left(-\frac{3}{2} \kappa_1 \Omega_1^2 - \frac{3}{2} \kappa_2 \Omega_2^2 - \frac{1}{2} \kappa_3 \Omega_3^2 - \Lambda + \pi a (\Omega_1 F_1 + \Omega_2 F_2) \right) \right) \right\} \cdot (\delta \mathbf{r}) ds \\
I_2 &= \left[(\mathbf{e}_1 (\kappa_2 \Omega_2 - \pi a F_2) - \mathbf{e}_2 (\kappa_1 \Omega_1 - \pi a F_1)) \cdot (\delta \mathbf{r})_s \right]_{s=0}^{s=L} \\
&\quad - \left[(\mathbf{e}_1 (\kappa_2 \dot{\Omega}_2 - \pi a \mathbf{f}_2 + \Omega_3 (\kappa_1 \Omega_1 - \pi a F_1)) - \mathbf{e}_2 (\kappa_1 \dot{\Omega}_1 - \pi a \mathbf{f}_1 - \Omega_3 (\kappa_2 \Omega_2 - \pi a F_2)) \right. \\
&\quad \left. - \mathbf{e}_3 (\Omega_1 (\kappa_1 \Omega_1 - \pi a F_1) + \Omega_2 (\kappa_2 \Omega_2 - \pi a F_2)) \right]_{s=0}^{s=L} (\delta \mathbf{r}) \\
&\quad + \int_0^L \left\{ \partial_s \left(\mathbf{e}_1 (\kappa_2 \dot{\Omega}_2 - \pi a \mathbf{f}_2 + \Omega_3 (\kappa_1 \Omega_1 - \pi a F_1)) - \mathbf{e}_2 (\kappa_1 \dot{\Omega}_1 - \pi a \mathbf{f}_1 - \Omega_3 (\kappa_2 \Omega_2 - \pi a F_2)) \right. \right. \\
&\quad \left. \left. - \mathbf{e}_3 (\Omega_1 (\kappa_1 \Omega_1 - \pi a F_1) + \Omega_2 (\kappa_2 \Omega_2 - \pi a F_2)) \right) \right\} \cdot (\delta \mathbf{r}) ds \\
I_3 &= \left[(\kappa_3 \Omega_3 - 2\pi a^2 \mathbf{f}_0) (\delta \chi) \right]_{s=0}^{s=L} - \int_0^L (\kappa_3 \dot{\Omega}_3 - 2\pi a^2 \dot{\mathbf{f}}_0) \delta \chi ds \quad .
\end{aligned}$$

After adding all the terms together we find that

$$\delta G = \text{B.T.} + \int_0^L \left(\frac{\delta G}{\delta \mathbf{r}} \delta \mathbf{r} + \frac{\delta G}{\delta \chi} \delta \chi \right) ds \quad ,$$

where the variational derivatives are given by

$$\begin{aligned}
\frac{\delta G}{\delta \mathbf{r}} &= \partial_s \left[\mathbf{e}_1 (2\pi a^2 \mathbf{f}_0 \Omega_1 - a\pi (F_1 \Omega_3 + \mathbf{f}_2) - (\kappa_3 - \kappa_1) \Omega_1 \Omega_3 + \kappa_2 \dot{\Omega}_2) \right. \\
&\quad \left. + \mathbf{e}_2 (2\pi a^2 \mathbf{f}_0 \Omega_2 - a\pi (F_2 \Omega_3 - \mathbf{f}_1) - (\kappa_3 - \kappa_2) \Omega_2 \Omega_3 - \kappa_1 \dot{\Omega}_1) \right. \\
&\quad \left. + \mathbf{e}_3 \left(\Lambda + \frac{\kappa_1}{2} \Omega_1^2 + \frac{\kappa_2}{2} \Omega_2^2 + \frac{\kappa_3}{2} \Omega_3^2 \right) \right] \\
&\quad \underbrace{\hspace{10em}}_{-\tau}
\end{aligned}$$

$$\frac{\delta G}{\delta \chi} = a\pi (F_2 \Omega_1 - F_1 \Omega_2) + 2\pi a^2 \dot{\mathbf{f}}_0 - \kappa_3 \dot{\Omega}_3 + (\kappa_1 - \kappa_2) \Omega_1 \Omega_2 \quad ,$$

with following boundary terms

$$\text{B.T.} = \left[\frac{\delta G}{\delta \mathbf{r}} \cdot (\delta \mathbf{r}) \right]_{s=0}^{s=L} + \left[(\mathbf{e}_1 (\kappa_2 \Omega_2 - \pi a F_2) - \mathbf{e}_2 (\kappa_1 \Omega_1 - \pi a F_1)) \cdot (\delta \mathbf{r})_s \right]_{s=0}^{s=L} + \left[(\kappa_3 \Omega_3 - 2\pi a^2 \mathbf{f}_0) (\delta \chi) \right]_{s=0}^{s=L}$$

Three dimensional non-linear equations and boundary terms

Here we present the explicit non-linear equations and boundary conditions corresponding to a clamped three-dimensional axoneme, as well as various limiting cases.

The incompressibility constraint

The incompressibility constraint reads

$$\begin{aligned}
\ddot{\tau} - \frac{\xi_{\parallel}}{\xi_{\perp}} \tau (\Omega_1^2 + \Omega_2^2) = & \\
& - \dot{\Omega}_1 (a\pi(F_2\Omega_3 - f_1) + \kappa_1\dot{\Omega}_1) + \dot{\Omega}_2 (a\pi(F_1\Omega_3 + f_2) - \kappa_2\dot{\Omega}_2) - \dot{\Omega}_3\Omega_1\Omega_2(\kappa_1 - \kappa_2) \\
& - \Omega_1(a\pi(f_2\Omega_3 + F_2\dot{\Omega}_3 - \dot{f}_1) + (\kappa_1 - \kappa_2)\Omega_3\dot{\Omega}_2 + \kappa_1\ddot{\Omega}_1) \\
& + \Omega_2(a\pi(f_1\Omega_3 + F_1\dot{\Omega}_3 + \dot{f}_2) - (\kappa_1 - \kappa_2)\Omega_3\dot{\Omega}_1 - \kappa_2\ddot{\Omega}_2) \\
& + \frac{\xi_{\parallel}}{\xi_{\perp}} [\Omega_3^2(\Omega_1^2(\kappa_1 - \kappa_3) + \Omega_2^2(\kappa_2 - \kappa_3) - a\pi(F_2\Omega_2 - F_1\Omega_1)) - \kappa_1\Omega_1\ddot{\Omega}_1 - \kappa_2\Omega_2\ddot{\Omega}_2 \\
& + 2\Omega_3(a\pi(\Omega_2f_1 - \Omega_1f_2 + af_0(\Omega_1^2 + \Omega_2^2)) - (\kappa_1 + \frac{1}{2}\kappa_3)\Omega_2\dot{\Omega}_1 + (\kappa_2 + \frac{1}{2}\kappa_3)\Omega_1\dot{\Omega}_2) \\
& + a\pi(\Omega_1\dot{f}_1 + \Omega_2\dot{f}_2 - 2af_0(\Omega_2\dot{\Omega}_1 + \Omega_1\dot{\Omega}_2)) + \dot{\Omega}_3(a\pi(F_1\Omega_2 - F_2\Omega_1) + (\kappa_2 - \kappa_1)\Omega_1\Omega_2)] .
\end{aligned} \tag{D.1}$$

The force-balance equations

The force-balance equations are given by

$$\begin{aligned}
\xi_{\perp} \partial_t \Omega_1 - a\pi \ddot{f}_1 + \kappa_1 \ddot{\Omega}_1 &= \text{term1} + \frac{\xi_{\perp}}{\xi_{\parallel}} \text{term2} + \frac{\xi_{\perp}}{\xi_r} \text{term3} \\
\xi_{\perp} \partial_t \Omega_2 - a\pi \ddot{f}_2 + \kappa_2 \ddot{\Omega}_2 &= \text{term4} + \frac{\xi_{\perp}}{\xi_{\parallel}} \text{term5} + \frac{\xi_{\perp}}{\xi_r} \text{term6} \\
\xi_r \partial_t \Omega_3 + 2a^2 \pi \ddot{f}_0 - \kappa_3 \ddot{\Omega}_3 &= \text{term7} + \frac{\xi_r}{\xi_{\perp}} \text{term8} ,
\end{aligned}$$

where the individual terms are given as follows:

- **term1:**

$$\begin{aligned}
& (a\pi F_1 + (-\kappa_1 + \kappa_3)\Omega_1)\Omega_3^4 + \Omega_1^3(-\tau + \Omega_3(-2a^2\pi f_0 + (-\kappa_1 + \kappa_3)\Omega_3)) \\
& + \Omega_1\Omega_2^2(-\tau + \Omega_3(-2a^2\pi f_0 + (-\kappa_2 + \kappa_3)\Omega_3)) + 2(a^2\pi f_0\Omega_1\Omega_2 + \dot{\tau})\dot{\Omega}_1 \\
& + \Omega_3^3(-2a^2\pi f_0\Omega_1 + 4a\pi f_2 + (-4\kappa_2 + 3\kappa_3)\dot{\Omega}_2) - 3(a\pi F_1 + (-\kappa_1 + \kappa_3)\Omega_1)\dot{\Omega}_3^2 \\
& + \tau\ddot{\Omega}_1 + \Omega_3^2(-\tau\Omega_1 - 6a^2\pi(\Omega_2\dot{f}_0 + f_0\dot{\Omega}_2) - 6(\kappa_2 - \kappa_3)\Omega_2\dot{\Omega}_3 \\
& + a\pi(F_1\Omega_1^2 + F_2(\Omega_1\Omega_2 + 6\dot{\Omega}_3) - 6\dot{f}_1) - 3(-2\kappa_1 + \kappa_3)\ddot{\Omega}_1) \\
& + \Omega_1^2(-2a^2\pi f_0\dot{\Omega}_2 - (2\kappa_2 - \kappa_3)\Omega_3\dot{\Omega}_2 - \kappa_2\Omega_2\dot{\Omega}_3 + a\pi(2\Omega_3f_2 + F_2\dot{\Omega}_3 - \dot{f}_1) \\
& + \kappa_1(\Omega_2\dot{\Omega}_3 + \ddot{\Omega}_1)) + \dot{\Omega}_3(-\tau\Omega_2 + 3(4\kappa_1 - 3\kappa_3)\Omega_3\dot{\Omega}_1 + 6a^2\pi(\Omega_1\dot{f}_0 + f_0(-\Omega_2\Omega_3 + \dot{\Omega}_1)) \\
& - a\pi(F_1\Omega_1\Omega_2 + 6(2\Omega_3f_1 + \dot{f}_2))) - 3(-2\kappa_2 + \kappa_3)\ddot{\Omega}_2 + \Omega_1(\ddot{\tau} + \Omega_2(-a\pi\dot{f}_2 + \kappa_2\ddot{\Omega}_2)) \\
& + (2a^2\pi f_0\Omega_1 + 4(\kappa_1 - \kappa_3)\Omega_1\Omega_3 - 4a\pi(F_1\Omega_3 + f_2) + (4\kappa_2 - 3\kappa_3)\dot{\Omega}_2)\ddot{\Omega}_3 \\
& + 2a^2\pi(3\dot{\Omega}_2\dot{f}_0 + 3\dot{f}_0\ddot{\Omega}_2 + \Omega_2f_0^{(3)}) + \Omega_3(\Omega_2(-2\dot{\tau} + \Omega_1(-2a\pi f_1 + (2\kappa_1 - \kappa_3)\dot{\Omega}_1)) \\
& - 2\tau\dot{\Omega}_2 + 2a\pi(3a(2\dot{f}_0\dot{\Omega}_1 + \Omega_1\ddot{f}_0 + f_0\ddot{\Omega}_1) - \dot{f}_2)) \\
& + (2a^2\pi f_0 + (4\kappa_2 - \kappa_3)\Omega_3)\ddot{\Omega}_2 + (-a\pi F_2 + (\kappa_2 - \kappa_3)\Omega_2)\ddot{\Omega}_3
\end{aligned}$$

- **term2:**

$$\begin{aligned}
& (a\pi F_1 + (-\kappa_1 + \kappa_2)\Omega_1)\Omega_2^2\Omega_3^2 + \dot{\tau}\dot{\Omega}_1 \\
& + \Omega_1\Omega_2\Omega_3(-a\pi(F_2\Omega_3 + f_1) + (2\kappa_1 - 3\kappa_2)\dot{\Omega}_1) - \Omega_2(\Omega_3\dot{\tau} + a\pi(F_1\Omega_3 + f_2)\dot{\Omega}_1) \\
& + \kappa_2\Omega_2\dot{\Omega}_1\dot{\Omega}_2 + \Omega_2^2\Omega_3(a\pi f_2 - \kappa_2\dot{\Omega}_2) + (2(\kappa_1 - \kappa_2)\Omega_1^2\Omega_2 + 2a\pi\Omega_1(F_2\Omega_1 - F_1\Omega_2))\dot{\Omega}_3 \\
& + \Omega_1(3\kappa_1\dot{\Omega}_1^2 + a(3\pi(F_2\Omega_3 - f_1)\dot{\Omega}_1 - 2\pi(F_1\Omega_3 + f_2)\dot{\Omega}_2) + 2(\kappa_2\dot{\Omega}_2^2 + \ddot{\tau}) \\
& + \Omega_1(2a\pi(\Omega_3f_2 - \dot{f}_1) + 2((\kappa_1 - \kappa_2)\Omega_3\dot{\Omega}_2 + \kappa_1\ddot{\Omega}_1))) + \Omega_1\Omega_2(-2a\pi\dot{f}_2 + 2\kappa_2\ddot{\Omega}_2)
\end{aligned}$$

- **term3:**

$$a\pi\Omega_2(-F_2\Omega_1 + F_1\Omega_2) - 2a^2\pi\Omega_2\dot{f}_0 + \Omega_2((-\kappa_1 + \kappa_2)\Omega_1\Omega_2 + \kappa_3\dot{\Omega}_3)$$

- **term4:**

$$\begin{aligned}
& \Omega_2(\Omega_1^2(-\tau - 2a^2\pi f_0\Omega_3 + (-\kappa_1 + \kappa_3)\Omega_3^2) + \Omega_2^2(-\tau - 2a^2\pi f_0\Omega_3 + (-\kappa_2 + \kappa_3)\Omega_3^2)) \\
& + \Omega_3^3(-2a^2\pi f_0\Omega_2 + (a\pi F_2 + (-\kappa_2 + \kappa_3)\Omega_2)\Omega_3 - 4a\pi f_1 + (4\kappa_1 - 3\kappa_3)\dot{\Omega}_1) \\
& + (-2a^2\pi f_0\Omega_1\Omega_2 + 2\dot{\tau})\dot{\Omega}_2 + \dot{\Omega}_3(\tau\Omega_1 + 3(4\kappa_2 - 3\kappa_3)\Omega_3\dot{\Omega}_2 + 6a^2\pi(\Omega_2\dot{f}_0 + f_0(\Omega_1\Omega_3 + \dot{\Omega}_2)) \\
& + (-3a\pi F_2 + 3(\kappa_2 - \kappa_3)\Omega_2)\dot{\Omega}_3 + a\pi(F_2\Omega_1\Omega_2 + 6(-2\Omega_3f_2 + \dot{f}_1)) + 3(-2\kappa_1 + \kappa_3)\ddot{\Omega}_1) \\
& + \Omega_2(\ddot{\tau} + \Omega_1(-a\pi\dot{f}_1 + \kappa_1\ddot{\Omega}_1)) + \tau\ddot{\Omega}_2 + \Omega_3^2(-\tau\Omega_2 + 6a^2\pi(\Omega_1\dot{f}_0 + f_0\dot{\Omega}_1) \\
& + 6(\kappa_1 - \kappa_3)\Omega_1\dot{\Omega}_3 + a\pi(F_2\Omega_2^2 + F_1(\Omega_1\Omega_2 - 6\dot{\Omega}_3) - 6\dot{f}_2) - 3(-2\kappa_2 + \kappa_3)\ddot{\Omega}_2) \\
& + \Omega_2^2(2a^2\pi f_0\dot{\Omega}_1 - \kappa_3\Omega_3\dot{\Omega}_1 + \kappa_1(2\Omega_3\dot{\Omega}_1 + \Omega_1\dot{\Omega}_3) - a\pi(2\Omega_3f_1 + F_1\dot{\Omega}_3 + \dot{f}_2) \\
& + \kappa_2(-\Omega_1\dot{\Omega}_3 + \ddot{\Omega}_2)) \\
& + (2a^2\pi f_0\Omega_2 + 4(\kappa_2 - \kappa_3)\Omega_2\Omega_3 + 4a\pi(-F_2\Omega_3 + f_1) + (-4\kappa_1 + 3\kappa_3)\dot{\Omega}_1)\dot{\Omega}_3 \\
& + \Omega_3(2\tau\dot{\Omega}_1 + \Omega_1(2\dot{\tau} + (-2\kappa_2 + \kappa_3)\Omega_2\dot{\Omega}_2) + 6a^2\pi(2\dot{f}_0\dot{\Omega}_2 + \Omega_2\dot{f}_0 + f_0\dot{\Omega}_2) \\
& + 2a\pi(\Omega_1\Omega_2f_2 + 2\dot{f}_1)) \\
& - 2a^2\pi(3\dot{\Omega}_1\dot{f}_0 + 3\dot{f}_0\ddot{\Omega}_1 + \Omega_1f_0^{(3)}) \\
& + (-2a^2\pi f_0 + (-4\kappa_1 + \kappa_3)\Omega_3)\ddot{\Omega}_1 + (a\pi F_1 + (-\kappa_1 + \kappa_3)\Omega_1)\ddot{\Omega}_3
\end{aligned}$$

- **term5:**

$$\begin{aligned}
& \Omega_1^2(a\pi F_2 + (\kappa_1 - \kappa_2)\Omega_2)\Omega_3^2 - \Omega_1\Omega_3(-\dot{\tau} + \Omega_1(a\pi f_1 - \kappa_1\dot{\Omega}_1)) \\
& + (\dot{\tau} + a\pi\Omega_1(F_2\Omega_3 - f_1))\dot{\Omega}_2 + \kappa_1\Omega_1\dot{\Omega}_1\dot{\Omega}_2 \\
& + \Omega_1\Omega_2\Omega_3(-a\pi F_1\Omega_3 + a\pi f_2 + (3\kappa_1 - 2\kappa_2)\dot{\Omega}_2) \\
& + (2(\kappa_1 - \kappa_2)\Omega_1\Omega_2^2 + 2a\pi\Omega_2(F_2\Omega_1 - F_1\Omega_2))\dot{\Omega}_3 + \Omega_1\Omega_2(-2a\pi\dot{f}_1 + 2\kappa_1\ddot{\Omega}_1) \\
& + \Omega_2(2\kappa_1\dot{\Omega}_1^2 + 3\kappa_2\dot{\Omega}_2^2 + a(2\pi(F_2\Omega_3 - f_1)\dot{\Omega}_1 - 3\pi(F_1\Omega_3 + f_2)\dot{\Omega}_2) \\
& + 2\ddot{\tau} + \Omega_2(2(\kappa_1 - \kappa_2)\Omega_3\dot{\Omega}_1 - 2a\pi(\Omega_3f_1 + \dot{f}_2) + 2\kappa_2\ddot{\Omega}_2))
\end{aligned}$$

- **term6:**

$$a\pi\Omega_1(F_2\Omega_1 - F_1\Omega_2) + 2a^2\pi\Omega_1\dot{f}_0 - \Omega_1((-\kappa_1 + \kappa_2)\Omega_1\Omega_2 + \kappa_3\dot{\Omega}_3)$$

- **term7:**

$$\Omega_2(a\pi f_1 + (-\kappa_1 + \kappa_2)\dot{\Omega}_1) + \Omega_1(-a\pi f_2 - \kappa_1\dot{\Omega}_2 + \kappa_2\dot{\Omega}_2) + a\pi(-F_2\dot{\Omega}_1 + F_1\dot{\Omega}_2)$$

- **term8:**

$$\begin{aligned}
& (\kappa_1\Omega_1^2 + \kappa_2\Omega_2^2 - \kappa_3(\Omega_1^2 + \Omega_2^2))\Omega_3^3 + (\Omega_1^2 + \Omega_2^2)(\tau\Omega_3 + 2a^2\pi f_0\Omega_3^2) + 3(-\kappa_1 + \kappa_2)\Omega_1\Omega_2\Omega_3\dot{\Omega}_3 \\
& - 2a^2\pi(\Omega_1^2 + \Omega_2^2)\ddot{f}_0 - ((\kappa_1 - \kappa_3)\Omega_1^2 + (\kappa_2 - \kappa_3)\Omega_2^2)\ddot{\Omega}_3 + \\
& \Omega_2(-\tau\dot{\Omega}_1 - 3\kappa_2\dot{\Omega}_2\dot{\Omega}_3 + 2\kappa_3(\Omega_3^2\dot{\Omega}_1 + \dot{\Omega}_2\dot{\Omega}_3) + (-3\kappa_2 + \kappa_3)\Omega_3\ddot{\Omega}_2 \\
& - 2a^2\pi(2\dot{f}_0\dot{\Omega}_2 + f_0(2\Omega_3\dot{\Omega}_1 + \ddot{\Omega}_2)) \\
& + a\pi(3\Omega_3^2f_1 + 3f_2\dot{\Omega}_3 + 3\Omega_3(F_1\dot{\Omega}_3 + \dot{f}_2) + F_2(-\Omega_3^3 + \ddot{\Omega}_3) - \ddot{f}_1) \\
& + \kappa_1(-3\Omega_3^2\dot{\Omega}_1 + \ddot{\Omega}_1)) \\
& + \Omega_1(\tau\dot{\Omega}_2 - 2\kappa_3\Omega_3^2\dot{\Omega}_2 - 3\kappa_1\dot{\Omega}_1\dot{\Omega}_3 + 2\kappa_3\dot{\Omega}_1\dot{\Omega}_3 + (-3\kappa_1 + \kappa_3)\Omega_3\ddot{\Omega}_1 \\
& - 2a^2\pi(2\dot{f}_0\dot{\Omega}_1 + f_0(-2\Omega_3\dot{\Omega}_2 + \ddot{\Omega}_1)) \\
& + a\pi(-3\Omega_3^2f_2 + 3f_1\dot{\Omega}_3 + \Omega_3(-3F_2\dot{\Omega}_3 + 3\dot{f}_1) + F_1(-\Omega_3^3 + \ddot{\Omega}_3) + \ddot{f}_2) \\
& + \kappa_2(3\Omega_3^2\dot{\Omega}_2 - \ddot{\Omega}_2))
\end{aligned}$$

Boundary terms

Discussing an axoneme whose base is clamped, we impose at $s = 0$

$$\begin{aligned}
\partial_t \chi &= 0 \\
\partial_t \mathbf{r} &= 0 \\
\partial_t \mathbf{r}_s &= 0 \quad ,
\end{aligned}$$

which corresponds to the following conditions on Ω_i, τ at $s = 0$

$$\begin{aligned} \partial_t \chi &= 0 \\ \Omega_1 \Omega_2 (\kappa_2 - \kappa_1) + a\pi(F_1 \Omega_2 - F_2 \Omega_1) + \kappa_3 \dot{\Omega}_3 - 2a^2 \pi \dot{f}_0 &= 0 \end{aligned}$$

$$\begin{aligned} (\partial_t \mathbf{r}) \cdot \mathbf{e}_1 &= 0 \\ \Omega_2 (\tau + 2a^2 \pi f_0 \Omega_3 + \kappa_2 \Omega_3^2 - \kappa_3 \Omega_3^2) + (-2a^2 \pi f_0 - 2\kappa_1 \Omega_3 + \kappa_3 \Omega_3) \dot{\Omega}_1 \\ + \Omega_1 (-2a^2 \pi \dot{f}_0 - \kappa_1 \dot{\Omega}_3 + \kappa_3 \dot{\Omega}_3) + a\pi(-F_2 \Omega_3^2 + 2\Omega_3 f_1 + F_1 \dot{\Omega}_3 + \dot{f}_2) - \kappa_2 \ddot{\Omega}_2 &= 0 \end{aligned}$$

$$\begin{aligned} (\partial_t \mathbf{r}) \cdot \mathbf{e}_2 &= 0 \\ \Omega_1 (-\tau - 2a^2 \pi f_0 \Omega_3 - \kappa_1 \Omega_3^2 + \kappa_3 \Omega_3^2) + (-2a^2 \pi f_0 - 2\kappa_2 \Omega_3 + \kappa_3 \Omega_3) \dot{\Omega}_2 \\ + \Omega_2 (-2a^2 \pi \dot{f}_0 - \kappa_2 \dot{\Omega}_3 + \kappa_3 \dot{\Omega}_3) + a\pi(F_1 \Omega_3^2 + 2\Omega_3 f_2 + F_2 \dot{\Omega}_3 - \dot{f}_1) + \kappa_1 \ddot{\Omega}_1 &= 0 \end{aligned}$$

$$\begin{aligned} (\partial_t \mathbf{r}) \cdot \mathbf{e}_3 &= 0 \\ \Omega_1 (-\kappa_2 \Omega_2 \Omega_3 + a\pi(F_2 \Omega_3 - f_1) + \kappa_1 (\Omega_2 \Omega_3 + \dot{\Omega}_1)) \\ + \Omega_2 (\kappa_1 \Omega_1 \Omega_3 - a\pi(F_1 \Omega_3 + f_2) + \kappa_2 (-\Omega_1 \Omega_3 + \dot{\Omega}_2)) \\ + \Omega_1 \Omega_2 \Omega_3 (\kappa_2 - \kappa_1) + \dot{\tau} &= 0 \end{aligned}$$

$$\begin{aligned} (\partial_t \mathbf{r}_s) \cdot \mathbf{e}_1 &= 0 \\ \Omega_2 (\dot{\tau} + a\pi(F_2 \Omega_1 \Omega_3 - \Omega_1 f_1 - \Omega_2 (F_1 \Omega_3 + f_2))) + \kappa_1 \Omega_1 (\Omega_2 \Omega_3 + \dot{\Omega}_1) + \kappa_2 \Omega_2 (\dot{\Omega}_2 - \Omega_1 \Omega_3) \\ + \frac{\xi_{\parallel}}{\xi_{\perp}} [-\kappa_2 \ddot{\Omega}_2 + \tau \dot{\Omega}_2 - \Omega_3^2 (3a\pi \dot{f}_2 + (2\kappa_3 - 3\kappa_2) \dot{\Omega}_2) \\ - \Omega_3 (3(\kappa_3 - \kappa_2) \Omega_2 \Omega_3 + a\pi(3F_2 \Omega_3 - 3f_1) - (2\kappa_3 - 3\kappa_1) \dot{\Omega}_1) \\ + \Omega_2 (\dot{\tau} + 2a^2 \pi (2\Omega_3 \dot{f}_0 + f_0 \dot{\Omega}_3)) + 2a^2 \pi f_0 (2\Omega_3 \dot{\Omega}_2 - \ddot{\Omega}_1) + (\kappa_3 - 3\kappa_1) \Omega_3 \ddot{\Omega}_1 \\ + \Omega_1 (\tau \Omega_3 + 2a^2 \pi (f_0 \Omega_3^2 - \dot{f}_0) + (\kappa_1 - \kappa_3) (\Omega_3^3 - \dot{\Omega}_3)) \\ + a\pi(-4a\dot{f}_0 \dot{\Omega}_1 + 3\Omega_3 \dot{f}_1 - F_1 (\Omega_3^3 - \ddot{\Omega}_3) + \dot{f}_2)] &= 0 \end{aligned}$$

$$\begin{aligned} (\partial_t \mathbf{r}_s) \cdot \mathbf{e}_2 &= 0 \\ -\Omega_1 (\dot{\tau} + a\pi(F_2 \Omega_1 \Omega_3 - \Omega_1 f_1 - \Omega_2 (F_1 \Omega_3 + f_2))) + \kappa_1 \Omega_1 (\Omega_2 \Omega_3 + \dot{\Omega}_1) + \kappa_2 \Omega_2 (\dot{\Omega}_2 - \Omega_1 \Omega_3) \\ + \frac{\xi_{\parallel}}{\xi_{\perp}} [\kappa_1 \ddot{\Omega}_1 - \tau \dot{\Omega}_1 + \Omega_3^2 (3a\pi f_1 + (2\kappa_3 - 3\kappa_1) \dot{\Omega}_1) \\ + \Omega_3 (3(\kappa_3 - \kappa_1) \Omega_1 \Omega_3 + 3a\pi(F_1 \Omega_3 + f_2) + (2\kappa_3 - 3\kappa_2) \dot{\Omega}_2) \\ - \Omega_1 (\dot{\tau} + 2a^2 \pi (2\Omega_3 \dot{f}_0 + f_0 \dot{\Omega}_3)) - 2a^2 \pi f_0 (2\Omega_3 \dot{\Omega}_1 + \ddot{\Omega}_2) + (\kappa_3 - 3\kappa_2) \Omega_3 \ddot{\Omega}_2 \\ + \Omega_2 (\tau \Omega_3 + 2a^2 \pi (f_0 \Omega_3^2 - \dot{f}_0) + (\kappa_2 - \kappa_3) (\Omega_3^3 - \dot{\Omega}_3)) \\ - a\pi(4a\dot{f}_0 \dot{\Omega}_2 - 3\Omega_3 \dot{f}_2 + F_2 (\Omega_3^3 - \ddot{\Omega}_3) + \dot{f}_1)] &= 0 \end{aligned}$$

$$\begin{aligned} (\partial_t \mathbf{r}_s) \cdot \mathbf{e}_3 &= 0 \\ \Leftrightarrow \text{Incompressibility constraint}|_{s=0} \end{aligned}$$

Note that $(\partial_t \mathbf{r}_s) \cdot \mathbf{e}_3 = 0$ is equivalent to the incompressibility constraint evaluated at $s = 0$ and therefore does not constitute an additional condition at the boundary, since it is automatically satisfied.

Two-dimensional limit

In the limit where $\kappa_2, \kappa_3, \rightarrow \infty \Rightarrow \Omega_2, \Omega_3 \rightarrow 0$ above force balance equations and incompressibility constraint reduce to

$$\begin{aligned}
\ddot{\tau} - \frac{\xi_{\parallel}}{\xi_{\perp}} \tau \Omega_1^2 &= a\pi(f_1 \dot{\Omega}_1 + \Omega_1 \dot{f}_1) - \kappa_1(\dot{\Omega}_1^2 + \Omega_1 \ddot{\Omega}_1) + \frac{\xi_{\parallel}}{\xi_{\perp}}(a\pi \Omega_1 \dot{f}_1 - \kappa_1 \Omega_1 \ddot{\Omega}_1) \\
\xi_{\perp} \partial_t \Omega_1 &= -\kappa_1 \ddot{\Omega}_1 + a\pi \ddot{f}_1 - \tau \Omega_1^3 + 2\dot{\tau} \dot{\Omega}_1 + \Omega_1 \ddot{\tau} + \tau \ddot{\Omega}_1 + \Omega_1^2(-a\pi \dot{f}_1 + \kappa_1 \ddot{\Omega}_1) \\
&\quad + \frac{\xi_{\perp}}{\xi_{\parallel}}(\dot{\tau} \dot{\Omega}_1 + \Omega_1(-3a\pi f_1 \dot{\Omega}_1 + 3\kappa_1 \dot{\Omega}_1^2 + 2\ddot{\tau} + \Omega_1(-2a\pi \dot{f}_1 + 2\kappa_1 \ddot{\Omega}_1))) \quad .
\end{aligned}$$

And the boundary conditions at the base $s = 0$ become

$$\begin{aligned}
\kappa_1 \ddot{\Omega}_1 - a\pi \dot{f}_1 - \Omega_1 \tau &= 0 \\
\kappa_1 \Omega_1 \dot{\Omega}_1 - a\pi \Omega_1 f_1 - \dot{\tau} &= 0
\end{aligned}$$

Passive limit

In the limit where there are no internal forces acting, i.e. $f_0, F_1, F_2 \rightarrow 0$ above three-dimensional equations for the active axoneme reduce to the previously discussed case for a passive filament (with $\kappa_1 = \kappa_2$) [107]. Note that in [107] the sign of the second term of Eq. (7) is incorrect and should be a minus [137].

Non-linear perturbation calculation

Multiplication of Eq. (3.15) with ψ_0^+ , and subsequent integration leads to an equation in which the only term involving ψ_1 is given by

$$\begin{aligned} \int_0^1 \psi_0^+ \mathcal{L}_c \psi_1 &= \int_0^1 \psi_0^+ (i\omega_c \psi_1 + \overset{\cdot\cdot\cdot}{\psi}_1 - \chi_c \overset{\cdot\cdot}{\psi}_1) \\ &= \int_0^1 \psi_1 (i\omega_c \psi_0^+ + \overset{\cdot\cdot\cdot}{\psi}_0^+ - \chi_c \overset{\cdot\cdot}{\psi}_0^+) \\ &\quad + \underbrace{\left[\psi_0^+ \overset{\cdot\cdot\cdot}{\psi}_1 - \overset{\cdot\cdot}{\psi}_0^+ \overset{\cdot\cdot}{\psi}_1 + (\overset{\cdot\cdot}{\psi}_0^+ - \chi_c \psi_0^+) \dot{\psi}_1 - (\overset{\cdot\cdot}{\psi}_0^+ - \chi_c \dot{\psi}_0^+) \psi_1 \right]}_{\text{B.T.}} \Big|_{s=0}^{s=1}. \end{aligned}$$

In order to eliminate ψ_1 from the above expression we require that

$$i\omega_c \psi_0^+ + \overset{\cdot\cdot\cdot}{\psi}_0^+ - \chi_c \overset{\cdot\cdot}{\psi}_0^+ = 0$$

i.e that ψ_0^+ satisfies the same differential equation as the linear modes ψ_0

$$\mathcal{L}_c \psi_0^+(s) = 0 \quad . \quad (\text{E.1})$$

The boundary conditions for ψ_0^+ are chosen such that terms proportional to ψ_1 vanish at the boundaries $s = 0$ and $s = 1$. In order to find those conditions for ψ_0^+ we first have to determine explicitly the boundary conditions for ψ_1 .

Clamped head without basal sliding

Matching terms of $\mathcal{O}(\epsilon)$ defines the linear problem

At $s = 0$	At $s = 1$
$\psi_0 = 0$	$\dot{\psi}_0 = 0$
$\overset{\cdot\cdot\cdot}{\psi}_0 - \chi_c \dot{\psi}_0 = 0$	$\overset{\cdot\cdot}{\psi}_0 - \chi_c \psi_0 = 0$

(E.2)

Matching terms of order $\mathcal{O}(\epsilon^2)$ defines the boundary conditions for τ_0 and τ_2 .

At $s = 0$	At $s = 1$	(E.3)
$\dot{\tau}_0 = -\partial_s(\dot{\psi} ^2)$	$\tau_0 = 0$	
$\dot{\tau}_2 = -\dot{\psi}\ddot{\psi}$	$\tau_2 = 0$	

And matching terms of order $\mathcal{O}(\epsilon^3)$ leads to the following boundary conditions for the non-linear correction ψ_1

At $s = 0$	At $s = 1$
$\psi_1 = 0$	$\dot{\psi}_1 = 0$
$\ddot{\psi}_1 - \chi_c \dot{\psi}_1 = A(\rho, \theta; \psi_0)$	$\ddot{\psi}_1 - \chi_c \dot{\psi}_1 = B(\rho, \theta; \psi_0)$

where

$$A(\rho, \theta; \psi_0) = \rho e^{i\theta} \dot{\psi}_0 + \tau_0 \dot{\psi}_0 + \tau_2 \dot{\psi}_0^*$$

$$B(\rho, \theta; \psi_0) = \rho e^{i\theta} \psi_0 + \chi_{nl} |\psi_0|^2 \psi_0 \quad .$$

Substituting these conditions into the boundary terms B.T. leads to

$$\int_0^1 \psi_0^+ \mathcal{L}_c \psi_1 = [\ddot{\psi}_1 \psi_0^+ - \psi_1 \ddot{\psi}_0^+ - B(\rho, \theta; \psi_0) \dot{\psi}_0^+]_{s=1} - [-\ddot{\psi}_1 \dot{\psi}_0^+ + \dot{\psi}_1 \ddot{\psi}_0^+ + A(\rho, \theta; \psi_0) \psi_0^+]_{s=0}$$

which become independent ψ_1 if ψ_0^+ satisfies the following conditions

At $s = 0$	At $s = 1$	(E.4)
$\dot{\psi}_0^+ = 0$	$\dot{\psi}_0^+ = 0$	
$\ddot{\psi}_0^+ = 0$	$\ddot{\psi}_0^+ = 0$	

Hence if ψ_0^+ satisfies Eq. (E.1) with boundary conditions (E.4) we finally obtain following expression for the last term

$$\begin{aligned} \int_0^1 \psi_0^+ \mathcal{L}_c \psi_1 &= -A(\rho, \theta; \psi_0) \psi_0^+ - B(\rho, \theta; \psi_0) \dot{\psi}_0^+ \\ &\equiv Z(\rho, \theta, \mu; \psi_0, \psi_0^+, \tau_0, \tau_2) \end{aligned}$$

In contrast to the other more complicated cases, for the clamped head without basal sliding discussion it is still feasible to write the complete expression that determines the relation between the three quantities ρ, θ, μ . We have

$$\begin{aligned} 0 &= -\rho e^{i\theta} \int_0^1 \psi_0^+ \partial_s^2 \psi_0 + i\mu \int_0^1 \psi_0^+ \psi_0 + \int_0^1 \psi_0^+ \mathcal{N}(\psi_0^3) \\ &\quad - \rho e^{i\theta} \psi_0^+(0) \dot{\psi}_0(0) - \left[\psi_0^+ (\tau_0 \dot{\psi}_0 + \tau_2 \dot{\psi}_0^*) \right]_{s=0} - \rho e^{i\theta} \dot{\psi}_0^+(1) \psi_0(1) - \left[\dot{\psi}_0^+ \chi_{nl} |\psi_0|^2 \psi_0 \right]_{s=1} \\ \rho e^{i\theta} &= \frac{i\mu \int_0^1 \psi_0^+ \psi_0 + \int_0^1 \psi_0^+ \mathcal{N}_1(\psi_0^3) - \left[\psi_0^+ (\tau_0 \dot{\psi}_0 + \tau_2 \dot{\psi}_0^*) \right]_{s=0} - \left[\dot{\psi}_0^+ \chi_{nl} |\psi_0|^2 \psi_0 \right]_{s=1}}{\int_0^1 \psi_0^+ \partial_s^2 \psi_0 + \psi_0^+(0) \dot{\psi}_0(0) + \dot{\psi}_0^+(1) \psi_0(1)} \end{aligned}$$

Clamped head with basal sliding

Matching terms of order $\mathcal{O}(\epsilon)$ defines the linear problem

At $s = 0$	At $s = 1$
$\psi_0 = 0$	$\dot{\psi}_0 = 0$
$\ddot{\psi}_0 - \chi_c \dot{\psi}_0 = 0$	$\ddot{\psi}_0 - \chi_c(\psi_0 + \Delta_0^0) = 0$

(E.5)

where we have introduced

$$\Delta_0^0 = -\frac{\bar{\chi}_c}{i\bar{\omega}_c\bar{\gamma} + \bar{k} + \bar{\chi}_c} \int_0^1 \psi_0(s) ds$$

Matching terms of order $\mathcal{O}(\epsilon^2)$ defines the τ_0, τ_2 conditions

At $s = 0$	At $s = 1$
$\dot{\tau}_0 = -\partial_s(\dot{\psi} ^2) + 2\text{Re}\left\{\bar{\chi}_c\Delta_0^0\dot{\psi}^*\right\}$	$\tau_0 = 0$
$\dot{\tau}_2 = -\dot{\psi}\ddot{\psi} + \bar{\chi}_c\Delta_0^0\dot{\psi}$	$\tau_2 = 0$

(E.6)

Matching terms of order $\mathcal{O}(\epsilon^3)$ defines the non-linear correction. But before we can write down the result we must first of all note that the parameters $\Delta_0^{lin}, \Delta_0^{nl}$ themselves need to be expanded in orders of ϵ as we go away from the bifurcation.

$$\begin{aligned} \Delta_0^{lin} &= -\epsilon \frac{\bar{\chi}_c}{i\bar{\omega}_c\bar{\gamma} + \bar{k} + \bar{\chi}_c} \int_0^1 \psi_0(s) ds - \epsilon^3 \frac{\rho e^{i\theta}(i\bar{\omega}_c\bar{\gamma} + \bar{k}) - i\mu\bar{\gamma}\bar{\chi}_c}{(i\bar{\omega}_c\bar{\gamma} + \bar{k} + \bar{\chi}_c)^2} \int_0^1 \psi_0(s) ds \\ &\quad - \epsilon^3 \frac{\bar{\chi}_c}{i\bar{\omega}_c\bar{\gamma} + \bar{k} + \bar{\chi}_c} \int_0^1 \psi_1(s) ds \\ &= \epsilon \Delta_0^0 + \epsilon^3 \left(\frac{\Delta_0^0}{\bar{\chi}_c} \frac{\rho e^{i\theta}(i\bar{\omega}_c\bar{\gamma} + \bar{k}) - i\mu\bar{\gamma}\bar{\chi}_c}{i\bar{\omega}_c\bar{\gamma} + \bar{k} + \bar{\chi}_c} + \Delta_0^1 \right) \\ \Delta_0^{nl} &= \Delta_0^{lin} - \epsilon^3 \frac{\bar{\chi}_c^{nl}}{i\bar{\omega}_c\bar{\gamma} + \bar{k} + \bar{\chi}_c} \int_0^1 |\psi_0(s) + \Delta_0^0|^2 (\psi_0(s) + \Delta_0^0) ds \end{aligned}$$

where we have introduced

$$\Delta_0^1 = -\frac{\bar{\chi}_c}{i\bar{\omega}_c\bar{\gamma} + \bar{k} + \bar{\chi}_c} \int_0^1 \psi_1(s) ds \quad .$$

The notation with $\Delta_0^{lin}, \Delta_0^{nl}, \Delta_0^0, \Delta_0^1$ seems cumbersome, but it is necessary to rigorously keep track of the correct orders of ψ at all stages. So, armed with the above we can finally match all $\mathcal{O}(\epsilon^3)$ terms to obtain the following expression for the boundary conditions of ψ_1

At $s = 0$	At $s = 1$
$\psi_1 = 0$	$\dot{\psi}_1 = 0$
$\ddot{\psi}_1 - \bar{\chi}_c \dot{\psi}_1 = A(\rho, \theta; \psi_0)$	$\ddot{\psi}_1 - \bar{\chi}_c(\psi_1 + \Delta_0^1) = B(\rho, \theta; \psi_0)$

where

$$\begin{aligned} A(\rho, \theta; \psi_0) &= \rho e^{i\theta} \dot{\psi}_0 + \bar{\chi}_c^{nl} (2|\Delta_0^0|^2 \dot{\psi}_0 + (\Delta_0^0)^2 \dot{\psi}_0^*) + \tau_0 \dot{\psi}_0 + \tau_2 \dot{\psi}_0^* \\ B(\rho, \theta; \psi_0) &= \rho e^{i\theta} (\psi_0 + \Delta_0^0) + \bar{\chi}_c^{nl} |\psi_0 + \Delta_0^0|^2 \psi_0 \\ &\quad + \frac{1}{i\bar{\omega}_c\bar{\gamma} + \bar{k} + \bar{\chi}_c} (\Delta_0^0 (\rho e^{i\theta}(i\bar{\omega}_c\bar{\gamma} + \bar{k}) - i\mu\bar{\gamma}\bar{\chi}_c) - \bar{\chi}_c^{nl} \bar{\chi}_c) \int_0^1 |\psi_0(s) + \Delta_0^0|^2 (\psi_0(s) + \Delta_0^0) ds \end{aligned}$$

Note that the above form of the boundary conditions contains Δ_0^1 which is defined in terms of the integral over ψ_1 . Hence in order to substitute the conditions on ψ_1 into the boundary terms we need to eliminate this integral. We do this by making use of Eq. (3.15)

$$\begin{aligned}\psi_1 &= \frac{1}{i\omega_c}[-\ddot{\psi}_1 + \chi_c\ddot{\psi}_1 + \rho e^{i\theta}\ddot{\psi}_0 - i\mu\psi_0 - \mathcal{N}_1(|\psi_0|^2\psi_0)] \\ \Rightarrow \int_0^1 \psi_1(s)ds &= \frac{1}{i\omega_c}[-\ddot{\psi}_1(1) + \ddot{\psi}_1(0) + \chi_c(\dot{\psi}_1(1) - \dot{\psi}_1(0)) + \rho e^{i\theta}(\dot{\psi}_0(1) - \dot{\psi}_0(0)) \\ &\quad - i\mu \int_0^1 \psi_0(s)ds - \int_0^1 \mathcal{N}_1(|\psi_0(s)|^2\psi_0(s))ds] \quad ,\end{aligned}$$

which can be simplified using the other boundary conditions, namely $\dot{\psi}_1(1) = 0$, $\ddot{\psi}_1 - \bar{\chi}_c\dot{\psi}_1 = A(\rho, \theta; \psi_0)$ and $\int_0^1 \psi_0(s)ds = -\frac{\Delta_0^{lin}}{\bar{\chi}_c}(i\bar{\omega}\bar{\gamma} + \bar{k} + \bar{\chi}_c)$ leading to

$$\int_0^1 \psi_1(s)ds = \frac{1}{i\bar{\omega}_c}[-\ddot{\psi}_1(1) + A(\rho, \theta; \psi_0) - \rho e^{i\theta}\dot{\psi}_0(0) + i\mu\frac{\Delta_0^0}{\bar{\chi}_c}(i\bar{\omega}_c\bar{\gamma} + \bar{k} + \bar{\chi}_c) - \int_0^1 \mathcal{N}_1(|\psi_0(s)|^2\psi_0(s))ds] \quad .$$

Hence the boundary conditions, which we can substitute into the boundary terms B.T., are given by

At $s = 0$	At $s = 1$
$\psi_1 = 0$	$\dot{\psi}_1 = 0$
$\ddot{\psi}_1 = \bar{\chi}_c\dot{\psi}_1 + A(\rho, \theta; \psi_0)$	$\ddot{\psi}_1 = \bar{\chi}_c(\psi_1 + \frac{\bar{\chi}_c}{i\bar{\omega}_c\bar{\gamma} + \bar{k} + \bar{\chi}_c}\frac{1}{i\bar{\omega}_c}\ddot{\psi}_1) + B'(\rho, \theta, \mu; \psi_0)$

where

$$B''(\rho, \theta, \mu; \psi_0) = B(\rho, \theta; \psi_0) - \frac{\mu\Delta_0^0}{\bar{\omega}_c}\bar{\chi}_c + \frac{\bar{\chi}_c^2}{i\bar{\omega}_c\bar{\gamma} + \bar{k} + \bar{\chi}_c}\frac{1}{i\bar{\omega}_c}(\rho e^{i\theta}\dot{\psi}_0(0) - A(\rho, \theta; \psi_0) + \int_0^1 \mathcal{N}_1(|\psi_0(s)|^2\psi_0(s))ds) \quad .$$

Substitution of this expression into the boundary terms B.T. and subsequent re-ordering leads to

$$\begin{aligned}\text{B.T.} &= \ddot{\psi}_1(1)(\psi_0^+(1) - \psi_0^+(1)\frac{\bar{\chi}_c^2}{i\bar{\omega}_c(i\bar{\omega}_c\bar{\gamma} + \bar{k} + \bar{\chi}_c)}) - \psi_1(1)\ddot{\psi}_0^+(1) - \dot{\psi}_1(0)\ddot{\psi}_0^+(0) + \ddot{\psi}_1(0)\dot{\psi}_0^+(0) \\ &\quad - \psi_0^+(0)A(\rho, \theta; \psi_0) - \dot{\psi}_0^+(1)B'(\rho, \theta, \mu; \psi_0) \quad .\end{aligned}$$

Hence we impose following boundary conditions on the conjugated modes

At $s = 0$	At $s = 1$
$\dot{\psi}_0^+ = 0$	$\psi_0^+ = \dot{\psi}_0^+(1)\frac{\bar{\chi}_c^2}{i\bar{\omega}_c(i\bar{\omega}_c\bar{\gamma} + \bar{k} + \bar{\chi}_c)}$
$\ddot{\psi}_0^+ = 0$	$\ddot{\psi}_0^+ = 0$

(E.7)

If ψ_0^+ satisfies Eq. (E.1) with boundary conditions (E.7) we finally obtain the following expression for the last term

$$\begin{aligned}\int_0^1 \psi_0^+ \mathcal{L}_c \psi_1 &= -\psi_0^+(0)A(\rho, \theta; \psi_0) - \dot{\psi}_0^+(1)B'(\rho, \theta, \mu; \psi_0) \\ &\equiv Z(\rho, \theta, \mu; \psi_0, \psi_0^+, \tau_0, \tau_2) \quad .\end{aligned}$$

Freely pivoting head

Matching terms of order $\mathcal{O}(\epsilon)$ defines the following linear problem

$$\begin{aligned} \ddot{\psi}_0(0) - \bar{\chi}_c \dot{\psi}_0(0) &= 0 & \ddot{\psi}_0(1) - \bar{\chi}_c(\psi_0(1) - \psi_0(0)) &= 0 \\ \dot{\psi}_0(0) + \bar{\chi}_c[-\psi_0(0) + \int_0^1 \psi_0(s) ds] &= 0 & \dot{\psi}_0(1) &= 0 \end{aligned} \quad (\text{E.8})$$

Matching terms of order $\mathcal{O}(\epsilon^2)$ defines the usual boundary conditions for τ_0 and τ_2 .

At $s = 0$	At $s = 1$
$\dot{\tau}_0 = -\partial_s(\dot{\psi} ^2)$	$\tau_0 = 0$
$\dot{\tau}_2 = -\dot{\psi}\ddot{\psi}$	$\tau_2 = 0$

(E.9)

which together with the differential equations for $\tau_{0,2}$ as given in section 3.2 fully defines $\tau_{0,2}$ in terms of ψ_0 .

Matching terms of order $\mathcal{O}(\epsilon^3)$ gives rise to

$$\begin{aligned} \ddot{\psi}_1(0) - \bar{\chi}_c \dot{\psi}_1(0) &= A(\rho, \theta; \psi_0) & \ddot{\psi}_1(1) - \bar{\chi}_c(\psi_1(1) - \psi_1(0)) &= B(\rho, \theta; \psi_0) \\ \dot{\psi}_1(0) + \bar{\chi}_c[-\psi_1(0) + \underbrace{\int_0^1 \psi_1(s) ds}_I] &= C(\rho, \theta; \psi_0) & \dot{\psi}_1(1) &= 0 \end{aligned}$$

where

$$\begin{aligned} A(\rho, \theta; \psi_0) &= \rho e^{i\theta} \dot{\psi}_0(0) + \tau_0(0) \dot{\psi}_0(0) + \tau_2(0) \dot{\psi}_0^*(0) \\ B(\rho, \theta; \psi_0) &= \rho e^{i\theta} (\psi_0(1) - \psi_0(0)) + \bar{\chi}_{nl} |\psi_0(1) - \psi_0(0)|^2 (\psi_0(1) - \psi_0(0)) \\ C(\rho, \theta; \psi_0) &= -\rho e^{i\theta} [-\psi_0(0) + \int_0^1 \psi_0(s) ds] - \bar{\chi}_{nl} \int_0^1 [|\psi_0(s) - \psi_0(0)|^2 (\psi_0(s) - \psi_0(0))] ds \quad . \end{aligned}$$

We can simplify the last two terms, making use of the ψ_0 conditions.

$$\begin{aligned} \Rightarrow B(\rho, \theta; \psi_0) &= \frac{\rho e^{i\theta}}{\bar{\chi}_c} \ddot{\psi}_0(1) + \frac{1}{|\bar{\chi}_c|^2} \frac{\bar{\chi}_{nl}}{\bar{\chi}_c} \left| \ddot{\psi}_0(1) \right|^2 \ddot{\psi}_0(1) \\ \Rightarrow C(\rho, \theta; \psi_0) &= \frac{\rho e^{i\theta}}{\bar{\chi}_c} \dot{\psi}_0(0) - \bar{\chi}_{nl} \int_0^1 [|\psi_0(s) - \psi_0(0)|^2 (\psi_0(s) - \psi_0(0))] ds \quad . \end{aligned}$$

In order to get these conditions for ψ_1 in a form we can substitute back into the boundary terms we need to eliminate the integral I , which we do by making use of Eq. (3.15)

$$\begin{aligned} \psi_1 &= \frac{1}{i\bar{\omega}_c} [-\ddot{\psi}_1 + \bar{\chi}_c \ddot{\psi}_1 + \rho e^{i\theta} \ddot{\psi}_0 - i\mu\psi_0 - \mathcal{N}_1(|\psi_0|^2\psi_0)] \\ \Rightarrow I &= \frac{1}{i\bar{\omega}_c} [-\ddot{\psi}_1(1) + \ddot{\psi}_1(0) - \bar{\chi}_c \dot{\psi}_1(0) - \rho e^{i\theta} \dot{\psi}_0(0) - i\mu(-\frac{1}{\bar{\chi}_c} \dot{\psi}_0(0) + \psi_0(0)) - \int_0^1 \mathcal{N}_1(|\psi_0|^2\psi_0) ds] \quad , \end{aligned}$$

where we have made use of some of the other boundary conditions. Finally, we can rewrite the condition involving I as follows

$$\dot{\psi}_1(0) + \bar{\chi}_c \left\{ -\psi_1(0) + \frac{1}{i\bar{\omega}_c} [-\ddot{\psi}_1(1) + A(\rho, \theta; \psi_0)] \right\} = C'(\rho, \theta; \psi_0) \quad ,$$

where

$$C'(\rho, \theta; \psi_0) = C(\rho, \theta; \psi_0) + \frac{\bar{\chi}_c}{i\omega_c} [\rho e^{i\theta} \dot{\psi}_0(0) + i\mu(\psi_0(0) - \frac{1}{\bar{\chi}_c} \dot{\psi}_0(0))] + \int_0^1 \mathcal{N}(|\psi_0|^2 \psi_0) ds$$

For clarity, let's finally group the boundary conditions for ψ_1 together into one table

$$\begin{aligned} \dot{\psi}_1(1) &= 0 \\ \ddot{\psi}_1(0) - \chi_c \dot{\psi}_1(0) &= A(\rho, \theta; \psi_0) \\ \ddot{\psi}_1(1) - \chi_c [\psi_1(1) - \psi_1(0)] &= B(\rho, \theta; \psi_0) \\ \dot{\psi}_1(0) + \chi_c [-\psi_1(0) + \frac{1}{i\omega_c} (-\ddot{\psi}_1(1) + A)] &= C'(\rho, \theta; \psi_0) \end{aligned}$$

defining four equations relating the eight quantities $\psi_1(0)$, $\dot{\psi}_1(0)$, $\ddot{\psi}_1(0)$, $\ddot{\psi}_1(1)$, $\psi_1(1)$, $\dot{\psi}_1(1)$, $\ddot{\psi}_1(1)$, $\ddot{\psi}_1(1)$. This enables us to express four of them in terms of four others. In matrix form we can write this system of equation as

$$\begin{pmatrix} 1 & 0 & 0 & 0 \\ 0 & 1 & -\chi_c & 0 \\ 0 & 0 & 1 & 0 \\ 0 & 0 & 0 & 1 \end{pmatrix} \begin{pmatrix} \dot{\psi}_1(1) \\ \ddot{\psi}_1(0) \\ \dot{\psi}_1(0) \\ \ddot{\psi}_1(1) \end{pmatrix} = \begin{pmatrix} 0 \\ A \\ C' - \chi_c [-\psi_1(0) + \frac{1}{i\omega_c} (-\ddot{\psi}_1(1) + A)] \\ B + \chi_c [\psi_1(1) - \psi_1(0)] \end{pmatrix}$$

which we can be solved easily

$$\begin{aligned} \dot{\psi}_1(1) &= 0 \\ \ddot{\psi}_1(0) &= A(\rho, \theta; \psi_0) + \bar{\chi}_c \{ C' - \bar{\chi}_c [-\psi_1(0) + \frac{1}{i\omega_c} (-\ddot{\psi}_1(1) + A(\rho, \theta; \psi_0))] \} \\ \dot{\psi}_1(0) &= C'(\rho, \theta; \psi_0) - \bar{\chi}_c [-\psi_1(0) + \frac{1}{i\omega_c} (-\ddot{\psi}_1(1) + A(\rho, \theta; \psi_0))] \\ \ddot{\psi}_1(1) &= B(\rho, \theta; \psi_0) + \bar{\chi}_c [\psi_1(1) - \psi_1(0)] \end{aligned}$$

Above is the desired expression for ψ_1 at the boundary, that in turn can now be substituted back into the equation for the boundary terms from the partial integration, leading to

$$\begin{aligned} \text{B.T.} &= \psi_1(0) [\ddot{\psi}_0^+(0) - \chi_c (\dot{\psi}_0^+(0) + \ddot{\psi}_0^+(0) - \dot{\psi}_0^+(1))] + \ddot{\psi}_1(0) \dot{\psi}_0^+(0) \\ &\quad - \psi_1(1) \ddot{\psi}_0^+(1) + \ddot{\psi}_1(1) [i \frac{\chi_c}{\omega_c} \ddot{\psi}_0^+(0) + \dot{\psi}_0^+(1)] - A(\dot{\psi}_0^+(0) + i \frac{\chi_c}{\omega_c} \ddot{\psi}_0^+(0)) - B \dot{\psi}_0^+(1) - C' \ddot{\psi}_0^+(0) \quad . \end{aligned}$$

Hence in order to eliminate the ψ_1 dependence from the above expression we impose the following boundary conditions for the conjugated linear modes ψ_0^+

$$\begin{aligned} \dot{\psi}_0^+(0) &= 0 \\ \ddot{\psi}_0^+(1) &= 0 \\ \psi_0^+(1) + i \frac{\chi_c}{\omega_c} \ddot{\psi}_0^+(0) &= 0 \\ \ddot{\psi}_0^+(0) - \chi_c (\dot{\psi}_0^+(0) + \ddot{\psi}_0^+(0) - \dot{\psi}_0^+(1)) &= 0 \end{aligned} \tag{E.10}$$

Note that the matrix defining these boundary conditions for the conjugated mode is singular for the same values χ_c as the matrix defining the boundary conditions of the linear problem, as is expected.

Hence if ψ_0^+ satisfies Eq. (E.1) with boundary conditions (E.10) we finally obtain the following expression for the last term in Eq. (3.16)

$$\begin{aligned} \int_0^1 \psi_0^+ \mathcal{L}_c \psi_1 &= -A(\rho, \theta; \psi_0)(\psi_0^+(0) + i \frac{\chi_c}{\omega_c} \ddot{\psi}_0^+(0)) - B(\rho, \theta; \psi_0) \dot{\psi}_0^+(1) - C'(\rho, \theta; \psi_0) \ddot{\psi}_0^+(0) \\ &\equiv Z(\rho, \theta; \psi_0, \psi_0^+, \tau_0, \tau_2) \quad . \end{aligned}$$

Limiting behaviour

In order to check the self-consistency of this approach (and that no mistakes were made during these rather involved calculations) we examined the limiting behaviour of the above expressions for the clamped head case, namely what happens when we try to find an expression for ρ and μ as the direction of $\Delta\chi$ becomes tangential to the critical line $\chi_c(\omega)$. In that case ϵ will tend to zero, while $\Delta\chi$ and $\Delta\omega$ remain finite, from which we conclude that ρ and μ must diverge for our ansatz (3.9) to be self-consistent. Hence in the limit $\rho, \mu \rightarrow \infty$ Eq. (3.16) determines the direction $e^{i\theta}$ that is tangential to the critical line. Using numerical results we verified this fact graphically (not shown).

Complete experimental dataset with theoretical fits

Here we present the best fit parameters and solutions for six different data sets from bull sperm, that were attached to the cover slip by their head, beating with similar frequency.

Sperm	$\frac{\omega}{2\pi}$ (in Hz)	k_s (in $\frac{pN}{nm}$)	γ (in $\frac{pNs}{nm}$)	Δ_0 (in μm)
Ko1/	19.80	83.31	0.27832	0.1676
R4/	21.26	87.63	0.29165	0.1752
S5/	20.28	84.84	0.28329	0.1649
T1/	22.70	90.28	0.28627	0.2162
T4/	19.55	83.08	0.28230	0.1690
V2/	20.30	85.61	0.29281	0.1875
Average	20.6	85.8	0.2857	0.180
S.D.	1.2	2.8	0.0056	0.019

(F.1)

The corresponding fits, where the amplitude of the solution has been fixed to match the amplitude of the experiment, are shown in Figs. F.1 – F.3.

Note that the theoretical solution tends to deviate from the experimental curve towards the distal end at $s = 1$, which is probably due to an image sampling effect, since the distal end of the sperm flagellum cannot be detected exactly. Hence in general the experimental data are missing the very end of the flagellum, which we believe leads to the above effect.

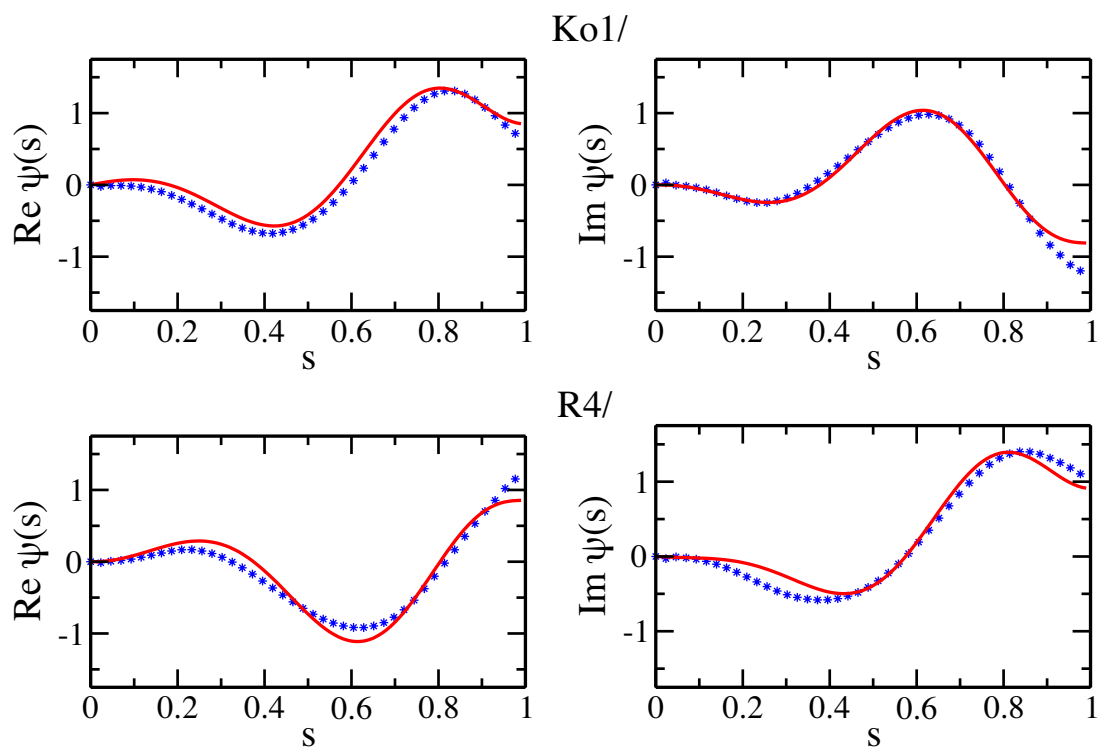


Figure F.1: The best fits for sperm Ko1, R4.

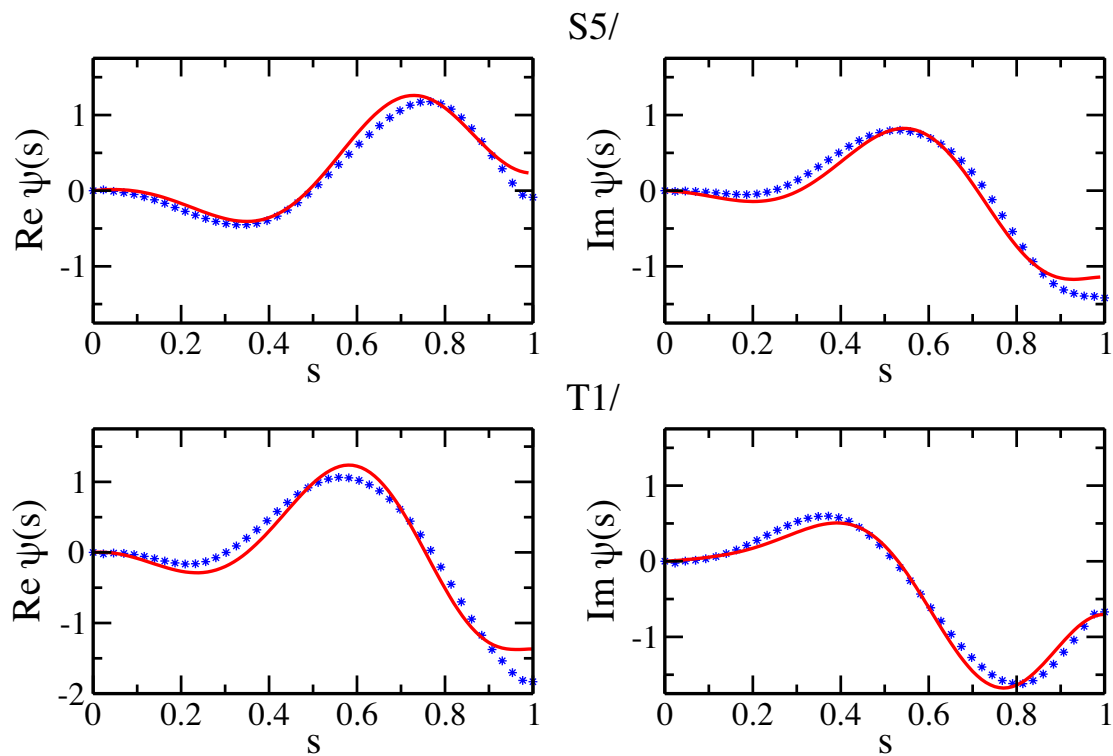


Figure F.2: The best fits for sperm S5, T1

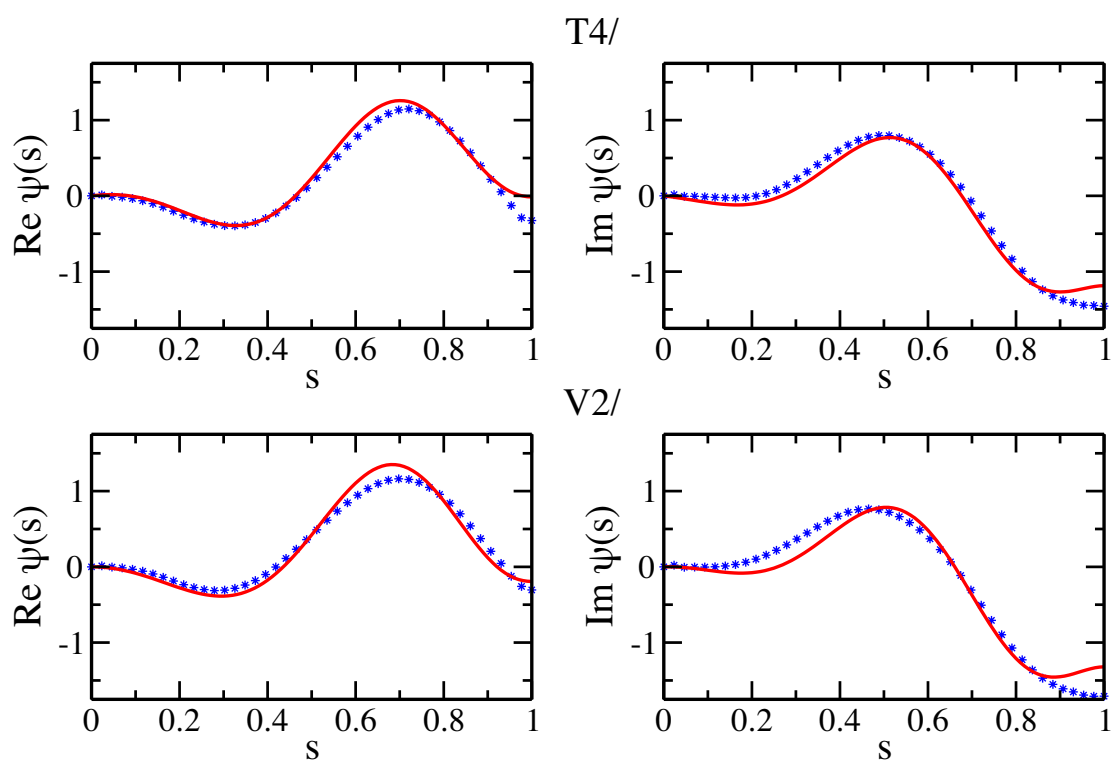


Figure F.3: The best fits for sperm T4,V2.

Unstable modes for microscopic motor models

For the parameter values of the microscopic motor response as discussed in section 4.2 the system becomes unstable with different modes and frequencies as the control parameter Ω is increased. In this appendix we present the first six unstable modes, comparing basal sliding (left hand side, $k_s = 85.8 \frac{\text{pN}}{\text{nm}}$ $\gamma = 0.286 \frac{\text{pNs}}{\text{nm}}$) to fixed basal connection (right hand side, $k_s \rightarrow \infty$). Plotted are the arbitrarily normalised real and imaginary parts of the first Fourier mode of the shear angle $\psi(s)$, and the corresponding critical value Ω_c of the order parameter for which the system becomes unstable with that particular mode and frequency ω_c .

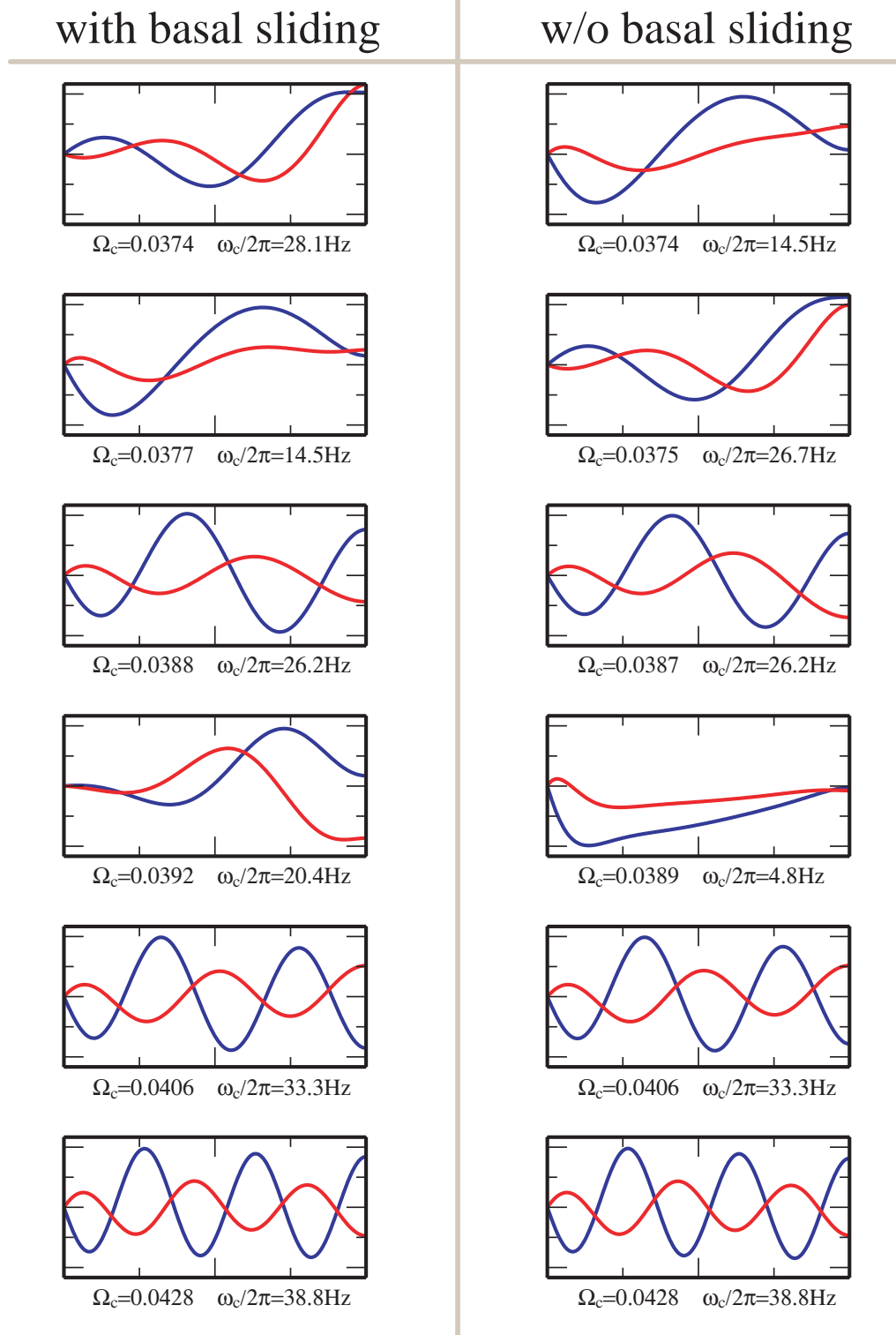


Figure G.1

Boundary condition defining matrices

Here we define the matrices $\mathbf{Q}^{(1)}(\bar{\chi}, \bar{\omega})$ and $\mathbf{Q}^{(2)}(\bar{\chi}, \bar{\omega})$, and in the limit $\omega \rightarrow 0$ also find an analytic expression for the values of χ such that which $\det \mathbf{Q}^{(i)} = 0$.

General case $\omega \neq 0$

Let $\mathbf{Q}^{(1)} = Q_{mn}^{(1)}$ and $\mathbf{Q}^{(2)} = Q_{mn}^{(2)}$, where

$$\begin{aligned} Q_{1,n}^{(1)} &= \bar{\chi} - q_n^2 + 2Aiq_n \\ Q_{2,n}^{(1)} &= \bar{\chi}q_n - q_n^3 + 3Ai(q_n^2 - \bar{\chi}) \\ Q_{3,n}^{(1)} &= e^{q_n} \\ Q_{4,n}^{(1)} &= \frac{\bar{\chi}}{q_n}(e^{q_n} - 1) - q_n e^{q_n} + Aie^{q_n} \end{aligned}$$

$$\begin{aligned} Q_{1,n}^{(2)} &= \bar{\chi} - q_n^2 + 2Aiq_n \\ Q_{2,n}^{(2)} &= \bar{\chi}q_n - q_n^3 + 3Ai(q_n^2 - \bar{\chi}) \\ Q_{3,n}^{(2)} &= e^{-q_n} \\ Q_{4,n}^{(2)} &= \frac{\bar{\chi}}{q_n}(e^{-q_n} - 1) - q_n e^{-q_n} + Aie^{-q_n} \end{aligned}$$

Limiting case $\omega \rightarrow 0$

Note that in the limit $\omega \rightarrow 0$ the general solution is of a different form from the $\omega \neq 0$ case, and given by

$$\mathbf{z}(s) = \sum_{n=1}^{n=3} (C_n \mathbf{z}_1 e^{q_n s} + C_4) + \mathbf{z}(s) = \sum_{n=1}^{n=3} (D_n \mathbf{z}_2 e^{-q_n s} + D_4) \quad .$$

The corresponding matrices that characterise the boundary conditions are therefore different from the above. They can be determined in the same straightforward manner and lead to the result that

$$\det \mathbf{Q}^{(1)}(\bar{\chi}), \det \mathbf{Q}^{(2)}(\bar{\chi}) \sim e^{-\sqrt{\bar{\chi}}}(1 + e^{2\sqrt{\bar{\chi}}})\bar{\chi}^{\frac{3}{2}}(16A^2 + \bar{\chi}) \quad .$$

In contrast to the $\omega \neq 0$ case, the set of solutions to this equation can be solved analytically with non-trivial zeroes for

$$\begin{aligned} 1 + e^{2\sqrt{\bar{\chi}}} &= 0 \\ \Rightarrow \bar{\chi}_n &= -\left(\frac{2n+1}{2}\pi\right)^2 \text{ for } n = 0, 1, 2, \dots \end{aligned}$$

Which define same set of zeroes on the real axis as in the previously discussed planar case [106]. Note that above equation also allows for a $\bar{\chi} = -16A^2$ solution, which is the starting point of branches for which formally $\det \mathbf{Q}^{(i)}(\bar{\chi}) = 0$ is satisfied, but whose critical values for $\bar{\chi}$ correspond to a singular limit of the problem in which $\mathbf{Q}^{(i)}$ of the above form do no longer describe the boundary conditions appropriately. This is similar to the two-dimensional case in which the branch $\bar{\chi} = \sqrt{\bar{\omega}}(1 + i)$ formally solves the eigenvalue problem of the boundary conditions, but does not allow for non-zero solutions.

Bibliography

1. M.G. Nielsen and E.C. Raff. The best of all worlds or the best possible world? Developmental constraint in the evolution of beta-tubulin and the sperm tail axoneme. *Evolution & Development*, 4(4):303–15, 2002.
2. S. Nonaka et al. Randomization of left-right asymmetry due to loss of nodal cilia generating leftward flow of extraembryonic fluid in mice lacking KIF3B motor protein. *Cell*, 95(6):829, 1998.
3. Y. Okada et al. Mechanism of nodal flow: A conserved symmetry breaking event in left-right axis determination. *Cell*, 121(4):633, 2005.
4. B.A. Afzelius. Human syndrome caused by immotile cilia. *Science*, 193(4250):317–9, 1976.
5. Dennis Kunkel Microscopy, Inc. <http://www.denniskunkel.com/>.
6. M.R. Knowles and R.C. Boucher. Mucus clearance as a primary innate defense mechanism for mammalian airways. *J Clin Invest*, 109(5):571–7, 2002.
7. Primary Ciliary Dyskinesia Interest Group <http://www.p-c-d.org>.
8. M. Mercola. Left-right asymmetry: Nodal points. *J Cell Sci*, 116(16):3251–7, 2003.
9. H.C. Berg. *E. Coli in Motion*. Biological and Medical Physics, Biomedical Engineering. Springer, New York, 2004.
10. C.H. Wiggins et al. Trapping and wiggling: Elastohydrodynamics of driven microfilaments. *Biophys J*, 74(2):1043–60, 1998.
11. C.W. Wolgemuth, T.R. Powers, and R.E. Goldstein. Twirling and whirling: Viscous dynamics of rotating elastic filaments. *Phys Rev Lett*, 84(7):1623–6, 2000.
12. B. Alberts et al. *Molecular Biology of the Cell*. Garland Science, New York, 4th edition, 2002.
13. J. Howard. *Mechanics of Motor Proteins and the Cytoskeleton*. Sinauer Associates, Publishers, Sunderland, Mass., 2001.

14. G.M. Cooper. *The Cell: A Molecular Approach*. ASM Press; Sinauer Associates, Washington, D.C. Sunderland, Mass., 2nd edition, 2000.
15. D.L. Coy, M. Wagenbach, and J. Howard. Kinesin takes one 8-nm step for each ATP that it hydrolyzes. *J Biol Chem*, 274(6):3667–71, 1999.
16. W.O. Hancock and J. Howard. Kinesin's processivity results from mechanical and chemical coordination between the ATP hydrolysis cycles of the two motor domains. *Proc Natl Acad Sci U S A*, 96(23):13147–52, 1999.
17. B. Rothlein. Kollektivarbeit im Nanokosmos. *MaxPlanckForschung*, 03:28–31, 2004.
18. J. Howard, A.J. Hudspeth, and R.D. Vale. Movement of microtubules by single kinesin molecules. *Nature*, 342(6246):154–8, 1989.
19. S. Ray et al. Kinesin follows the microtubule's protofilament axis. *J Cell Biol*, 121(5):1083–93, 1993.
20. I.R. Gibbons and A.J. Rowe. Dynein - a protein with adenosine triphosphatase activity from cilia. *Science*, 149(3682):424–&, 1965.
21. S.A. Burgess et al. Dynein structure and power stroke. *Nature*, 421(6924):715, 2003.
22. B.A. Afzelius et al. Flagellar structure in normal human spermatozoa and in spermatozoa that lack dynein arms. *Tissue & Cell*, 27(3):241–7, 1995.
23. B.A. Afzelius. Immotile cilia syndrome: Past, present, and prospects for the future. *Thorax*, 53(10):894–7, 1998.
24. Max-Planck-Institut für Physik komplexer Systeme, Institutsbroschüre. 2005.
25. B.A. Afzelius. Asymmetry of cilia and of mice and men. *Int J Dev Biol*, 43(4):283–6, 1999.
26. R.N. Seetharam and P. Satir. High speed sliding of axonemal microtubules produced by outer arm dynein. *Cell Motil Cytoskeleton*, 60(2):96–103, 2005.
27. S.K. Dutcher. Elucidation of basal body and centriole functions in *Chlamydomonas reinhardtii*. *Traffic*, 4(7):443–51, 2003.
28. G.G. Vernon and D.M. Woolley. Basal sliding and the mechanics of oscillation in a mammalian sperm flagellum. *Biophys J*, 87(6):3934–44, 2004.
29. S.J. Ansley et al. Basal body dysfunction is a likely cause of pleiotropic Bardet-Biedl syndrome. *Nature*, 425(6958):628–33, 2003.
30. I. Riedel. *Mechanics of the Axoneme: Self-Organized Beating Patterns and Vortex Arrays of Spermatozoa*. PhD thesis, TU Dresden, 2005.
31. G.J. Douglas and M.E. Holwill. Behaviour of flagella isolated from *Crithidia oncopelti*. *J Mechanochem Cell Motil*, 1(4):213–23, 1972.

32. D.M. Woolley and G.G. Vernon. A study of helical and planar waves on sea urchin sperm flagella, with a theory of how they are generated. *J Exp Biol*, 204(7):1333–45, 2001.
33. J. Cosson et al. Flagellar movements and controlling apparatus in flagellates. *Cr Rev Plant Sci*, 20(4):297–308, 2001.
34. G. Lefevre Jr. and U.B. Jonsson. Sperm transfer, storage, displacement, and utilization in *Drosophila melanogaster*. *Genetics*, 47(12):1719–36, 1962.
35. D.M. Woolley. Studies on the eel sperm flagellum: I. The structure of the inner dynein arm complex. *J Cell Sci*, 110 (Pt 1):85–94, 1997.
36. S. Ishijima, K. Sekiguchi, and Y. Hiramoto. Comparative study of the beat patterns of American and Asian horseshoe crab sperm: Evidence for a role of the central pair complex in forming planar waveforms in flagella. *Cell Motil Cytoskel*, 9(3):264–70, 1988.
37. B.H. Gibbons, B. Baccetti, and I.R. Gibbons. Live and reactivated motility in the 9 + 0 flagellum of *anguilla* sperm. *Cell Motil Cytoskel*, 5(4):333–50, 1985.
38. J. Schrevel and C. Besse. Un type flagellaire fonctionnel de base "6 + 0". *J Cell Biol*, 66(3):492–507, 1975.
39. G. Prensier et al. Motile flagellum with a "3 + 0" ultrastructure. *Science*, 207(4438):1493–4, 1980.
40. S.F. Goldstein and J. Schrevel. Motility of the 6 + 0 flagellum of *Lecudina tuzetae*. *Cell Motil Cytoskel*, 2(4):369–83, 1982.
41. G.B. Witman, J. Plummer, and G. Sander. *Chlamydomonas* flagellar mutants lacking radial spokes and central tubules. Structure, composition, and function of specific axonemal components. *J Cell Biol*, 76(3):729–47, 1978.
42. B. Huang, Z. Ramanis, and D.J. Luck. Suppressor mutations in *Chlamydomonas* reveal a regulatory mechanism for flagellar function. *Cell*, 28(1):115–24, 1982.
43. C.J. Brokaw and D.J. Luck. Bending patterns of *Chlamydomonas* flagella: III. A radial spoke head deficient mutant and a central pair deficient mutant. *Cell Motil*, 5(3):195–208, 1985.
44. C.K. Omoto et al. Ability of paralyzed flagella mutants of *Chlamydomonas* to move. *Cell Motil Cytoskeleton*, 33(2):88–94, 1996.
45. E. Frey, C.J. Brokaw, and C.K. Omoto. Reactivation at low ATP distinguishes among classes of paralyzed flagella mutants. *Cell Motil Cytoskeleton*, 38(1):91–9, 1997.
46. T. Yagi and R. Kamiya. Vigorous beating of *Chlamydomonas* axonemes lacking central pair/radial spoke structures in the presence of salts and organic compounds. *Cell Motil Cytoskel*, 46(3):190–9, 2000.
47. A. Fleury and M. Laurent. Coverpage. *Science*, 266(5191):1619, Dec 9 1994.

48. H. Machemer and J.W. Deitmar. From structure to behavior: Stylonychia as a model system for cellular physiology. In John O. Corliss and David J. Patterson, editors, *Progress in Protistology*. Biopress, Bristol, 1986.
49. S.L. Tamm and G.a. Horridge. Relation between orientation of central fibrils and direction of beat in cilia of Opalina. *Proc Roy Soc Lond B Bio*, 175(1040):219–&, 1970.
50. G.J. Pazour and G.B. Witman. The vertebrate primary cilium is a sensory organelle. *Curr Opin Cell Biol*, 15(1):105–10, 2003.
51. S. Nonaka et al. Erratum: Randomization of left-right asymmetry due to loss of nodal cilia generating leftward flow of extraembryonic fluid in mice lacking KIF3B motor protein. *Cell*, 99(1):116, 1999.
52. D.L. Odor and R.J. Blandau. Observations on the solitary cilium of rabbit oviductal epithelium - its motility and ultrastructure. *Am J Anat*, 174(4):437–53, 1985.
53. J.H. Cartwright, O. Piro, and I. Tuval. Fluid-dynamical basis of the embryonic development of left-right asymmetry in vertebrates. *Proc Natl Acad Sci U S A*, 101(19):7234–9, 2004.
54. S. Nonaka et al. De novo formation of left-right asymmetry by posterior tilt of nodal cilia. *PLoS Biology*, 3(8), 2005.
55. S. Nonaka et al. Determination of left-right patterning of the mouse embryo by artificial nodal flow. *Nature*, 418(6893):96, 2002.
56. A.G. Kramer-Zucker et al. Cilia-driven fluid flow in the zebrafish pronephros, brain and Kupffer’s vesicle is required for normal organogenesis. *Development*, 132(8):1907–21, 2005.
57. I. Ibanez-Tallon, N. Heintz, and H. Omran. To beat or not to beat: Roles of cilia in development and disease. *Hum Mol Genet*, 12(90001):27R–35, 2003.
58. M.E.J. Holwill and J.L. Mcgregor. Control of flagellar wave movement in Crithidia-oncopelti. *Nature*, 255(5504):157–8, 1975.
59. P. Sugrue et al. Flagellar wave reversal in the kinetoplastid flagellate Crithidia oncopelti. *Biol Cell*, 63(2):127–31, 1988.
60. C.J. Brokaw. Calcium-induced asymmetrical beating of triton-demembranated sea urchin sperm flagella. *J Cell Biol*, 82(2):401–11, 1979.
61. J.S. Hyams and G.G. Borisy. Isolated flagellar apparatus of Chlamydomonas: Characterization of forward swimming and alteration of waveform and reversal of motion by calcium ions in vitro. *J Cell Sci*, 33:235–53, 1978.
62. C.D. Wood et al. Real-time analysis of the role of Ca(2+) in flagellar movement and motility in single sea urchin sperm. *J Cell Biol*, 169(5):725–31, 2005.
63. K. Wakabayashi, T. Yagi, and R. Kamiya. Ca2+-dependent waveform conversion in the flagellar axoneme of Chlamydomonas mutants lacking the central-pair/radial spoke system. *Cell Motil Cytoskeleton*, 38(1):22–8, 1997.

64. C.K. Omoto et al. Rotation of the central pair microtubules in eukaryotic flagella. *Mol Biol Cell*, 10(1):1–4, 1999.
65. E.F. Smith. Regulation of flagellar dynein by the axonemal central apparatus. *Cell Motil Cytoskel*, 52(1):33–42, 2002.
66. I. Nakano et al. Central-pair-linked regulation of microtubule sliding by calcium in flagellar axonemes. *J Cell Sci*, 116(8):1627–36, 2003.
67. D.R. Mitchell and M. Nakatsugawa. Bend propagation drives central pair rotation in *Chlamydomonas reinhardtii* flagella. *J Cell Biol*, 166(5):709–15, 2004.
68. M.J. Wargo, M.A. McPeck, and E.F. Smith. Analysis of microtubule sliding patterns in *Chlamydomonas* flagellar axonemes reveals dynein activity on specific doublet microtubules. *J Cell Sci*, 117(Pt 12):2533–44, 2004.
69. B. Afzelius. Electron microscopy of the sperm tail - results obtained with a new fixative. *J Biophys Biochem Cy*, 5(2):269–&, 1959.
70. I.R. Gibbons. Relationship between fine structure and direction of beat in gill cilia of a lamellibranch mollusc. *J Biophys Biochem Cy*, 11(1):179–&, 1961.
71. H. Bannai et al. Calcium regulation of microtubule sliding in reactivated sea urchin sperm flagella. *J Cell Sci*, 113(5):831–9, 2000.
72. E.F. Smith. Regulation of flagellar dynein by calcium and a role for an axonemal calmodulin and calmodulin-dependent kinase. *Molecular Biol Cell*, 13(9):3303–13, 2002.
73. Y. Hosokawa and T. Miki-Noumura. Bending motion of *Chlamydomonas* axonemes after extrusion of central-pair microtubules. *J Cell Biol*, 105(3):1297–301, 1987.
74. C.J. Brokaw and R. Kamiya. Bending patterns of *Chlamydomonas* flagella: IV. Mutants with defects in inner and outer dynein arms indicate differences in dynein arm function. *Cell Motil Cytoskeleton*, 8(1):68–75, 1987.
75. I. Minoura and R. Kamiya. Strikingly different propulsive forces generated by different dynein-deficient mutants in viscous media. *Cell Motil Cytoskeleton*, 31(2):130–9, 1995.
76. E. Kurimoto and R. Kamiya. Microtubule sliding in flagellar axonemes of *Chlamydomonas* mutants missing inner- or outer-arm dynein: Velocity measurements on new types of mutants by an improved method. *Cell Motil Cytoskeleton*, 19(4):275–81, 1991.
77. R. Kamiya. Exploring the function of inner and outer dynein arms with *Chlamydomonas* mutants. *Cell Motil Cytoskeleton*, 32(2):98–102, 1995.
78. C. Shingyoji et al. Dynein arms are oscillating force generators. *Nature*, 393(6686):711, 1998.
79. R. Kamiya. Functional diversity of axonemal dyneins as studied in *Chlamydomonas* mutants. *Int Rev Cytol*, 219:115–55, 2002.

90 Bibliography

80. C. Shingyoji et al. Effect of beat frequency on the velocity of microtubule sliding in reactivated sea urchin sperm flagella under imposed head vibration. *J Exp Biol*, 198(Pt 3):645–53, 1995.
81. I.R. Gibbons et al. Spontaneous recovery after experimental manipulation of the plane of beat in sperm flagella. *Nature*, 325(6102):351–2, 1987.
82. C. Shingyoji et al. Rotating the plane of imposed vibration can rotate the plane of flagellar beating in sea-urchin sperm without twisting the axoneme. *J Cell Sci*, 98 (Pt 2):175–81, 1991.
83. K. Takahashi et al. Polarity in spontaneous unwinding after prior rotation of the flagellar beat plane in sea-urchin spermatozoa. *J Cell Sci*, 98 (Pt 2):183–9, 1991.
84. G. Taylor. Analysis of the swimming of microscopic organisms. *Proc Roy Soc Lond A Mat*, 209(1099):447–61, 1951.
85. E.M. Purcell. Life at low Reynolds-number. *Am J Phys*, 45(1):3–11, 1977.
86. K.E. Machin. Wave propagation along flagella. *J Exp Biol*, 35(4):796–806, 1958.
87. P. Satir. Studies on cilia: Ii. examination of the distal region of the ciliary shaft and the role of the filaments in motility. *J Cell Biol*, 26(3):805–34, 1965.
88. K.E. Summers and I.R. Gibbons. Adenosine triphosphate-induced sliding of tubules in trypsin-treated flagella of sea-urchin sperm. *Proc Natl Acad Sci U S A*, 68(12):3092–&, 1971.
89. R.H. Dillon and L.J. Fauci. An integrative model of internal axoneme mechanics and external fluid dynamics in ciliary beating. *J Theor Biol*, 207(3):415–30, 2000.
90. V.V. Eliseev, I.V. Ogneva, and V.O. Samoilov. Mathematical modeling of the movement of cilia in olfactory cells. *Biofizika*, 48(5):884–90, 2003.
91. C.J. Brokaw. Computer simulation of flagellar movement: IX. Oscillation and symmetry breaking in a model for short flagella and nodal cilia. *Cell Motil Cytoskeleton*, 60(1):35–47, 2005.
92. C.B. Lindemann. A geometric clutch hypothesis to explain oscillations of the axoneme of cilia and flagella. *J Theor Biol*, 168(2):175–89, 1994.
93. C.B. Lindemann. A model of flagellar and ciliary functioning which uses the forces transverse to the axoneme as the regulator of dynein activation. *Cell Motil Cytoskel*, 29(2):141–54, 1994.
94. C.J. Brokaw and D.R. Rintala. Computer simulation of flagellar movement. III. models incorporating cross-bridge kinetics. *J Mechanochem Cell Motil*, 3(2):77–86, 1975.
95. C.J. Brokaw. Computer-simulation of flagellar movement:VI. Simple curvature-controlled models are incompletely specified. *Biophys J*, 48(4):633–42, 1985.

96. C.J. Brokaw. Computer simulation of flagellar movement: VII. Conventional but functionally different cross-bridge models for inner and outer arm dyneins can explain the effects of outer arm dynein removal. *Cell Motil Cytoskel*, 42(2):134–48, 1999.
97. C.J. Brokaw. Simulating the effects of fluid viscosity on the behaviour of sperm flagella. *Math Method Appl Sci*, 24(17-18):1351–65, 2001.
98. C.J. Brokaw. Computer simulation of flagellar movement: VIII. Coordination of dynein by local curvature control can generate helical bending waves. *Cell Motil Cytoskel*, 53(2):103–24, 2002.
99. C.B. Lindemann. Geometric clutch model version 3: The role of the inner and outer arm dyneins in the ciliary beat. *Cell Motil Cytoskel*, 52(4):242–54, 2002.
100. C.B. Lindemann. Testing the geometric clutch hypothesis. *Biol Cell*, 96(9):681–90, 2004.
101. F. Jülicher and J. Prost. Spontaneous oscillations of collective molecular motors. *Phys Rev Lett*, 78(23):4510–3, 1997.
102. K. Yasuda, Y. Shindo, and S. Ishiwata. Synchronous behavior of spontaneous oscillations of sarcomeres in skeletal myofibrils under isotonic conditions. *Biophys J*, 70(4):1823–9, 1996.
103. H. Fujita and S. Ishiwata. Spontaneous oscillatory contraction without regulatory proteins in actin filament-reconstituted fibers. *Biophys J*, 75(3):1439–45, 1998.
104. C.J. Brokaw. Molecular mechanism for oscillation in flagella and muscle. *Proc Natl Acad Sci U S A*, 72(8):3102–6, 1975.
105. S. Camalet, F. Jülicher, and J. Prost. Self-organized beating and swimming of internally driven filaments. *Phys Rev Lett*, 82(7):1590–3, 1999.
106. S. Camalet and F. Jülicher. Generic aspects of axonemal beating. *New Journal of Physics*, 2:1–23, 2000.
107. R.E. Goldstein, T.R. Powers, and C.H. Wiggins. Viscous nonlinear dynamics of twist and writhe. *Phys Rev Lett*, 80(23):5232–5, 1998.
108. C.W. Wolgemuth, R.E. Goldstein, and T.R. Powers. Dynamic supercoiling bifurcations of growing elastic filaments. *Physica D*, 190(3-4):266–89, 2004.
109. S. Camalet. *Oscillations Critiques De Systèmes Biologiques*. PhD thesis, Université Paris 6, 2001.
110. F. Jülicher, A. Ajdari, and J. Prost. Modeling molecular motors. *Rev Mod Phys*, 69(4):1269–81, 1997.
111. F. Jülicher and J. Prost. Molecular motors: From individual to collective behavior. *Prog Theor Phys Supp*, (130):9–16, 1998.
112. A.J. Hunt, F. Gittes, and J. Howard. The force exerted by a single kinesin molecule against a viscous load. *Biophys J*, 67(2):766–81, 1994.

92 Bibliography

113. K. Svoboda and S.M. Block. Force and velocity measured for single kinesin molecules. *Cell*, 77(5):773–84, 1994.
114. E. Meyhofer and J. Howard. The force generated by a single kinesin molecule against an elastic load. *Proc Natl Acad Sci U S A*, 92(2):574–8, 1995.
115. S.M. Block et al. Probing the kinesin reaction cycle with a 2D optical force clamp. *Proc Natl Acad Sci U S A*, 100(5):2351–6, 2003.
116. D. Riveline et al. Acting on actin: The electric motility assay. *Eur Biophys J Biophys*, 27(4):403–8, 1998.
117. F. Jülicher. Mechanical oscillations at the cellular scale. *Cr Acad Sci IV-Phys*, 2(6):849–60, 2001.
118. K. Kruse and F. Jülicher. Oscillations in cell biology. *Curr Opin Cell Biol*, 17(1):20–6, 2005.
119. P. Martin, A.D. Mehta, and A.J. Hudspeth. Negative hair-bundle stiffness betrays a mechanism for mechanical amplification by the hair cell. *Proc Natl Acad Sci U S A*, 97(22):12026–31, 2000.
120. P. Martin and A.J. Hudspeth. Compressive nonlinearity in the hair bundle’s active response to mechanical stimulation. *Proc Natl Acad Sci U S A*, 98(25):14386–91, 2001.
121. B. Nadrowski, P. Martin, and F. Jülicher. Active hair-bundle motility harnesses noise to operate near an optimum of mechanosensitivity. *Proc Natl Acad Sci U S A*, 101(33):12195–200, 2004.
122. S.W. Grill, K. Kruse, and F. Jülicher. Theory of mitotic spindle oscillations. *Phys Rev Lett*, 94(10), 2005.
123. S.W. Grill et al. Mitotic spindle oscillations. *Biophys J*, 88(1):539A–A, 2005.
124. D. Adams. *The Hitchhiker’s Guide to the Galaxy*. Ballantine Books, New York, NY, 2005.
125. D.E. Mulready and R. Rikmenspoel. Time course of the motion of bull sperm flagella. *Cell Motil Cytoskel*, 4(5):387–401, 1984.
126. S.A. Baba and Y. Mogami. An approach to digital image-analysis of bending shapes of eukaryotic flagella and cilia. *Cell Motil Cytoskel*, 5(6):475–89, 1985.
127. D.N. Johnston, N.R. Silvester, and M.E.J. Holwill. Analysis of the shape and propagation of waves on the flagellum of *Crithidia oncopelti*. *J Exp Biol*, 80(JUN):299–&, 1979.
128. M.C. Holley. Adaptation of a ciliary basal apparatus to cell shape changes in a contractile epithelium. *Tissue Cell*, 17(3):321–34, 1985.
129. B.N. Gomperts, X. Gong-Cooper, and B.P. Hackett. Foxj1 regulates basal body anchoring to the cytoskeleton of ciliated pulmonary epithelial cells. *J Cell Sci*, 117(Pt 8):1329–37, 2004.

130. C.D. Silflow et al. The Vfl1 protein in *Chlamydomonas* localizes in a rotationally asymmetric pattern at the distal ends of the basal bodies. *J Cell Biol*, 153(1):63–74, 2001.
131. M.E. Porter and W.S. Sale. The 9 + 2 axoneme anchors multiple inner arm dyneins and a network of kinases and phosphatases that control motility. *J Cell Biol*, 151(5):37F–42, 2000.
132. Y. Okada et al. Abnormal nodal flow precedes situs inversus in *iv* and *inv* mice. *Mol Cell*, 4(4):459–68, 1999.
133. M. Brueckner. Cilia propel the embryo in the right direction. *Am J Med Genet*, 101(4):339–44, 2001.
134. J. McGrath and M. Brueckner. Cilia are at the heart of vertebrate left-right asymmetry. *Curr Opin Genet Dev*, 13(4):385–92, 2003.
135. W.B. Wood. The left-right polarity puzzle: Determining embryonic handedness. *PLoS Biol*, 3(8):e292, 2005.
136. E. Boisvieux-Ulrich and D. Sandoz. Determination of ciliary polarity precedes differentiation in the epithelial cells of quail oviduct. *Biol Cell*, 72(1-2):3–14, 1991.
137. R. Goldstein. Private communication.

